Affordable Soft and Semi-rigid Robot Designs

Case Studies via Compliance Tuning and Mechanism Design

by

Dongting Li

A Dissertation Presented in Partial Fulfillment
of the Requirements for the Degree
Doctor of Philosophy

Approved March 2023 by the
Graduate Supervisory Committee:

Daniel M. Aukes, Chair
Thomas G. Sugar
Wenlong Zhang

ARIZONA STATE UNIVERSITY

August 2023

ABSTRACT

Robotic technology can be broadly categorized into two main approaches based on the compliance of the robot's materials and structure: hard and soft. Hard, traditional robots, with mechanisms to transmit forces, provide high degrees of freedom (DoFs) and precise manipulation, making them commonly used in industry and academic research. The field of soft robotics, on the other hand, is a new trend from the past three decades of robotics that uses soft materials such as silicone or textiles as the body or material base instead of the rigid bodies used in traditional robots.

Soft robots are typically pre-programmed with specific geometries, and perform well at tasks such as human-robot interaction, locomotion in complex environments, and adaptive reconfiguration to the environment, which reduces the cost of future programming and control. However, full soft robotic systems are often less mobile due to their actuation − pneumatics, high-voltage electricity or magnetics − even if the robot itself is at a millimeter or centimeter scale. Rigid or hard robots, on the other hand, can often carry the weight of their own power, but with a higher burden of cost for control and sensing. A middle ground is thus sought, to combine soft robotics technologies with rigid robots, by implementing mechanism design principles with soft robots to embed functionalities or utilize soft robots as the actuator on a rigid robotic system towards an affordable robotic system design.

This dissertation showcases five examples of this design principle with two main research branches: locomotion and wearable robotics. In the first research case, an example of how a miniature swimming robot can navigate through a granular environment using compliant plates is presented, compared to other robots that change their shape or use high DoF mechanisms. In the second pipeline, mechanism design is implemented using soft robotics concepts in a wearable robot. An origami-inspired, soft "exo-shell", that can change its stiffness on demand, is introduced. As a follow-up

to this wearable origami-inspired robot, a geometry-based, "near" self-locking modular brake is then presented. Finally, upon combining the origami-inspired wearable robot and brake design, a concept of a modular wearable robot is showcased for the purpose of answering a series of biomechanics questions.

To my parents.

ACKNOWLEDGMENTS

My foremost appreciation belongs to my Ph.D. advisor, Dr. Daniel Aukes. Five years ago, as I began my journey as a Ph.D. student, it was Dr. Aukes who introduced me to the enthralling world of research and exploration. Without him, I wouldn't have progressed as far as I have (though I am aware there's still a long road ahead). I vividly recall the early days of our weekly meetings at IDEAlab. When presenting, Dan once advised me, "Imagine they do not know that at all". This sentiment resonated with me deeply, leading me to pin it as a reminder atop my Google Keep notes.

As I delved deeper into my research on granular robots, I began to realize the extent of my professor's brilliance. His mind was a fountain of ideas and inspiration. I found myself often overwhelmed, questioning how I might evolve into a successful Ph.D., researcher, and educator like him.

In all honesty, there were times when my advisor's intellect surpassed my comprehension, especially concerning complex subjects such as kinematics, dynamics, and mechanisms. I remember the prolonged period of despair when my progress slowed, and failures seemed frequent. Yet, Dr. Aukes was always patient, encouraging me to move at my own pace. I grappled with balancing my research and personal life during these challenging times. But under my advisor's guidance, patience, and tolerance, I persevered. Interestingly, the region we inhabit is called "Phoenix", symbolizing rebirth from one's own ashes—a metaphor that resonates with my personal journey through this Ph.D.

Dan taught me a valuable lesson: no one can make decisions for me, and I'm free to choose my own path. Yet, without his guidance, getting through the many challenges I faced would have been extremely difficult. All of Dr. Aukes's teaching, mentorship, and guidance have been instrumental in helping me navigate through

the complex world of academia. His wisdom didn't just show me the way but also gave me the strength to keep going, even when faced with significant obstacles and doubts. I want to thank him once more for his unconditional patience, guidance, and for sharing his knowledge on design, paper writing, and research. Dan, I hope I have made you proud.

I extend heartfelt gratitude to my committee members, Dr. Thomas Sugar and Dr. Wenlong Zhang, who served not just as lecturers, but also as collaborators and advisors. Collaborating with them on a project spanning three years has left me with delightful memories. Their encouragement and recognition have been potent motivators throughout my journey. The knowledge they imparted during classes, meetings, and paper writing sessions remains an invaluable asset that will continue to guide my future research endeavors.

Additionally, I would like to express my appreciation to all my collaborators and co-authors for their contributions and insights that significantly enhanced our collective work. My gratitude also extends to all the past and current members of the IDEAlab and RISE Lab. Joining the lab as a mid-generation member provided me a unique perspective and the opportunity to learn from a diverse group of researchers. The chance to work alongside, learn from, and contribute to this talented group of individuals has truly been a privilege. The experiences I've gained and the relationships I've fostered will continue to shape my academic journey in the years to come. I am sincerely grateful to have had the opportunity to know and work with you all.

Beyond the confines of the lab and course works, I owe a considerable debt of gratitude to my friends, Y.W., Y.K., Y.Z., and Y.Z. (It only dawned on me as I penned this acknowledgement that all your names intriguingly commence with a "Y"). The magnitude of your unwavering support and the richness of the companionship you offered throughout this journey is inexpressible. To Dr. W., I extend my heartfelt

thanks for aiding me in navigating and acclimating to an unfamiliar environment. Your perennial support and words of encouragement have been a pillar of strength for me. Y.K., as you steadily tread your path towards earning the Dr. title, I eagerly look forward to welcoming you to the other side!

To Drs. Z. and Z., I recall fondly the countless happy hours, exhilarating game nights, and memorable moments shared with L.X.Z. and C. Z. Our long-anticipated but belated road trip, marked by a melancholic rainy drive back, echoes in my mind as a sweet reminder of the joyful times we missed together. A special mention is deserved by L.X.Z. Our relationship is adorned by a myriad of special connections, and I cherish the hope that my presence will remain etched in your "growing but vanishing" memory until we meet again.

Finally, I want to express my deepest gratitude to my parents for their unwavering support and generosity during this challenging period. Their unconditional love, support, and encouragement served as the ultimate source of strength propelling me forward. Thank you for always standing by me and instilling in me the resilience and determination that were pivotal to my journey. I love you.

The sketches included in this work have been created using the Adobe Illustrator plug-in LaTeX2AI, which can be found at `https://github.com/isteinbrecher/latex2ai`. I appreciate the effort of the author in developing this beneficial plugin.

TABLE OF CONTENTS

CHAPTER Page

CHAPTER Page

CHAPTER Page

LIST OF TABLES

LIST OF FIGURES

Figure Page

Chapter 1

INTRODUCTION

1.1 The Philosophical Question

It was 2010. When I was a teenager, one day, I watched a TV show. I remember they were talking about a scientist who obtained his Ph.D. degree in 1950. The host asked:

> *Why is it a Doctor of Philosophy? Obviously, he is a physicist.'*
>
> *That is because in ancient Greece, all sciences were considered as philosophy.'*

Probably from then on, I wished I could become a Ph.D. who could answer scientific questions from a philosophical perspective, although I did not know it's really common for physics student to be awarded a Ph.D. After thirteen years, I realized that this dream was far more ambitious than I initially thought. First of all, I became an engineering student instead of a scientist. Even so, I still found it difficult to give a clear answer of engineering philosophy problems, but the fortunate thing is that I believe I can discuss this open question and provide some of my insights into it. Here, I would like to pose my philosophical question:

Is the human hand a soft or rigid robot?

Indeed, one could answer the question by stating that the human hand is a "bio-robot" to avoid this yes-or-no question. This question is worth contemplating because the skin and muscles on the outside are grown with soft tissues, at the same time, the

bones can be considered as rigid components. The tendons attached to the bones are part of cable-driven systems actuated by the muscles in the forearm. If we consider the muscles as actuators, they should be categorized as soft actuators from a robotics perspective.

One could oversimplify the human hand as a rigid structure actuated by soft actuators with compliant materials coating the exterior. Depending on the task, the hand exhibits different characteristics and can switch from rigid to soft or somewhere in between. This is arguably the most appropriate characterization I can offer at this juncture.

Evolution, over the course of millions of decades, has selected this particular construction for the human hand, which is often the product of a minimal cost objective. This bio-inspiration presents us with valuable insights into combining two categories of robots to design an affordable, low-cost robotic system. To offer more insight into soft and rigid robotics, I would like to begin with a brief discussion on those two major categories of robots.

1.2 Affordable Robot Design via Combing Soft and Hard Robotics

My research focuses on the intersection of soft and rigid robotics, utilizing an affordable approach to address real-world problems such as locomotion and wearable robot applications to make soft robots accessible, low-cost, and yet efficient.

Affordability should not be limited to financial cost, but should also encompass actuation, control, computation, and response speed. Over the past thirty years, the field of soft robotics has evolved from simple inflated multi-chamber tube actuator [103, 45] to an expansive family that includes grippers, locomotors, and actuators. Some common features in soft robots are: 1) made of soft materials, 2) actuated by pneumatic, hydraulic, dielectric elastomer actuators (DEA), shape memory alloy

(SMA), magnetic fields, and other unconventional power sources, 3) highly deformable and adaptable, making them safer for interacting with their environments.

Unlike traditional rigid robots powered by motors, gears, and belts, soft robots face certain limitations in response speed, actuation, and recovery due to their material properties and sources of actuation. Additionally, the overall mobility and affordability can be impacted by the size and weight of air compressors or high-voltage generators commonly associated with soft robotics research.

Soft robots also excel at performing tasks that are challenging for rigid robots, particularly those involving significant uncertainty, for example, grasping or complex terrain locomotion. The price, as mentioned, is that soft robots are less efficient, compared to rigid robots.

In many soft robotics systems, especially those using pneumatics, high-voltage electricity or magnetic fields, the robot or its end-effector may be small even when its support systems, or those parts related to sensing and power delivery – power sources, control units, tubing, wiring – tend to be large and heavy, making soft robots less feasible in mobile scenarios.

On the other hand, while rigid robots appear bulky, they are stronger and stiffer, which makes them able to carry the weight of their support systems. Most rigid robots are powered by motors and use more conventional power sources for actuation, and despite their size, capable of complex motion and high precision [117]. These relations are illustrated in Fig. 1.1; can we combine these two kinds of robots towards a more affordable and efficient robot?

To leverage the advantages of both types of robots, I focus on natural combinations of soft and rigid components into a system to make it more efficient and affordable. Depending on the proportion and primary component of the two robot types, in my doctoral studies, I primarily use two methods to combine soft and rigid robots.

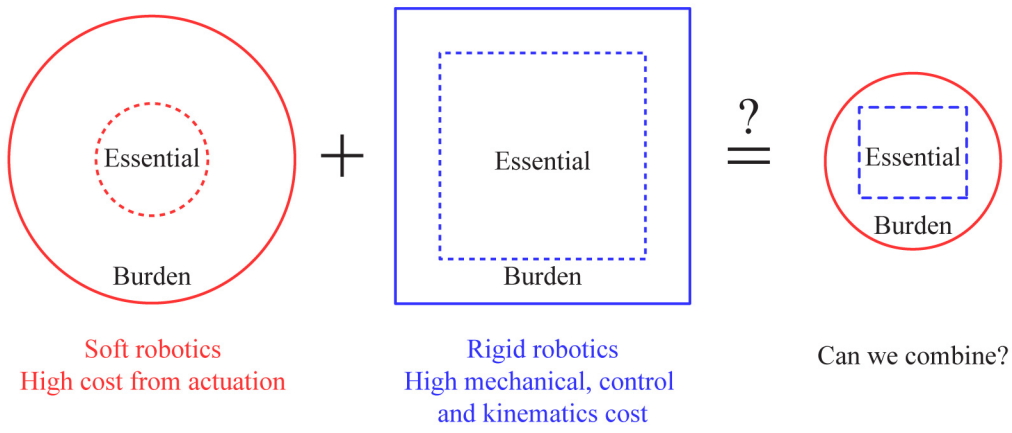

Figure 1.1. Combine soft and rigid robots

1.3 Method I: Use Soft Robots as the End-effector in a Rigid Robot System

Method I is to use soft robots as a flexible or compliant actuator or end-effector in a rigid robot system; this method is exemplified in this thesis for a granular-related application. This can be helpful in granular applications, as soft materials adapt better to the surrounding environment, which can leverage the performance of the traditional rigid robot it is attached to, such as the base robot for granular terrain exploration.

To be more specific, the general approach begins with identifying the functionality necessary for the soft actuator to have in order to interact with the environment, as well as the existing hard or rigid robot system it will be attaching to, in order to leverage such adaptability. To reduce cost, it follows that the minimal mechanism or geometry suitable for this specific task should then be selected. With these design principles and initial design in hand, one can start evaluating the performance of potential designs by modeling both the end-effector and the environment, and optimizing performance using a combination of experimental approaches and optimization methods. Finally, a system-level evaluation of the new robot should be carried out

to examine the design goals. This approach is exemplified in the following research case.

1.3.1 Case 1 – Compliant Fins for Locomotion in Granular Media

This research case was funded by the NSF Signals in the Soils (SitS) program and is presented in Chapter 3. To apply the general design principle with granular swimming robot scenarios, I aim to answer the question: "How to design a minimal robot for complex environments such as granular media using soft robotics techniques?" In this chapter, I showcase the design, manufacturing and modeling of an origami-inspired compliant plate for a miniature granular swimming robot based on a rigid flapping wing robot. The detailed approaches using method I are as follows: 1) Identify the major features of this environment and find the approximate model to describe it, 2) Based upon this model, then find the minimal mechanism to achieve a desired functionality within the environment, 3) With a preliminary prototype or design in mind, combine modeling, optimization and experimental validation to ensure the minimal robot and, 4) Perform system level swimming experiments and compare with the design goal.

I have also showed an example of building an experimental setup to obtain granular parameters in order to validate the effectiveness of the design. Finally, using the knowledge I have obtained, I performed an design optimization to select an optimal configuration of the robot using swimming efficiency as the objective.

1.4 Method II: Implement Mechanism Design to Soft Robot

Method II involves implementing mechanical design principles in larger soft robotic systems. In my dissertation, this approach is generally suitable for wearable robots, due to the inherent safety of soft materials.

Based on the specific robotic task, one first identifies the system-level requirement, such as range of motion, external force feedback or stiffness, and then select the appropriate soft structural elements. Then, using foundational principles of soft structures, the performance of these compliant robots can be greatly enhanced by incorporating elements of mechanism design. With mechanism design or structural geometry embedded inside the soft robot, complex structural elements that maintain the desired functionality can be then created. This technique allows us to combine soft and rigid components effectively, creating low-profile yet high-performance systems. To illustrate, we use this design principle to real world problem for wearable robots in the following two case studies.

1.4.1 Case 2 – Origami-inspired Wearable Robot for Trunk Support

Starting from Chapter 4, I illustrate how one can implement mechanism design in a larger soft robotic system to create embodied functionality. This and the following cases are all funded by the Kaiteki Project, titled "A Wearable Hybrid Robotic Suit for Self-Actualization and Well-Being". As the first case in this series, I designed a lightweight robot that can be worn on the human back as a robotic spine to provide on-demand external stiffness while remaining soft, lightweight and low resistance when unlocked during human walking. The scenario studied by collaborators for this system design was obstacle avoidance in elderly walking.

Using the general methodology of implementing mechanism design within soft robots, I selected a laminate-based, origami-inspired manufacturing method to construct a serially-connected, multi-segment robot made from lightweight yet strong structural elements. To create embedded switchable stiffness, I selected a *global* stiffening strategy to lock all segments simultaneously, providing the robot with on-demand rigidity. This is done by attaching attaching belts to each element then

locking all belts at once, using an mechanical brake to stiffen the system. I then introduced the components and design methodologies for this robot and use a "mix-and-match" approach to fit the user. Since both rotational and translational elements are implemented in this robot, I derived two basic kinematic models using a custom Python dynamics library called Pynamics. I then introduced a system-level workflow to identify the weakest joint and confirm the design requirements for the brake element. Finally, I presented the experimental setup, method, and protocol for validating the kinematic model, and then performed a system-level test to evaluate the stiffness and response speed of the robot.

1.4.2 Case 3 – Modular Lockable Module for Wearable Robot

While the *global* locking strategy in Case 2 offers a straightforward solution for stiffening the device, it also increases the *system*-level complexity, making it less convenient to tailor to different users and expand its number of use cases. Additionally, the force provided by the global brake is insufficient for human-level forces. Therefore, the objective of Chapter 5 is to explore the design of a rapidly-customizable wearable robot with high-force locking strategies integrated into each structural element.

To satisfy the fast-customization requirement, I propose a modular design principle for the locking module. This approach involves using generalized connectors at the top and bottom of the locking module, allowing for serial connections. I then commence an investigation into the locking strategies for each element with the goal of achieving fast response times, high resistive torque, compactness, low weight, and low power consumption.

However, upon investigation and literature review of locking devices in robotics, I find that none of the existing solutions meet my requirements. Taking inspiration from self-locking mechanisms, I introduce novel locking strategies that incorporate a series

of mechanical designs and modifications. More specifically, I illustrate the design inspiration behind the locking device in a single brake and the customization made to improve its performance. I then explain the mechanism design and integration of the single brake into the lockable module, along with other design considerations including sets of pulleys, belt routing systems, and linear tensioners.

With the single lockable module presented, I subsequently introduce the experimental setup and method for evaluating force/torque, feasibility, and response speed. This series of evaluations answers the question of how to design an efficient locking system. In conjunction with the modular design concepts, I equip the lockable module with modular connectors as well as wearing interfaces that can be adapted to fit the user. With these mechanism-designed structural elements, I then construct the final soft wearable robot systems and demonstrate its ability to control the external stiffness provided on demand.

1.5 Summary of Methodology

I summarize each case study by its methodology, manufacturing method, modeling and analytical approach, and experimental approach in Table. 1.1. Following these two general methodologies, I use the design tool and skill sets selectively to solve a particular robotics problem. These design methodologies can still be applied to general robotics research to solve various problems. For example, one can design a compliant gripper that attaches to a rigid robot arm or soft landing/perching mechanism for a quad copter drone using method I. On the other hand, embedded mechanisms can be used alongside or within soft silicone-based robots or other pneumatic based robots to leverage their performance.

Method/ Scenario	**Case study**	**Design/ Manufacturing**	**Modeling/ Analysis**	**Experiments**
Method 1 Granular	Compliant fins for locomotion	3D print Origami-inspired	Dynamics RFT	Granular Experiments Python
Method 2 Wearable	Origami-inspired wearable robot	Origami-inspired	Kinematics	Tensile testing Kinematics validation Speed response Stiffness measurement
	Modular Lockable module	Mechanism design	Cam-profile	Tensile testing Speed response

Table 1.1: **Case Study Summary**

1.5.1 The Blurring Boundary and the Mysterious Cut-off Point

Over several decades of development, a wide array of "soft robots" have emerged that vary in the overall ratio of soft material components to the whole body and utilize soft robotics technologies as critical components for certain robotic tasks. While this dissertation will not definitively demarcate the exact boundary between soft and rigid robots in a manner that may satisfy all, it presents my robots and some of their components within the spectrum shown in Fig. 1.2. This spectrum considers multiple variables such as the ratio of soft components to all components and the location of compliance, whether it is at the material, mechanism, or system level.

Compliant fins, indicated by (a), are comprised mostly of soft components and exhibit compliance at the mechanism level, as the fin assembly operates as the soft actuator of the rigid robot shown at (b). I categorize (a) as a soft robot actuator. Similarly, I position the single origami-inspired wearable element at (c), where compliance exists between the mechanism and material level. For the origami-inspired wearable robot, the soft materials primarily consist of the living hinge of the origami element and the transmission belt. However, the robot body is analyzed using rigid body dynamics, shifting its position to the left half-plane around (d). As for the

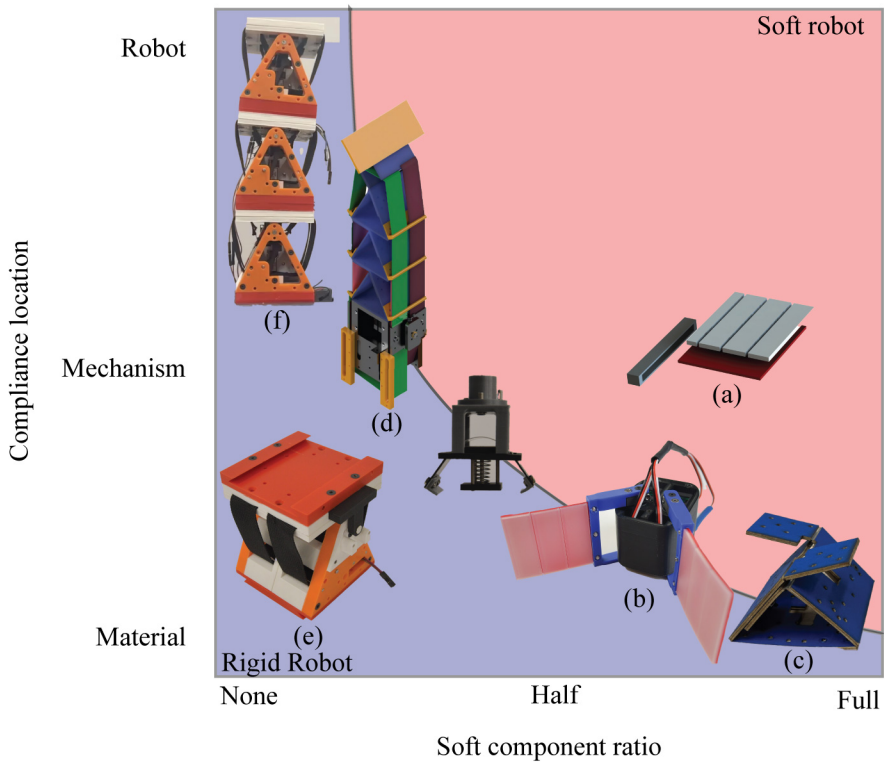

Figure 1.2. Position of my robots according to their soft ratio and compliance location

modular lockable module, I place it in the middle left at (e) as its flexible material level is low and it can be considered a locking robot itself, even without the final wearable robot, which is positioned right above the module in (f). As indicated by the color, where pink stands for soft robots and blue represents rigid robots, many of my robots are situated on the boundary between these two kinds, as many robots presented combine these two techniques. While other researchers might define the boundary between soft and rigid at a different level, I illustrate my boundary using a solid line and many of my robots lie on the boundary between soft and rigid robots.

1.5.2 Definitions in This Dissertation

To better clarify the concept in this dissertation, I provide a local statement of definition of the common terms found in soft robotics research; these definitions will

be used throughout this dissertation.

- **Soft:** The term "soft" is the most broadly defined term in this dissertation. It can refer to a low rigidity in the material, embody flexibility in the mechanism, or exhibit compliance at the system level. I believe it's the most inclusive term that can be used across different dimensions, including material, mechanism, and system level.

- **Flexible:** "Flexible" often refers to two main attributes: 1) its own material proprieties permit deformation upon encountering external loads, for example, flexible materials or beams or 2) it possess adaptability for future adjustment, such as in flexible manufacturing. In this thesis, I mainly use "flexible" to refer to flexible materials.

- **Compliant:** "Compliant" means that the object or mechanism can adapt its geometry or form to conform to an external shape or to accommodate an external force. This property is often exploited at the mechanism level to provide adaptability and versatility in interaction with the environment, differing slightly from the term "soft". For instance, compared to a soft actuator, a compliant actuator might exhibit softness only in some portions of its entire body while still having rigid components inside, whereas soft actuators usually denote a larger ratio of compliance. In this dissertation, "compliant" is typically used to refer to a mechanism or mechanical part that exhibits material softness, e.g. compliant fin.

- **Rigid/Hard** "Rigid" or "hard" typically signifies that the object or material exhibits high resistance to changes in shape and deformation under applied forces. It usually implies low compliance, high stiffness, and a high degree of

resistance to bending or folding. In this thesis, these two terms mean that it doesn't have features described by the previous three definitions, e.g. rigid base, hard material and rigid arm.

1.6 Contribution

As suggested by the title of the dissertation, "Affordable Soft and Semi-rigid Robot Designs – Case Studies via Compliance Tuning and Mechanism Design" this dissertation reports a series of *case studies* for the investigation of *soft and semi-rigid robotics* using *experimental methods*, including compliance tuning and mechanism design. The significant contributions of this dissertation include:

- Providing foundational research examples to guide newcomers in soft robotics. Through the general methodologies of combining soft and rigid robotics and the exemplification of design principles, new researchers can leverage these case studies as a blueprint to address specific robotics challenges. This includes designing new robots, enhancing the performance of existing robotic systems, and integrating new functionalities into robotic systems.

- Detailed design, modeling, and experimentation for soft and semi-rigid robots. I provide a comprehensive collection of examples demonstrating how these skills can be applied to address a robotics research question.

- A low-cost robot design principle embodied throughout the dissertation. Together with the proposed methodologies and approaches, each case study tackles its respective research objectives using cost-effective, minimal material solutions.

Further contributions, especially the detail-led technical contributions of each research case, will be detailed in their respective chapters. The remaining chapters of

the dissertation are organized as follows: Chapter 2 first introduces the relevant background of each case study, followed by a brief description of experimental design that is used in this dissertation. Chapter 3 to 5 then introduces each case study, with a brief introduction summarizing the methodologies and connection to the dissertation. The dissertation then concludes in Chapter 6.

Chapter 2

BACKGROUND AND METHODOLOGY

2.1 Granular Media and Low-Re Environment Locomotion

2.1.1 The "Scallop Theorem"

Animals' ability to locomote through a variety of media like sand, dirt, and fluid is a complex product of the force interactions between the musculo-skeletal systems of these animals and the medium that surrounds them [37, 50, 19, 52]. A well known concept from literature, known as the "Scallop Theorem", states that if a swimmer in a low Reynolds number fluid environment performs a reciprocal behavior, zero net movements will be generated [89]. Indeed, for a number of more complex organisms such as bony fish, the motion of fins, spines, and other active subsystems have been observed to proceed through non-reciprocating trajectories such as rowing, cupping, and undulation[64, 19]. For simpler organisms, however, including the body's compliance such as the "flexible oar" may serve as a straightforward approach to breaking symmetry [89].

2.1.2 Flexible foil Locomotion

Driving flexible filaments or foils to swim, propel or generate force in a viscous fluidic environment has been demonstrated as an efficient way to generate non-reciprocating motion [89]. The motion of "elastic swimmers" with rigid bodies and slender, elastic tails have been described, using the compliance of the tail section to solve for the swimming kinematics such as shape, velocities and force balancing in the case of small amplitude oscillations [51].

In another example, a flexible flapping model using a torsional spring as a compliant element has been used to study the locomotion of slender bodies in viscous fluids and granular media [83]; in this study, however, the compliance in the proposed wing-flapping mechanism exists only at the proximal joint of a rigid beam, rather than distributed along the beam as in an Euler-Bernoulli formation. In a second paper by the same group, the stiffness of a filament was varied along its length, providing new design principles for maximizing the propulsion of micro-swimmers[84]. Finally, the study of flexible plates and foils has been extended to frictional environments such as granular media with numerical solutions for the static force balance and curvature of continuum plates moving through soil[116]. These papers serve as a theoretical starting point for our current work.

2.1.3 Bio-inspired granular robot

Researchers have also developed a variety of swimming or digging robots inspired by this biological phenomenon to create non reciprocal motion trajectories. This includes high degree-of-freedom mechanisms[71, 68] or pneumatic chambers[81, 39, 105, 104]. Without the musculo-skeletal systems found in many digging/swimming animals, there are few simple techniques for thoughtfully adding compliance to mimic the natural swimming and digging capabilities found in nature. One natural place to add compliance and break the symmetry of a simple flapping motion is in leg or fin-like digging appendages.

Flexible and compliant materials have been used to mimic the biological gaits of digging animals. Shoele and Zhu showed nonuniform flexibility in insect wing designs could lead to higher lift force in air with low energy consumption comparing to rigid wings [100]. Nian et al [78] analyzed a flexible wing with a one-sided stop at the joint. In aerodynamics, using asymmetry in the deformation between upward and

downward has been shown to increase the wing performance with higher force and lower energy consumption. [111, 76].

In granular media, using asymmetric fin designs for propulsion has been less explored. Russell developed a burrowing robot [95] inspired by the Mole Crab, an animal that maximizes thrust in its power stroke and minimizes drag in its recovery stroke through careful configuration of its leg pairs [109]. This robot utilizes flexible sheets and a rigid stop in the fin design to break symmetry and permit forward motion in sand.

2.1.4 Granular media resistive force theory (RFT)

Granular Resistive Force Theory (RFT) [65], has been used to model the propulsive forces of organisms with low Reynolds numbers [30] as well as used in the design, analysis, and optimization of robots [66, 28, 57, 125].

In Chapter. 3 of this dissertation, granular RFT has been integrated into a dynamics simulation package called Pynamics [1] , which is a Python based dynamics simulation library that uses Kane's method to derive symbolic equations of motion [55, 99]. The RFT-based force, material properties, experimental parameters are implemented into Pynamics to replicate the system and optimize the design. Other alternative, such as Discrete Element Method (DEM) [93] coupled with Finite Element Method (FEM)-based simulations [74, 110, 33] are potentially suitable to predict the force interactions between particles and compliant intruders but incur high computational costs and take much longer, reducing their usefulness in optimization-based approaches.

[1] `https://github.com/dli-sys/Pynamics_demo_for_compliant_fin_ral`

2.2 Wearable robots

2.2.1 Wearable robots for human walking assistance

Exoskeleton

A variety of rigid exoskeletons have been developed for improving mobility over the decades[85, 46, 126, 88, 16, 114]. High forces and torques provided by those rigid exoskeletons assist the ankle, hip and/or knee, facilitating activities such as walking or lifting heavy objects. However, due to the complexity of the human musculoskeletal system, adjusting and aligning human and robot joints has proven difficult, increasing the metabolic cost of the wearer and the external energy expenditure of the attached system. Heavy, high-torque, and often non-backdriveable systems can also be a safety risk for the wearer when the control system fails or misalignments occur [112, 90].

Exo-suit

More recent innovations in soft robotic techniques [20, 73, 7, 91] have resulted in "exo-suit" style technology in which tendons routed through Bowden cables provide pulling forces across joints. While this has addressed many of the issues stemming from traditional exoskeleton designs, it has also resulted in increased forces across human joints, which can lead, over time, to damaging the user's joints through increased wear [47]. Furthermore, wearable robotic orthoses often fail to break even on metabolic cost, although there have been some notable recent exceptions [92, 56, 20].

Current wearable robot limitations

One common nuance of a number of exo-skeletons/suits is that they are often designed and tuned for one purpose, such as lifting, walking, running, or carrying loads. Fewer

wearable devices provide the versatility required to be worn as a multipurpose device throughout the day, again with notable exceptions [94, 101, 18].

Many of the above wearable robotic systems employ active sensing and feedback control techniques to quickly respond to the wearer's motion and provide powered assistance both to assist the user as well as to offset the extra weight of the system itself. In many cases, however, the small control delays imposed by digital control techniques also add small but perceptible loads to the wearer that can over time lead to accelerated fatigue and reduced efficacy [96].

Thus a middle ground between soft and rigid solutions is still desired, in which wearable systems provide alternate loading pathways across joints, where a variety of capabilities can be enabled or disabled on-demand based on the user's activity, and in which the trade-off between wearability and utility is made not through the use of active, timed, energy addition via powered joints, but by minimizing the weight of rigid systems, and by powering the system to change its state.

2.2.2 Added metabolic cost and load carriage

Loaded mass or load carriage-induced metabolic costs have been well studied in elderly people during walking [31, 106, 29]. To create such "transparency" while preventing motion when engaged, one design approach is to reduce the overall weight of the device. Utilizing structural element within compliant mechanisms can be alternative method to meet this weight requirement.

Past literature has also established that metabolic cost increases with increased load [31, 106], and that the user will have more difficulty maintaining their center of mass. However, under certain load carriage cases, increased metabolic cost does not increase fatigue or reduce performance significantly. According to [29], for elderly human subjects (70 kg), payloads less than three percent (2.1kg) of the human body

do not significantly impact the wearer [9, 10]. Therefore, one design criterion is to keep our system weight below this value. Additionally the distribution of the load at the posterior of the trunk helps minimize metabolic cost by keeping system loads closer to the user's center of mass [106].

2.3 Locking solutions in robotics

Lockable solutions in robotics can generally be divided into three categories: 1) singularity locking , 2) frictional locking and 3) mechanical locking [86]. Singularity-based locking, such as four-bar linkage are less common in robotics applications due to their large size and the restricted locking position although their power consumption is low, only requires energy when switching states, seen in a knee locking mechanism that use four-bar linkage to restrict leg angle for a walking robot [113] and an energy efficient prosthesis based on four-bar mechanism [13].

2.3.1 Frictional locking

Frictional locking, including capstans [40, 72, 107], dielectric [5], non-backdrivable gears [38] and self amplifying clutches [48] relies on a negative force gradient applied in the normal direction to generate a friction force, thus prevent motion between two parts. To remain in the locked state, frictional locking solutions often require the actuation source to continue engaging in order to provide the normal force, increasing power consumption.

2.3.2 Laminar jamming

Layer jamming in particular has proven itself compact and lightweight while providing high locking forces [1, 77, 53, 61, 97, 49, 22, 102], as it can multiply friction through multi-layer structures; these have been applied to a number of robotic and

variable-stiffness mechanism designs.

This technique typically employs a negative pressure gradient [1, 60, 14, 121, 43] over soft membranes, either within a bag or distributed across a planar surface, to bring layered sliding materials into close contact, with a few exceptions [115, 41, 62]. As the pressure grows, the friction between layers increases to slow and stop relative motion between layers. Pneumatic-based jamming, however, necessitates high-pressure negative differential pressures, which must be supplied by a vacuum pump. This is less ideal for compact, portable designs that must be worn, because the size and weight of these pumps can be exceedingly large in order to achieve the required pressures through narrow tubing in a short amount of time.

Mechanical clamping-inspired jamming[44, 63, 53] can address some of those issues, permitting small, non-backdriveable motors to generate high normal forces; we have thus selected this approach in our current prototype.

However, the associated challenges of these systems are not thoroughly explored in the literature. For example, the use of pneumatic systems necessitates incorporating tubes and vacuum pumps, potentially increasing the overall weight and reducing response speed, especially during recovery. Likewise, many frictional locks, including jamming structures, need small but continuous power input to remain locked, or require two actuators for switching between locked and unlocked states, which may increase system mass and total energy consumption. Furthermore, vacuum-based jamming applications often face limitations in their range of motion due to the requirement for an airtight envelope.

2.3.3 Mechanical locking

Mechanical locking systems that rely on mechanism design are widely present in engineering and academic research. As they often utilize motors to direct-drive locking

parts, high-speed responses can be observed, alongside reduced design complexity. However, these mechanisms, on the other hand, use interference to prevent movement between two parts, often in a discrete way – as in a ratchet/pawl – meaning that the resolution of the output position is limited when locked. Examples can be seen in ratchet systems for a robotic gripper [32] and a latch design for a walking robot and energy harvesting [17].

2.3.4 Towards a hybrid locking solution

One can combine these two categories of locking strategies to avoid their own disadvantages. The coupling of *mechanical* and *frictional* locking permits an infinite number of stable locations and low energy consumption. Additionally, avoiding direct-driving the motor or only engaging in contact between those two components when switching states allows for lower power consumption and smaller actuation forces. For example, Plooij et al [87] utilize a statically-balanced brake that disengages its clamping mechanism and frictional pad, allowing small actuators to control a high locking force. Similarly, Chou et al utilize a buckling beam-based bistable mechanical structure to actuate a friction pad for optical operations [15], disengaging the payload with the actuation unit.

This was also seen in some self-locking solutions. Self-locking mechanisms are often passive, so in the absence of active initialization and reconfiguration, the unlocking speed can be slow, with a few notable exceptions highlighted in recent research [23]. Our research is particularly interested in such mechanisms, as they allow unlimited locking positions, making them more suitable for wearable applications that require accommodation for highly variable human motions in many positions.

Chapter 3

COMPLIANT FINS FOR LOCOMOTION IN GRANULAR MEDIA

3.1 Introduction

In this chapter, I present an approach to study the behavior of compliant plates in granular media and optimize the performance of a robot that utilizes this technique for mobility. From previous work and fundamental tests on thin plate force generation inside granular media, we introduce an origami-inspired mechanism with non-linear compliance in the joints that can be used in granular propulsion. This concept utilizes one-sided joint limits to create an asymmetric gait cycle that avoids more complicated alternatives often found in other swimming/digging robots. To analyze its locomotion as well as its shape and propulsive force, we utilize granular Resistive Force Theory (RFT) as a starting point. Adding compliance to this theory enables us to predict the time-based evolution of compliant plates when they are dragged and rotated. It also permits more rational design of swimming robots where fin design variables may be optimized against the characteristics of the granular medium. This is done using a Python-based dynamic simulation library to model the deformation of the plates and optimize aspects of the robot's gait. Finally, we prototype and test robot with a gait optimized using the modelling techniques mentioned above[58].

3.2 Statement of Designs and Experimental Methods

This chapter provide the following examples and technical contributions for soft robotics study:

1): A 3D-printed origami-inspired fin with "directional" stiffness, seen in Sec. 3.3.2

and Fig. 3.1. Inspired by the origami-inspired design that consists of rigid, flexible and adhesive layers with hinge design, I select a 3D-printed method to co-print rigid and flexible materials together and use the physical gap between rigid materials as the hinge geometry. ..... (Page: 24);

2): Test setup for granular environment and data collection of load cell force, robot arm distance and shape/location of an object from the camera. This method is mentioned in Sec. 3.3.3 and can be seen in Fig. 3.2. ..... (Page: 25);

3): Compliant Granular RFT modelling – I implement compliant object modelling to a rigid-body dynamics model by adding equivalent springs to the joint. Please refer to Sec. 3.4.1 ..... (Page: 27);

4): Parameter fitting using an optimizer. In this chapter, an example has been shown to solve the granular media and compliant plate parameter, $F_{\parallel}$, $F_{\perp}$ b and k using the compliant RFT model and a CMA-ES optimizer. I calculate the error in the predicted joint angle then utilize the optimizer to minimize the output error, (difference between estimated measured angle) to find the parameter set that best describes both the fin's and environment's properties. A detailed description can be seen in Sec. 3.5.3 ..... (Page: 35)

5): Robot configuration optimization and its experimental validation. Upon obtaining the granular parameters and model of the swimming robot, I select the range of motion for the fin as the input variables and the swimming efficiency as the output. A CMA-ES optimization program is utilized to find the optimal robot configuration and then compared to the experimental validation using the granular media test setup that tracks the robot swimming trajectories, described in Sec. 3.5.4 and Fig. 3.7 ..... (Page: 36).

3.3 Material and Method

3.3.1 Motivation

To navigate through granular media using compliant actuator and a rigid robot as the base, we propose an origami inspired design [79, 80, 119, 108] in which rigid plates are connected by compliant joints to permit bending in one direction. These joints are fabricated out of two layered materials and can effectively act as a one-sided joint limit, as in [42]. The difference in stiffness between forward and reverse motion is then leveraged to break the symmetry of reciprocating motor inputs. To model our digging system, we have selected granular Resistive Force Theory (RFT) [65], which has been used to model the propulsive forces of organisms with low Reynolds numbers [30] as well as used in the design, analysis, and optimization of robots [66, 28, 57, 125].

3.3.2 Compliant Fins for Locomotion

To understand how changing the stiffness of intruders can change the resistive force interactions, we propose three different fin designs including rigid, fully-compliant and origami-inspired plates; we hypothesize that the origami-inspired plate with a one-sided stop can behave differently in different portions of a gait cycle as opposed to the fully rigid and fully compliant plates.

To change the stiffness of the plates in a full gait cycle, we add a joint limit on one side of the fin to permit the flexible sheet/joint to bend only during the recovery portion of a flapping gait. When the origin of the plate oscillates back and forth in the granular media, the fin only bends in the recovery-stroke, recovers to flat while approaching the constraint, and remains rigid against the stop during the power

stroke, effectively behaving as a rigid plate in one direction and a compliant plate in the other. Our intent is to use the difference in thrust force between power and recovery portions of its stroke to generate forward motion. Here we present the plate with unidirectional bending by embedding a joint limit.

The plates of the fins, which can be seen in Fig. 3.1, are printed using soft TPU95 filament [1] with rigid nylon filament [2], in comparison with our selected fully soft design that only uses soft TPU filament. The nylon, when printed on top of the flexible TPU layer, bonds firmly to the TPU and serves as a rigid layer. A 0.05 mm gap separates rigid links, exposing only a small portion of the TPU to bending in one direction. In the other direction, the narrow gap quickly closes, causing interference between neighboring Nylon links, behaving effectively as a joint limit. Fig. 3.1 highlights the geometry and behavior of this plate in comparison to a flexible plate. We replicated the origami/laminate structure [79, 119, 108] using a 3D-printing approach, where the nylon serves as to rigidze the sheet and TPU serves as the flexure joint. The gap between nylon links permits bending in one direction while acting as a joint limit in the other. The nylon and TPU 95A bond during the printing process, eliminating the need for an explicit adhesive layer.

3.3.3 Test Setup and Data Collection

I use the test setup illustrated in Fig. 3.2 to measure force, control displacement and track markers' position in the experiments. The mounting side of a 6-DOF force/torque sensor [3] is connected to the end of a robot arm [4]. The intruders and fins are mounted to the tool side of the sensor with different custom attachments in

[1] Ultimaker TPU 95A 2.75mm

[2] Ultimaker Nylon 2.75mm

[3] ATI Gamma F/T Sensor

[4] Universal robot, UR5

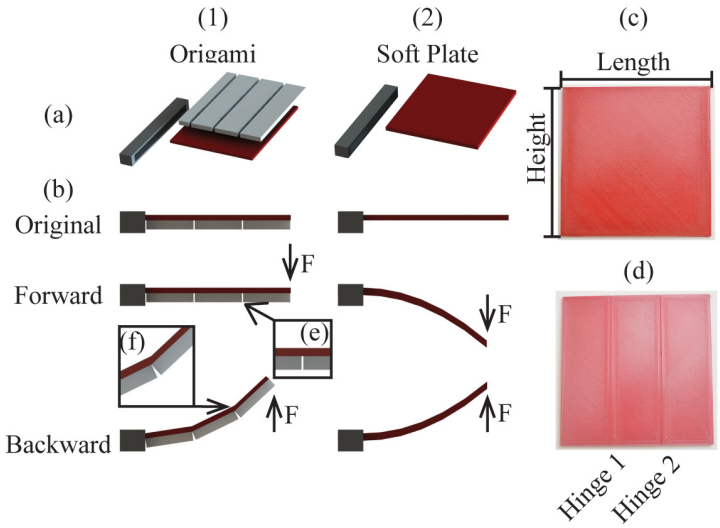

Figure 3.1. Compliant fin design and manufacturing. Column (1) is the origami plate while (2) is the soft plate. (a) Assembling of the parts in the fin: gray material stands for frame, printed by conventional PLA filament; red layers are printed with red Ultimaker TPU 95A as flexible sheet and white plates are made with Ultimaker transparent nylon. (b) The bending of the actuator plates and effect of the stops; in (b-1), the nylon acts as the rigid stop. (b-2) The normal flexible plate has no stop mechanism thus can bend in two directions. Due to the accuracy and line width of our printer, we draw the hinge in our 3D design with a gap of 0.4mm. When finished, the printed plates have a gap of 0.05mm and do not permit bending beyond the nylon surface. (c) Printed soft plate. (d) Printed origami plate with two hinges. (e) and (f) Enlarged view for the origami hinge and rigid stop in normal and bending states respectively.

various tests; these are inserted into a box filled with glass beads. Currently, the average particle diameter, d_g, is 4mm. The robot arm is programmed to hold, drag or rotate the object using a Python script, which also records the markers' locations over time using a motion-capturing camera system [5] .

To track the deformation inside the glass beads, we attach the OptiTrack markers using extension rods (diameter = 1 mm) along each joint axis so that they can be seen above the beads, as in Fig. 3.2 (b). Four markers are placed onf the plate

[5]Motive OptiTrack

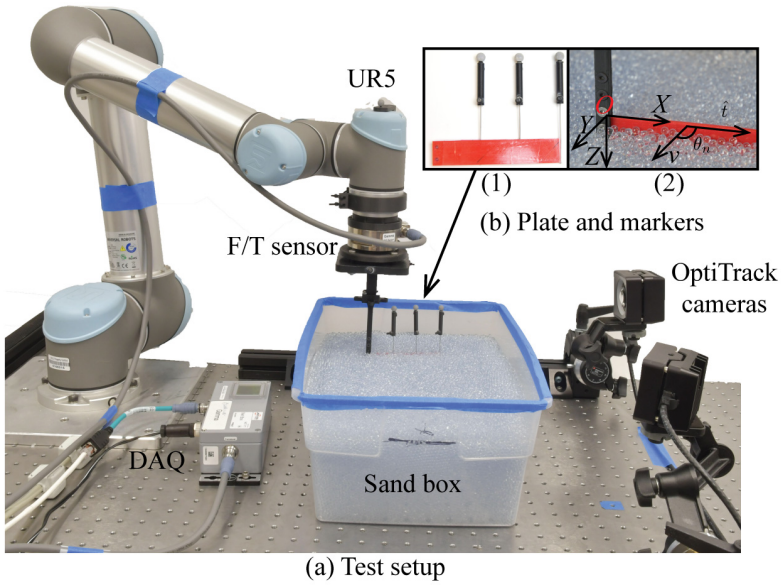

Figure 3.2. The granular propulsion fin experimental test setup. (a) shows the test setup used in this study, including a UR5 robot arm, an ATI Gamma Force/Torque sensor with DAQ, and a group of OptiTrack cameras. The plate is attached to the test setup using a custom 3D-printed attachment and inserted into the box placed on the test table. OptiTrack markers are connected to tiny steel rod that mounted to the plate. The cameras are moved for pictures, (b): A closer look of the plate. In (b-1), the markers are placed on the plate using the extension rods and (b-2) illustrates how the plate is inserted into the box and the local coordinate of the plate.

and on the center of UR5 end effector, aligning with the origin of the plates. The markers attached to the intruder are mounted so as to obtain its location, curvature and displacement. The maximum error introduced on force estimates due to twisting in the YZ-plane is less than 0.3%, which is thus ignored.

3.4 Theory and Model

3.4.1 Granular Resistive Force Theory (RFT) for Compliant Body

Consider a multi-link intruder moving within a frictional, granular environment as seen in Fig 3.3. As it is dragged through the medium it bends and deforms through

its interactions with the glass beads. If starting from rest in its undeformed flat state, the final configuration of a compliant intruder will adapt to achieve a minimum energy configuration, impacting the forces it imparts on the media; in contrast, a rigid plate, dragged through the soil, will see far smaller deflections and higher forces; its effective configuration after being dragged remains unchanged, and its force interactions can be completely described by traditional RFT. The goal of our modeling approach is to consider the effect of compliance, which will require augmenting current RFT theory. This has been considered previously by Peng et al [84], but applied to problems without changing stiffness in the gait cycle, such as a rigid slender body with torsional spring at the origin or a flexible filament that can bends in both directions.

A compliance-augmented granular RFT model will provide a more convenient way to model flexible materials interacting with granular material, and will permit more rapid analysis and optimization of compliant sand swimmers and diggers. We propose to utilize this theory to model our fins and better understand robot locomotion in granular media.

To demonstrate how compliance could be applied to RFT on our origami inspired plate, we first consider a three-link plate, seen in Fig. 3.3, where the linkages are equally spaced along the long edge of the plate.

The plate, with height, L_p, linkage number $N = 3$ and joint stiffness/equivalent spring constant at hinge, k, is placed vertically in the xy-plane and dragged inside the bulk material at a speed v_p with angle of attack, θ_p, as shown in Fig. 3.3(a). The normal and tangential vector of plate i are $\hat{\boldsymbol{n}}_{\boldsymbol{i}}$ and $\hat{\boldsymbol{t}}_{\boldsymbol{i}}$ respectively; the angle of attack of the plate can thus be written as $\theta_p = \angle(\hat{\boldsymbol{t}}, \hat{\boldsymbol{v}})$. Based on previous work focusing on the effect of intruder speed on dragging force in granular material, we assume that the resistive force on the plate, F_p is insensitive to speed at low, friction-dominating speeds [118, 2, 3, 65]. In traditional granular RFT, the resistive force in the moving

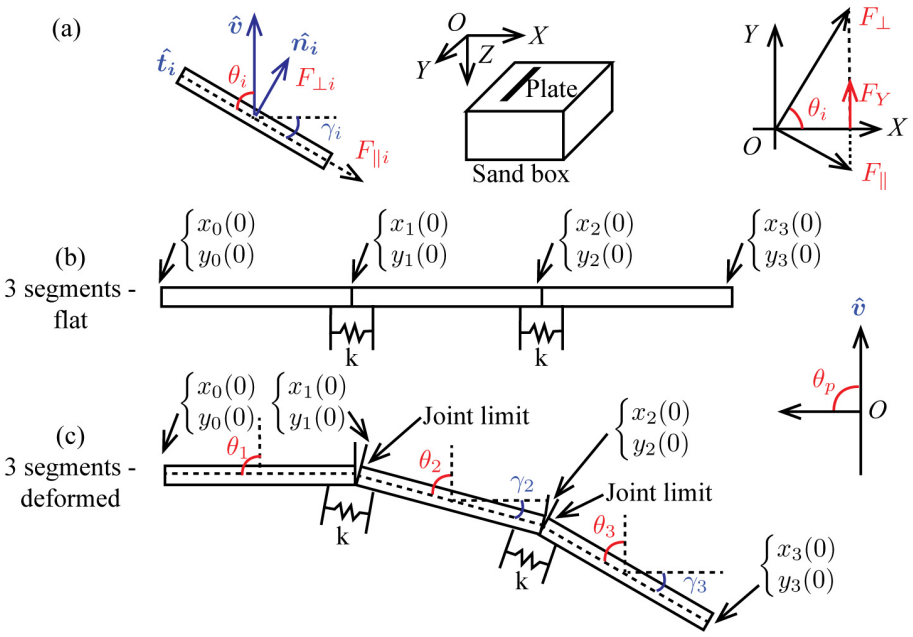

Figure 3.3. Granular RFT model for compliant plate. (a) On the left side, we show a single segment from (c), v is the direction of the velocity, $\hat{\boldsymbol{n}}_{\boldsymbol{i}}$, $\hat{\boldsymbol{t}}_{\boldsymbol{i}}$ indicate the normal and tangential direction of the plate, θ_i is the angle of attack of i-th segment of the plate and γ_i is the angle of twist of each segment, where $\theta_i + \gamma_i = 90°$; the other two represents the local coordinate of the test setup and the propulsive/resistive force, F_Y. (b) An undeformed plate with 3 segments at $t = 0$, the equations under the plate show the position of each point along the hinge. On the right side of (b), we show the local frame of the plate. In (c), we highlighted the deformed, final geometry of this origami inspired plate at later time t_f. In (b) and (c), we also showed how equivalent springs and stops were placed on the plate.

direction on a equivalent rigid plate ($N = 0$) moving at steady state is calculated using

$$\mathbf{F_p} = \int_0^L (d\mathbf{F}_\perp sin(\theta_p) - d\mathbf{F}_\parallel cos(\theta_p)) \tag{3.1}$$

where $dF_\parallel$ and $dF_\perp$ are the force derivatives per element.

3.4.2 Compliant RFT for 3-Link Origami Plate

We now consider the case for a three-link origami-inspired compliant plate, where the length of each segment l equals $\frac{L_p}{N}, (N = 3)$; θ_i stands for the angle of attack for each segment. In granular RFT, force on individual segments are only influenced by the field of the local granular material; we can thus assume that for all segments, $dF_{\|i}$ and $dF_{\perp i}$ remain the same, given that the granular media remains in a quasi-static state.

The instantaneous position of the joint on plate i can be seen in Fig. 3.3, as indicated by $x_i(t)$ and $y_i(t)$. The force acting on each joint can be expressed as F_{Yi},

$$F_{Y_i} = \int_0^{\frac{L}{N}} (d\mathbf{F}_{\perp} sin(\theta_i) - d\mathbf{F}_{\|} cos(\theta_i)) \tag{3.2}$$

Note that when $i = 1$, θ_0 refers to θ_p, which is the angle of attack about the axis located at the origin. In this case, after sufficient time, the intruder traveling at constant velocity v reaches a final state at time t_f, at which point the resistive force and geometry of the plate remains steady. For instance, when the plate is placed vertically in glass beads and dragged at a constant speed v at angle of attack 90°, the boundary conditions will be as follows:

$$\begin{cases} x_0(0) = 0 \\ y_0(t) = vt \\ x_N(0) = L_p \\ y_N(0) = 0 \\ \theta_p(t) = 90^\circ \end{cases} \tag{3.3}$$

The decomposed segments and connection between the plate are connected to our test setup, as shown in Fig. 3.3. We may calculate the steady state configuration of the system at t_f by tracking the position of the markers attached to the plate,

which permits us to track the position and deformation of the compliant intruder. This configuration corresponds to the steady-state force-balance between the internal compliance of the fin and the external forces exerted by the granular media as it moves.

3.5 Result and Analysis

3.5.1 Compliant Fin Dragging and Rotating Test

Though this robot's proposed actuation is based on rotation, as seen in Fig. 3.7, we believe that dragging tests and results may be extended to rotation cases and can help us to gain insights into the contribution of compliant plates as well as compare the merits of different designs.

The force vs. distance and torque vs. angle for linear and rotational cases, respectively, are plotted in Fig. 3.4. Compared to a rigid plate, the force, F_p for soft plates (blue and cyan) is lower due to a smaller effective profile in the direction of motion when deformed in the forward and reverse directions. A symmetric pattern is observed for rigid and soft plates. The origami plate, with a one-sided rigid stop and compliance in the other direction, shows a different pattern in contrast. As seen in Fig. 3.4(2), the origami-inspired plate in red produces an asymmetric force-displacement histogram in its power and recovery stroke. We observe that, by introducing stops, the new curve overlaps with the forces exerted on the rigid plate (black) in the power stroke, and much more closely tracks the forces exerted on the soft plate (blue) in the initial portion of the recovery stroke. The force near the end of the recovery stroke slowly deviates toward the rigid limit, which we attribute to a higher equivalent stiffness compared to the soft plate.

In the case of rotation, we find similar results. In Fig. 3.4(4), compared to the

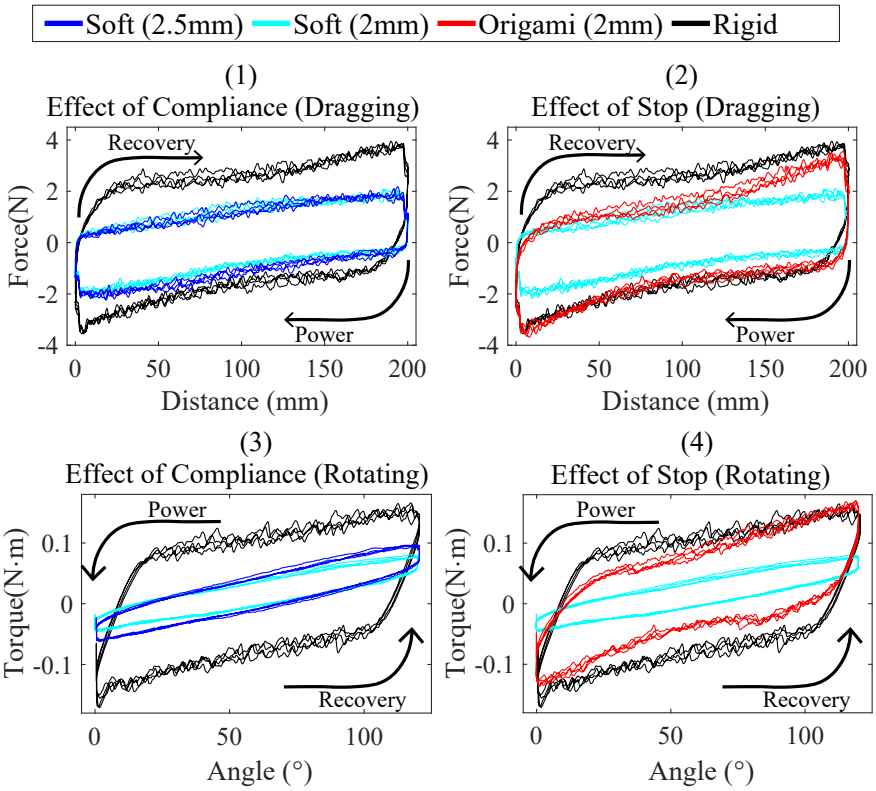

Figure 3.4. Dragging and rotating results. The legend on the top indicates the plate type. These sub-figures show how the force/torque change corresponding to the distance/angle. For example, in (1) and (2), the plate moves from 0 mm to 200 mm as recovery stroke (upper and left) then is dragged back to the origin in the power stroke (lower and right). (1) and (2) show the dragging results, where rigid and soft (2mm) are shown in both (1) and (2). In contrast, soft (2.5mm) is only presented in (1) and origami (2mm) can be seen in(2). Following the same principles, (3) and (4) indicate the rotating results.

soft plate, the torque generated by the origami-inspired plate can effectively act as a rigid plate in the power stroke. In the recovery stroke, we find the torque of the origami-inspired plate is higher than the compliant continuum plate in Fig. 3.4(3), due to the differences in the thickness and equivalent stiffness between the origami plate and fully compliant plate. We may use this finding to design our robot by integrating joint limits into the fin design, thus breaking symmetry.

3.5.2 Effective Flapping for Compliant Plates

When an origami plate is dragged inside a granular medium from origin D_0, the plate will reach a maximum deflection as the dragging distance reaches D_{f1}. Once the maximum deflection is reached, the resistive forces of the plate remain constant. A displacement in the opposite direction will drive the plate towards its original shape, where the threshold value required for the plate to return its original shape is D^r_{f1}. If the plate doesn't start to bend in the opposite direction as it returns to its origin, we refer to this as "Small amplitude oscillation", as seen in Fig. 3.5(a-1). However, if the plate's amplitude increases and a change of the direction occurs at D_{f2} ($D_{f2} > D_{f1}$) when oscillating back, the plate will recover to a flat shape at $D_{f2} - D^r_{f1}$.

At a constant speed the plate's configuration remains constant after $-D^r_{f1}$ when traveling back to the origin; we refer this scenario as "Large amplitude oscillation", as shown in Fig. 3.5(a-2). Under large amplitude oscillation, if a unidirectional joint limit is established for $\gamma_i < 0$ (angles of twist in Fig. 3.3), the joint limit will break motion symmetry, and non-zero total thrust forces will be produced over a full power/recovery stroke during $(D_{f2} - D^r_{f1})$ to D_0, as in the right side of Fig. 3.5(a-3). We refer this phenomenon as "Effective Flapping".

Thus in the design of the fin, an important guideline is to ensure that the amplitude of the fin is larger than D_{f1} so as to guarantee nonzero net force. In Fig. 3.5(b-3), we observe that, when dragged back, the markers' locations indicate that a small amount of bending occurs when $\gamma_i < 0$; this can be attributed to a number of potential reasons: (1) Error between the marker attached to the end of the extension rod; (2) a non-zero joint limit due to geometric differences between the ideal and prototyped plate; or (3) because the rigid material's stiffness plays a role in establishing a high – but not infinite – joint stiffness at the joint. In the following section, we will discuss the

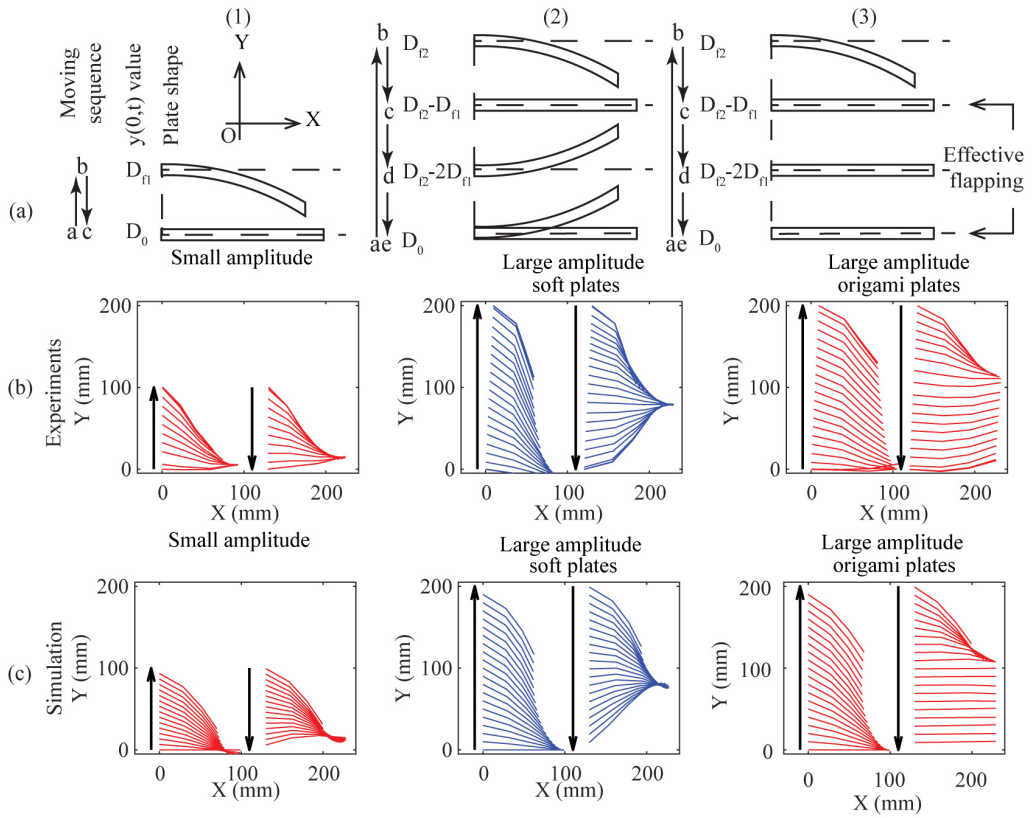

Figure 3.5. Concepts of effective flapping. Column (1): Small amplitude oscillations; (2) Large amplitude oscillation for flexible plate. (a-3) Large amplitude oscillation for the origami plate. Row (a) shows a schematic diagram of the bending of the plate. Letters, arrows and notations on the left side of each sub-figure indicates the moving sequence and distances (value of $y(0,t)$), following alphabetical order; we plot the local coordinate frame on the upper-right corner of (a-1). In row (b) and (c), we show the bending process of plate dragging tests corresponding to row (a) from experimental data and simulations using Pynamics, respectively. The legends indicate the plate types. In each sub-figure, the arrows in row (b) and (c) show the dragging directions. And on the left side, we show the power strokes and the right hand sides are the recovery strokes.

simulation result using Pynamics.

3.5.3 Simulation of Compliant Plate Dragging

To simulate the plate's motion, we first define a 3-link origami-inspired plate with the extension rod as a 4-link serial chain of links connected by pin joints, where the first linkage is the extension rod and the next three links correspond to the segments of the origami-inspired plate. The forces and torques applied to each individual plate include the forces due to the granular RFT model ($dF_{\perp}, dF_{\parallel}$) applied to the geometric center, and an equivalent torsional spring applied to each joint, representing material-based compliance as a linear constant k in the soft direction. These values are obtained by experimental measurement using our test setup. To model the joint limit's stiffness when $\gamma_i < 0$, we apply an arbitrarily large spring constant, $k_r = 10000\,\mathrm{N/rad}$. Also added to the model is a rotational damper located at each joint, whose damping ratio, b, is used to model the loss within the soft material itself. Other dynamic parameters include mass and inertia, which are obtained based on the density and geometry of the materials used and essential for solving for acceleration prior to integration in Pynamics.

With the parameters described above, one can obtain the time-based motion of the system in our dynamic model as a function of specific motion or force inputs. To replicate the motion data obtained experimentally for the origami-inspired plate, we supply a motion constraint for v, the forward dragging velocity. We supply the previously obtained experimental values for $dF_{\parallel}$, $dF_{\perp}$ and k as system constants, while the value for b is solved iteratively using the Covariance Matrix Adaptation Evolution Strategy (CMA-ES), which is provided in Python via the pycma [34] package. In order to do this, b and v are supplied as inputs to a function for calculating the angles of twist of each joint (γ_1, γ_2, γ_3) through time, t, as:

$$F_{Sim}(b, v, t) = [\gamma_{s1}, \gamma_{s2}, \gamma_{s3}]^T \tag{3.4}$$

In comparison, we can thus write the experimental system's state as:

$$F_{Exp}(v,t) = [\gamma_1, \gamma_2, \gamma_3]^T \tag{3.5}$$

To obtain the joint damping ratio, b, we first calculate the Mean Squared Error (MSE) for the joint angles over time as an error function:

$$E(b) = \sum_{v=10}^{50} \frac{(F_{Sim}(b,v,t) - F_{Exp}(v,t))^2}{5} \tag{3.6}$$

We then solve $E(b)$ using pycma to find the value of b via:

$$min \;\; E(b) \tag{3.7}$$

3.5.4 Sand-swimming Robot Design and Tests

To determine if the plates can be used in the generation of motion, we introduce a full robot model consisting of a body and two origami-inspired fins. We adapt the basic mechanical design of our robot from the sand-burrowing robot in [95]. Our robot, seen in Fig. 3.7(a) and (b), consists of a 3D-printed case and two bilaterally-symmetric sets of servos and fins, attached to the main body of mass, M_r, height, H_r, width, W_r, and length, L_r. The servo angles are represented by Θ_1 and Θ_2, and the resistive force in the moving direction is represented by F_r. The robot servos are connected and controlled by an Arduino Uno using PWM signals sent from an attached computer.

To select a set of feasible parameters of the robot, we first consider that the resistive force for the robot body should be minimized. In granular RFT, resistive force increases with the cross section; we thus select the robot body with the following parameters: $H_r = 45\,\text{mm}$, $W_r = 55\,\text{mm}$, $L_r = 75\,\text{mm}$ and $M_r = 220\,\text{g}$. These are

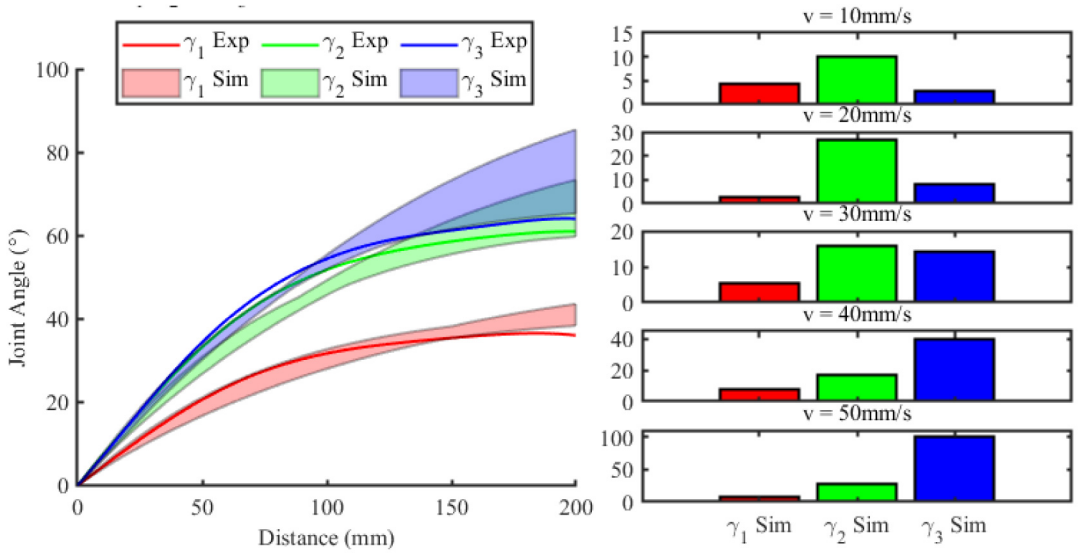

(a) $\gamma_1, \gamma_2, \gamma_3$ Exp. vs. Sim.

(b) MSE between Sim. and Exp.

Figure 3.6. Simulation result of plate deformation using Pynamics. In (a), we show the joint angles over distance comparing to the simulation result. Solid lines show the mean of the experimental values of γ_1, γ_2 and γ_3. The transparent region shows the range of simulation results across five speeds (10mm/s - 50mm/s), where the height of the variation stands for the minimum and maximum simulated values for each position in mm. Column (b) indicates the MSE of each speed between the simulation and experiments. Each row inside is the MSE between the simulation result and the experimental data at the same velocity. Red, green and blue bars stand for γ_1, γ_2 and γ_3, respectively.

the minimum sizes and corresponding masses we can design and manufacture to accommodate the servos. Constrained by the size of robot body, we select the length of the plate, L_p of 60 mm and the height of the plate, H_p as 55 mm to accommodate the robot arm and actuator frame. We define the minimum value of the length of the robot arm, L_a as 60 mm, which is the lowest value we could select to allow the full range of motion. After selecting these parameters, we mount the plates to the robot then mount the system to our test setup, inserting it into the box in preparation for the next step.

To utilize RFT-based deformation found in Sec. 3.5.3 and Sec. 3.5.2, we obtain a new set of $dF_{\perp}$ and $dF_{\parallel}$ values. This is due to differences in the sizes and depth of the plates from the previous section.

When the robot is on, servos flap the fins of length L_a between Θ_1 and Θ_2. We define the power stroke as the portion of the stroke when the fins rotate from Θ_1 to Θ_2; the remainder of the stroke is defined as the recovery stroke. During the power stroke, the robot moves forward for D_1 (mm), while during recovery, the robot moves backward by D_2 (mm). To measure the efficiency of the robot, we define the swimming efficiency as:

$$\eta(\Theta_1, \Theta_2) = \frac{D_1 - D_2}{D_1} \tag{3.8}$$

which represents the proportion of the net displacement, $D_1 - D_2$ in the forward distance, D_1 of the power stroke. As discussed in Sec. 3.5.3 and Fig. 3.6, in RFT-regime, force and deformation of the compliant fin are configuration-dependant rather than velocity-dependent; we conclude that increasing the angular velocity of the inputs will not change the η significantly. Faster-oscillating fins will simply drive the robot at a higher speed. Thus we have selected efficiency as the performance metric.

An optimization strategy was used to optimize the efficiency η by tuning Θ_1, Θ_2 and L_a. In a symmetric gait both sides of the robot are actuated symmetrically; we thus simulated the right half of the robot to increase the optimization speed. The objective function was selected as:

$$min \;\; (1 - \eta(\Theta_1, \Theta_2, L_a)) \tag{3.9}$$

With a minimum value of L_a as 60 mm, the servos and fins have a maximum ranges of motion of $0^\circ \sim 90^\circ$. We thus define the bounds of the optimization of η as $\Theta_1 \in [0^\circ, 90^\circ]$, $\Theta_2 \in [-90^\circ, 0^\circ]$ and $L_a \in$ [60mm, 85mm], where the upper bound of L_a is the longest value we can manufacture. The optimizer found that $\Theta_1 = 60^\circ$,

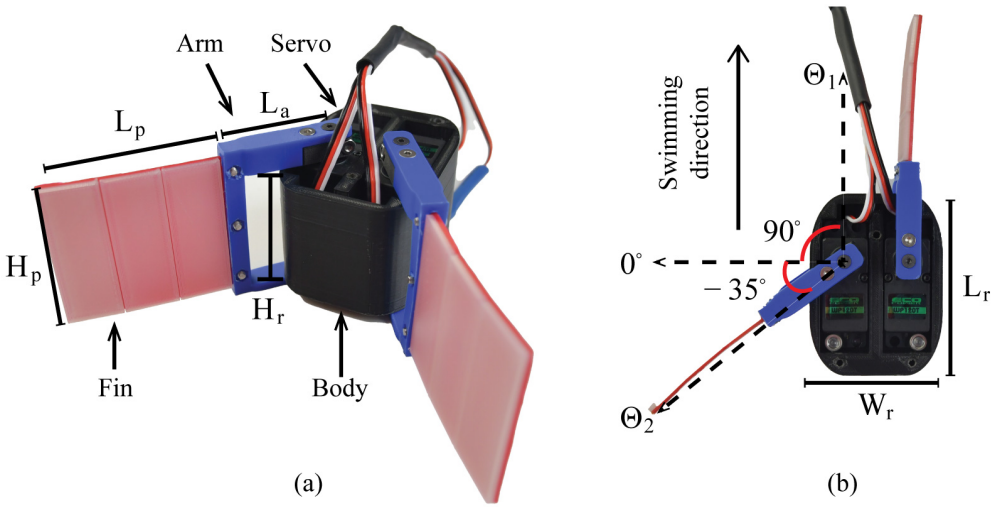

Figure 3.7. The granular swimming robot prototype (a) and (b) are the perspective and top view of the robot, respectively. We also include the design parameter associated with this robot.

Configuration	$\eta_{\mathbf{Exp}}$ (%)	$\eta_{\mathbf{Sim}}$ (%)	**MSE**	Θ_1 (°)	Θ_2 (°)	L_a (mm)	**Net Speed** (mm/s)
Optimized	8.61	8.95	1.2×10^{-5}	60	-90	65	1.69
Symmetry 1	1.22	0.06	1.35×10^{-6}	30	-30	65	0.48
Symmetry 2	1.08	0.05	1.06×10^{-6}	30	-30	75	0.59
Asymmetry 1	3.12	3.71	3.5×10^{-5}	90	0	65	0.34
Asymmetry 2	3.57	3.65	6.4×10^{-7}	90	0	75	0.43
Rigid Fin	0.11	1.02	8.281×10^{-5}	60	-90	65	0.02

Table 3.1: **Robot swimming efficiency vs. configuration**

$\Theta_2 = -90°$ and $L_a = 65$mm produces the maximum swimming efficiency of $\eta_{best} = 8.95\%$.

To measure the swimming efficiency of the flapper robot, we submerge the robot 1 cm deep into the container filled with 4 mm glass beads before each run. During initial experiments, we observe that the robot rolls and rises above the surface of the granular media due to drag-induced lift [21].

This has been addressed in related work by using a wedge attached to the head

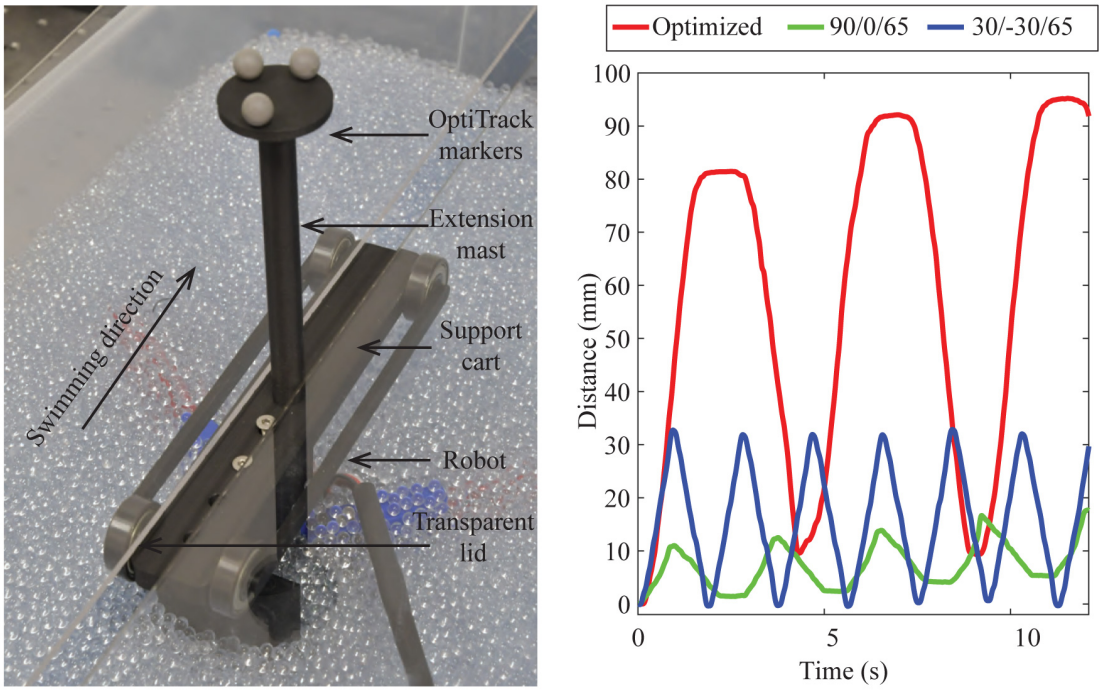

(a) Swimming efficiency test setup

(b) Swimming distance

Figure 3.8. Robot Swimming efficiency experiments and results. (a) shows how the robot is placed in the glass beads with a a support cart with extension mast with markers on the top to track location. (b) illustrates the trajectories of the robot in the moving direction shown in (a) over time in tests for different configurations. Legends indicates the value of Θ_1/Θ_2 / L_a, respectively. For instance, 30/-30°/65 stands for experimental trajectory of configuration, $\Theta_1 = 30°$, $\Theta_2 = -30°$ and $L_a = 65mm$.

of a sand-swimming robot [67]. However, given the small size and minimal design of our robot, adding such a similar wedge would introduce new complexity to the robot that does not directly answer our main research question. To simplify our prototype and experiments, we place a lid on the box and mount the robot to a supporting cart, whose wheels remain in contact with the lid to constrain the robot in a constant horizontal plane at a fixed depth under the granular media. To track the location of the robot under the lid cover, an extension mast with OptiTrack markers is attached to the cart (weight=160 g), permitting the motion of the robot to continue to be

tracked under the beads within the box, as seen in Fig. 3.8(a). We have compared the swimming efficiency of various configurations of the robot's joint limits in Table 3.1 and verified the optimized swimming efficiency from Pynamics experimentally.

Our dynamic model accurately predicts the swimming efficiency of the robot; however, it over-predicts the forward and backward distance covered. This is due to the fact that our current granular RFT model over-estimates the resistive forces and fin deformation, resulting in higher distances covered in both directions. The trajectories of each experiment can be seen in Fig.3.8(b), illustrating the difference in efficiency as a function of gait.

3.6 Conclusion

In this chapter, I have presented an origami-inspired compliant fin for granular locomotion using a new approach for adding plate compliance to a traditional granular RFT model. This has been applied to the model for a two-fin robot and compared to the experimental prototype. I have shown that the time-based evolution of bending and recovering of the fins, modeled by material damping within the fin can be used to improve the swimming performance of a robot.

My results have detailed an approach to understand the principles by which nonlinear compliant materials can be leveraged within granular media, providing potential design simplifications that can reduce control overhead in the future. Although embedding compliance breaks symmetry, given the nature of granular media and the constant compliance, the fins, however, requires a distance/angle to "activate" this symmetry-breaking effect, which brings to my attention that the use of more nonlinear compliance is required to improve propulsion efficiency.

Chapter 4

ORIGAMI-INSPIRED WEARABLE ROBOT FOR TRUNK SUPPORT

4.1 Introduction

In this chapter we propose a new class of wearable robotic devices called "exo-shells" – origami-inspired, multi-link robots with the ability to sense their state and stiffen selected regions on demand to guide, support, and nudge the wearer during daily living activities. Starting with a trunk support robot as a case study, the goal of our current system is to provide supportive forces for maintaining proper posture when avoiding obstacles during walking, with the intent to reduce the chance of slips, trips, and falls. The purpose of this chapter, therefore, is to outline the design and strategy for stiffening, sensing, and understanding its current performance across a wide range of physical considerations. The key contributions of this chapter may be summarized as follows:

1): An origami-inspired design approach to rapidly manufacture and customize wearable robots is presented;

2): The methodology is implemented to create a new serial robot with low resistance and switchable stiffness;

3): Kinematic models are introduced and validated to understand the dimensional requirements for stiffening the robot against external loads using brakes

In Sec. 4.2, I state the design and experimental templates used in this chapter, then introduce the design rationale and describe our approach in the design of each subsystem, along with the kinematic model of the device in Sec. 4.3. Sec. 4.4 then

describes the experimental validation of our subsystems, kinematics, and system. Our paper concludes in Sec. 4.5 with some insights on the future of this research along with our thoughts on the impact of this design. In Sec. 4.2, I introduce and justify the design and experimental templates used in this chapter [59].

4.2 Statement of Designs and Experimental Methods

This chapter provides a study of the following design and experimentation examples:

1): Origami-Inspired manufacturing technique for low-cost wearable robot: The origami-inspired design approach allows for rapid iteration of designs as well as manufacturing of highly capable wearable robots using switchable, passive systems and lightweight materials that remain transparent to the user when inactive. The selected tessellated pattern and manufacturing technique facilitates the production of lightweight, low-cost solutions. A methodology of designing easily-customizable, low-cost wearable devices is introduced, where the wearable system can be adjusted to fit the individual wearer ..... (Page: 44, 46);

2): Wearable "exo-shell" device: The chapter presents a wearable "exo-shell" device inspired by the human spine to improve the gait of elderly individuals during obstacle avoidance tasks. This device is designed and fabricated using the methodologies mentioned above and features a serial chain of lockable joints that can be stiffened using a braking system using a "mix and match" approach towards the selection and use of components ..... (Page: 49);

3): Kinematics and force experiments: this chapter also describes the kinematics

and forces of the proposed device, including 1) the kinematics of rotational links, 2) the two degree-of-freedom, belt-driven parallel mechanism, and 3) full system kinematics consisting of these two mechanisms. We have also introduced an approach for verifying kinematics experimentally and share the Python code for calculation. The kinematic model can be applied to similar mechanisms, especially four-bar cable-driven parallel mechanisms. ..... (Page: 53,62,67);

4): System-level experiments: in this chapter, two system-level experiments were performed, including 1) a measurement of system stiffness and 2) locking response. The general approach toward designing these experiments include synchronizing the force or load, distance or angle, and system time in a single measurement; this approach can be adapted to other tests requiring similar information..... (Page: 70, 72).

4.3 Materials and Methods

4.3.1 Design Rationale

Interventions along the sagittal plane at the wearer's trunk (waist) have been determined to offer the best opportunity for reducing reaction torques in elderly users. This is achieved by providing external stiffness along the trunk, based on preliminary human motion data [69]. To understand the general design principle of trunk support robots, a review of existing supporting devices [120, 54, 36, 82] was conducted, with features compared and summarized in Table. 4.1.

The literature review in Chapter. 2 and the comparison of common trunk support robot features in Table. 4.1 confirm that providing stiffness or locking force on demand and minimizing friction when unlocked are common features. To increase

Robot	**Soft/ Rigid**	**Weight**	**Actuation Method**	**Passive/ Active**
Yang et al [120]	Soft	Not reported	Bowden tubes	Passive
Lee et al [54]	Soft	1.3kg (without battery)	Twisted string actuator	Passive
Heo et al [36]	Rigid	9.2kg	Pneumatic	Active
Park et al [82]	Rigid	Not reported	Linear actuator	Active
This robot	Soft	1.4 kg	Locking	Passive

Table 4.1: Comparison of Trunk Support Robot Features

mobility, these designs tend to focus on creating lightweight structures or propose the integration of a powering unit as future work. As a result, the requirements for a trunk support robot have been identified as follows:

1): Lightweight design;

2): Low power consumption except when changing states;

3): Transparency when disengaged.

For the purposes of our design, the envisioned device is thus attached around the waist and just below the shoulder blades (as seen in Fig. 4.1) and stiffens on demand along the sagittal plane. To create the effect of a continuum system using origami-inspired approaches, we highlight four essential subcomponents of our design: 1) rotational elements, 2) translational elements, 3) a locking mechanism and 4) mounting components. Because the base of the robot is mounted at the wearer's waist and beneath the shoulder blades, our system will need to both rotate and lengthen in order to conform to and support the wearer's back during trunk flexion. Thus, both *rotational* and *translational* degrees of freedom (DOF) are required to fully adapt to the wearer's motion. We propose two basic elements as the building blocks for our device.

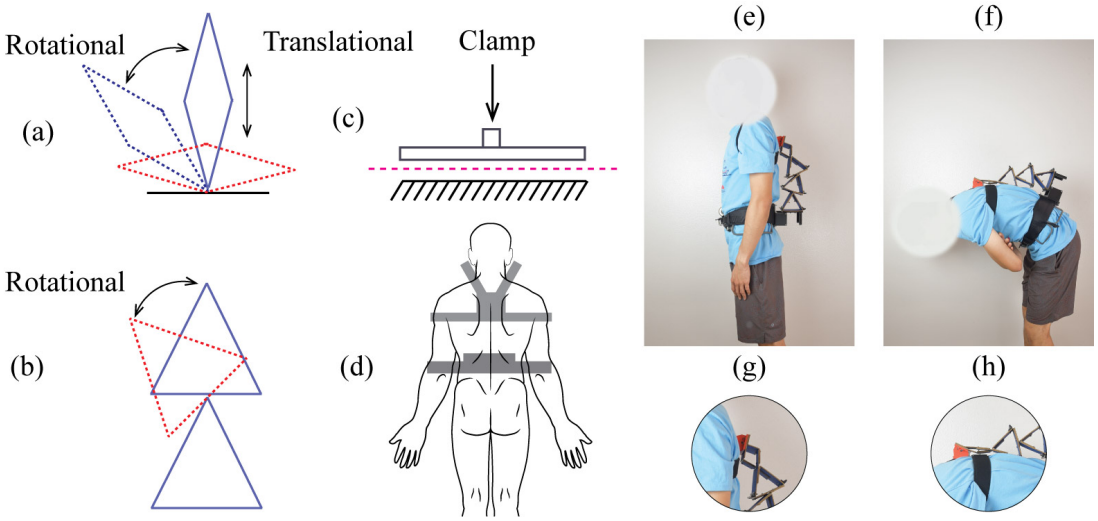

Figure 4.1. Components of the wearable robot. From (a) to (d), we show the four-bar linkage, triangle element, brake and mounting belts, respectively. Subfigures (e) and (f) illustrate the configuration change as a function of posture, where (e) stands for standing straight and (f) shows bending the trunk. We highlight the extraction of the four-bar linkage in (g) and (h). Upon bending, the distal four-bar linkage extends to maximum length to accommodate the human. In this set of figures, we show the robot without break to highlight the structural elements.

We use a laminate fabrication method to construct triangular links that serve as the serial "rotational" elements. Triangles have been selected for these one-DOF rotational elements because, as fundamental elements of trusses, they form stiff, lightweight structures. The outer faces of the triangles serve as simple joint limits to restrict motion to a specific range, as well as the attachment point for our locking system; the range of motion may be adjusted by modifying the triangle's dimensions and proximal connection point. This adjustability serves as a useful way to adapt to individual users while achieving high stiffness using thin materials.

We have also selected a locking four-bar linkage as a secondary, more-complex component because it is capable of both rotation and translation in two degrees of freedom. This component is essential, as mentioned before, for permitting the serial

chain to lengthen along the back during flexion. Fig. 4.5(a). highlights the motion and locking configurations under different external loading conditions.

A number of possible locking solutions have been reviewed for our system; we have selected a mechanical-based jamming brake to lock the system on demand. Brakes, in contrast with actuated joints, are lightweight, respond quickly, and are compatible with tendons attached to multiple moving parts to permit global locking. Mounting components can be selected from a variety of commercially-available hip harnesses, shoulder straps for the upper body, or other custom solutions.

4.3.2 "Exo-Shell" Manufacturing and Device Customization

We adapt concepts from soft robotics [11] and choose origami-inspired, laminate fabrication techniques as the fundamental technology for creating light-weight, high-stiffness, and rapidly-manufacturable wearable mechanisms. Having been applied to a variety of robotic applications [35, 24, 25], origami robots have also been shown to be capable of providing high structural stiffness [75, 124]. Furthermore, the incorporation of sensors into origami structures has proven itself to be a promising method for sensorizing modular origami segments [26, 8]. Following a laminate fabrication approach, as described in [4, 6, 108] the mechanism is designed using 3D computer-aided design (CAD) software.

Each layer of the laminate is generated, exported, and cut with a laser using a custom Python script [1] . The layers of the element are illustrated in Fig. 4.2(g). They consist of a sandwich of two, thick, rigid outer layers of material (Thick cardboard [2] , followed by inner layers of adhesive [3] , a flexible middle layer that serves as a living

[1] https://github.com/iicfcii/laminate-pipeline

[2] Crescent Select Alpha-Cellulose Matboard

[3] DRYTAC MHA25328

hinge [4] , and a flexible circuit layer [5] for mounting and connecting embedded sensors to power and communication. The rigid, adhesive, and hinge layers are cut with a laser cutter [6] ; the flex-circuit layer is manufactured using a masking and chemical etching process. Four copper traces on the flex circuit layer permit communication using the I^2C protocol to each sensor. All the layers are then aligned using locating pins and bonded using a heat press. After the circuit layer is laminated to the other layers, the full laminate is then cut away from remaining scrap with a final release cut.

After the segments are folded into their the final configuration they are serially connected to the next element, as shown in Fig. 4.2(e). Once the positions of the circuit layer components are confirmed, the I^2C bus can then be connected. The conductors from a proximal segment are aligned and connected to the next distal segment so that sensors integrated directly onto the flex circuit can communicate back to the micro-controller located in the base. More details on sensing can be found in Sec. 4.4.1.

To measure joint angles, hall effect sensors [7] are soldered directly on the flex circuit layer and connected to the I^2C bus. In each individual module, the hall effect sensor is mounted as close as possible along the axis of the segment's distal hinge to maintain the sensor's linearity in rotation; a disk magnet is then positioned near the same axis on the next distal segment. With sensor and magnet precisely mounted into the segments, the sensor's signal thus changes as the distal link rotates. The location of the sensor and magnet can be seen in Fig. 2(d) and (e) of the main manuscript. the calculation of the joint angle using these values is discussed further in Sec. 4.4.1.

[4] Grafix Dura-Lar 5 mil

[5] DuPont Pyralux AP Copper-Clad Laminate ap7163e

[6] Epilog Fusion M2 75 W CO_2 Laser cutter

[7] Silicon Labs Si7210

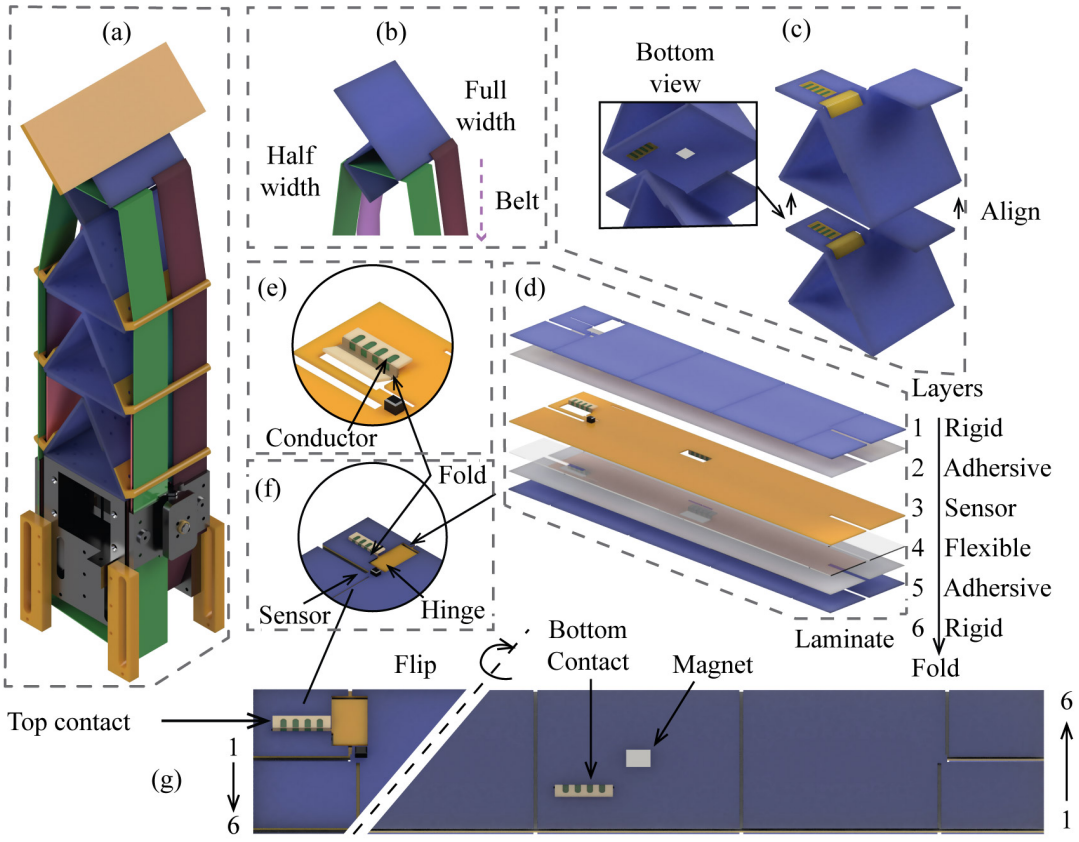

Figure 4.2. Manufacturing of the origami-inspired system. (a) Assembled device. (b) The four-bar segment. (c) Aligned triangle segment with contact pads aligned to the previous segment. (d) Different material layers are stacked and aligned prior to lamination. The layer number and name can be seen on the rigid side. (e) and (f) A closer view of the conductors and sensors, showing how the contact pad is folded twice to expose the copper side to the next segment. (g) Top and bottom views of the laminated triangle segment, divided by the dashed line and flipped to see the bottom.

For this version of the trunk support device, we have selected three triangle elements and one four-bar linkage in the construction of our serial chain, as shown in Fig. 4.2(a). Details on dimensioning can be found in Sec. 4.4.5. Successive triangles are connected as shown in Fig. 4.2(a) and (e); the proximal joint of each link is located at a point along the triangle's base. The distal joint of each link is located

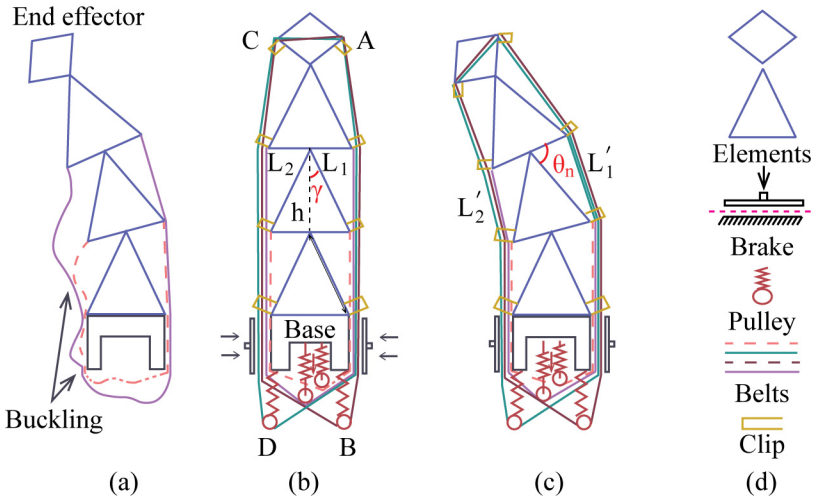

Figure 4.3. Design and integration of the brake. In (a), we demonstrate how buckling might happen. (b) is a 2D-sketch of the spine where the tension mechanism and clips are integrated to the base station to prevent buckling. We label the different components with various color and line types. In (c), we show how the required length for the layers changes as a function of configuration. Legend (d) represents the components and accessories of this system.

at the top vertex of the triangle; the next most distal triangle's origin (also located along its base) is thus connected to this point. The four-bar linkage is then connected to the top vertex of the most distal triangular link to compensate for any lengthening during trunk flexion. The selected laminate manufacturing technique allows for rapid and low-cost customization for users with different trunk lengths.

4.3.3 Brake Design

The mechanical design of the brake consists of three main parts: (1) flexible, sliding sheet-based belts attached to each moving segment of the wearable system, (2) a motorized clamp for applying normal forces to the belts, and (3) a tension mechanism that maintains tension in each belt to minimize backlash, as seen in Fig. 4.3(b).

In the triangular segments, one belt is attached to each side of the two lower

vertices of the triangular segment, as shown in Fig. 4.3(b). The lower portion of these belts is clamped to the base of the device via two motorized, self-aligning brake pads in the base station. These clamps are actuated via lead screws to stepper motors, which are controlled by a micro-controller [8] with a stepper motor driver [9]. When activated, the motors drive the lead screws to clamp the belts on each side of the base station, locking all the degrees of freedom together.

The length of the belt traveling around the base station and attaching to each segment is a function of system configuration, as seen in Fig. 4.3(c). For example, the total length of the layers on the side, $L_1 + L_2$, varies as $\sqrt{W^2/4 + L^2 - WL\cos(\theta_n)} + \sqrt{W^2/4 + L^2 - WL\cos(\pi - \gamma - \theta_n)}$ with a decrease of about 3.39 % in length at its limit compared to $\theta_n = 0°$. Excess slack in those configurations causes backlash in the system, which can lead to unintended shocks, misalignments and unintended stresses in the belt, and can ultimately lead to premature damage of the system, as shown in Fig. 4.3(a). To prevent buckling and keep the layers flat within the clamping area, we have added (1) a tension mechanism that utilizes a spring-loaded pulley to maintain tension at the bottom of the belt and (2) 3D-printed clips with clearance to allow layers to slide while maintaining a position constraint at each segment's vertices, as shown in Fig. 4.3(b).

Two belts are attached in a similar way to the two-DOF four-bar segment at each end, in order to fully lock the segment when needed. Fig. 4.4(c) highlights the internal routing within the segment, while Fig. 4.3 shows the external routing. The belt attached to point A passes down to the base along each triangular segment, around a spring-loaded pulley/tensioner, back up the other side, around a pulley on point C, and attaches back to point A. The green belt is routed in a similar fashion,

[8] Arduino UNO

[9] TB6600 stepper motor driver

but is attached to point C. The kinematics of this routing are detailed in the following section, Sec. 4.3.4.

According to previous literature, an empirical law for calculating resistive force, F_B, for one jamming layer that slides between the brake pads can be calculated as follows[49]:

$$F_B = \mu SNP \tag{4.1}$$

where μ is the friction coefficient between layers, S is the area of jamming, N stands for the total jammed layer number and P represents the negative pressure on the jammed materials. A detailed brake force evaluation can be found in the Sec. 4.4.2.

4.3.4 System Kinematics Workflow

We have developed two parametric models for understanding the kinematics of our locking serial mechanism. As mentioned in Sec. 4.3.3, one global brake is responsible to lock all DOFs; the force required to lock is thus a function of brake dimensions and system kinematics. To understand the dimensional requirements at different configurations, a full kinematic model is required to calculate the required brake force. Two kinematic models represent the two basic segments of our system, as shown in Fig. 4.2: triangular, single DOF segments, and a four-bar parallel mechanism that can both translate and rotate, located at the most distal segment. Together, these two models can help us understand how belts, routed through the system, can be expected to perform when held by the brake located in the base. This can be used for a number of purposes, including verifying the performance of our current system and estimating the kinds of performance-focused redesigns required to ensure that locking forces on all joints can support similar loading conditions by the wearer. Fig. 4.4 highlights the details of our belt routing and system kinematic variables; our process for solving for the belt forces is summarized below.

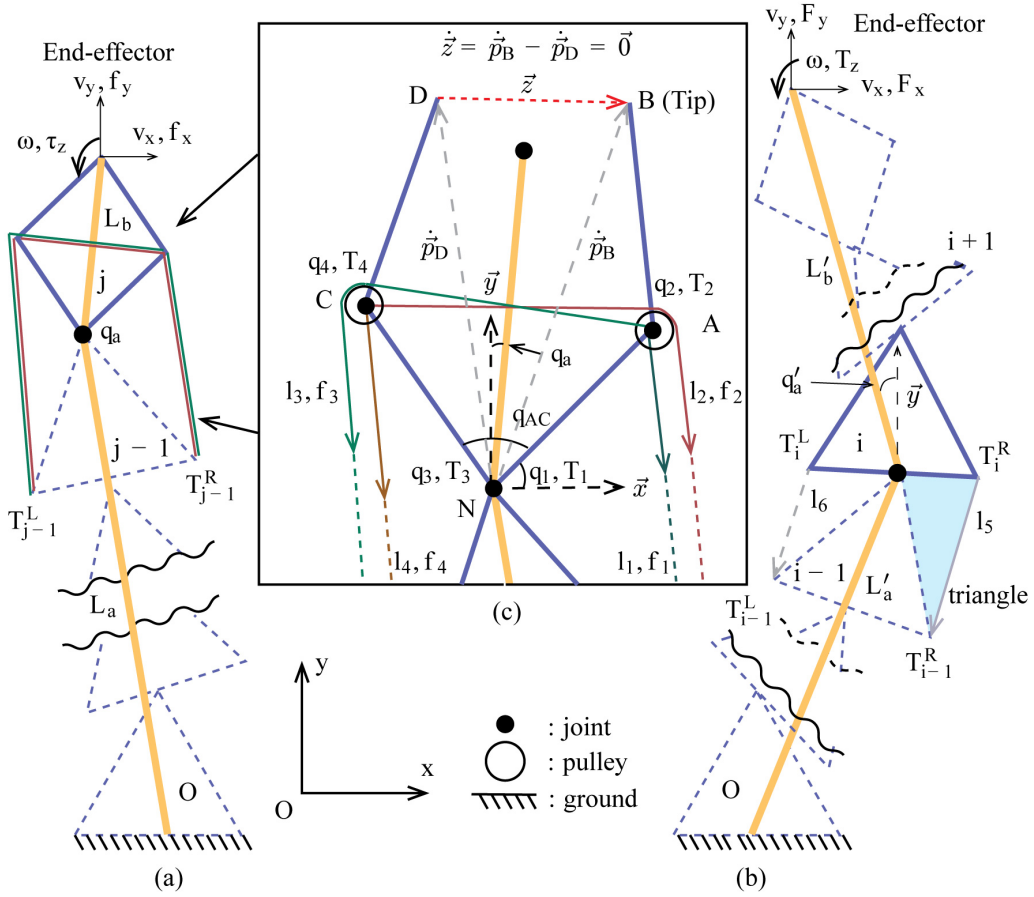

Figure 4.4. Kinematic Model: In (a), we show the simplified kinematic model of the j-th four-bar element mounted on *j-1*-th triangle, we also illustrate how belts are routed on the four-bar element and kinematics constraints in (c). Although the four-bar is a closed chain mechanism, we show these two RR chains split into chains NCD and NAB, constrained by $\dot{\vec{z}}$ (red line) We show how an example of how we relate a triangle at random location to the end-effector as shown in (b). Although we only have three triangles in our current design, we demonstrate how our method can be applied to one at a random location and orientation.

We first specify a system configuration, defining the joint orientations and thus the location of the end-effector. The dimensions of each link, and the belt routing determines the direction of all belt tensions, which can then be solved for based on an assumption of external loading conditions. Because belts span joints with varying geometry, it is readily apparent that the effective moment arm of the belt depends on

the state of the joint. A set of forces is then assigned to the end effector; these forces can be supplied either as a set of numerical or symbolic values, and can be derived from biomechanical loading assumptions based on different use-cases.

We proceed to analyze one link at a time, assuming that the selected segment is slipping, while all other joints remain fixed. This permits us to analyze the brake slip limits at each joint independently. Based on the direction of forces supplied at the end effector, only one of the two belts routed to each triangular segment will be in tension. We solve for the tensile force in each one degree-of-freedom joint required to maintain static equilibrium against external end-effector forces by formulating the problem as a constrained minimization problem, where the combination of forces must be minimized while keeping belt tensions positive.

4.3.5 Element Level Kinematics

For the final four-bar linkage, there are a total of four links and four belts, but only two total degrees of freedom, with only two belts ever in tension at a time, as shown in Fig.4.5.

Based on the fact that the four-bar linkage is a parallel mechanism, we can solve for the independent motion variables first, to generate the Jacobians mapping internal and external forces to each other, and then use those Jacobians to solve for the two out of four belt tensions that are holding the system in static equilibrium in that specific state. We again use a constrained minimization formulation to solve for belt tensions.

Given all the belt tensions solved for in the serial link kinematics, we then evaluate which of those tensions is the highest, and what the required braking force (normal to the belts) will be, using an experimentally-determined coefficient of friction. To symbolically solve the belt forces and the kinematics of each segments as well as

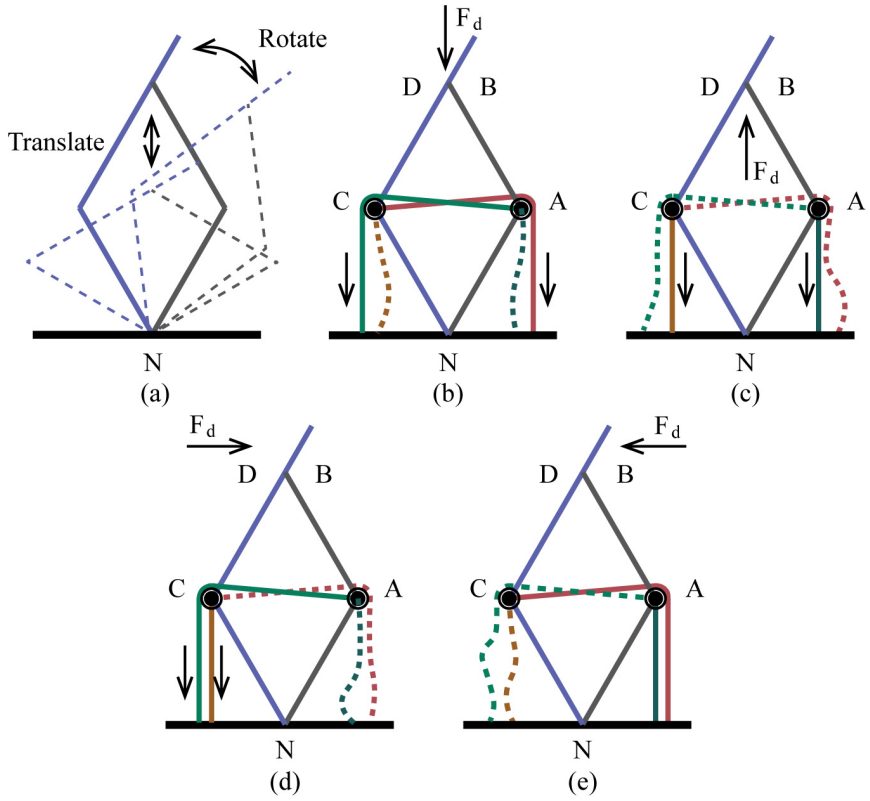

Figure 4.5. Locking illustration: In (a), we show the four-bar segment exhibits both translational and rotational DOFs, as seen in the three displayed configurations. In the following set of figures, we color-code four tendons to show the activated belts under various loading conditions. Solid lines indicate the tendons in tension; the arrows denote the direction of tendon forces. The dashed lines indicate slack tendons. F_d indicates the external loading direction. Sub-figures (b)-(e) illustrate four Cartesian loading conditions: downward, upward, right and left, respectively.

the full-body kinematics, we model the structure in Pynamics [10] [98, 58], a custom Python library using Kane's method to derive symbolic equations of motion. A master Python script reads the system's configuration and generates the state variables for each segments. We solve the required locking force for each triangle after calculating the four-bar locking forces using two sub-scripts respectively. The corresponding

[10] https://github.com/idealabasu/code_pynamics

scripts can be found in the repository [11] .

To understand the required forces for the segments, we first calculate the force required to lock the most distal segment under external loading, as a case study of understanding the full-body static force balances. This four-bar linkage, consists of a set of *independent* joints ($q_i = [q_1, q_3]$) and *dependent* joints ($q_d = [q_2, q_4]$), as shown in Fig. 4.4(a) and (c), such that

$$q = \begin{bmatrix} q_i \\ q_d \end{bmatrix} = \begin{bmatrix} q_1 & q_3 & | & q_2 & q_4 \end{bmatrix}^T . \tag{4.2}$$

The planar four-bar linkage can be thought of as two serial RR chains connected at their respective ends via a pin joint. The motion of $\vec{p}_B$ and $\vec{p}_D$, or the position of the two distal points on each serial chain are thus constrained together with the equation $\vec{z} = \vec{p}_B - \vec{p}_D = \vec{0}$. The time derivative of this vector equation with respect to the Newtonian reference frame permits us to linearize this equation with respect to the system's velocity variables $\dot{q}_i$ and $\dot{q}_d$, respectively.

$$\dot{\vec{z}} = \dot{\vec{p}}_B - \dot{\vec{p}}_D = \vec{0} \tag{4.3}$$

$$\dot{z} = \dot{\vec{z}} \cdot \begin{bmatrix} \hat{x} & \hat{y} \end{bmatrix}^T . \tag{4.4}$$

Using the relation

$$M_A = \left[\frac{\partial \dot{z}}{\partial \dot{q}_i} \right], M_B = \left[\frac{\partial \dot{z}}{\partial \dot{q}_d} \right] \tag{4.5}$$

we can then split z into independent and dependent parts $\dot{z} = M_A \dot{q}_i + M_B \dot{q}_d = 0$ and solve for $\dot{q}_d$

$$\dot{q}_d = \underbrace{[-M_B^{-1} M_A]}_{C} \dot{q}_i \tag{4.6}$$

[11] https://github.com/dli-sys/code_TMech_pynamics_demo

The Cartesian velocity of the end-effector can be expressed by the well known equation $\dot{x} = J\dot{q}_i$, where $\dot{x} = \begin{bmatrix} \dot{\vec{p}}_B \cdot \hat{x} & \dot{\vec{p}}_D \cdot \hat{y} & \omega \end{bmatrix}^T$. J is derived by expressing

$$\dot{x} = J_i\dot{q}_i + J_d\dot{q}_d \tag{4.7}$$

where $J_i = \left[\frac{\partial \dot{x}}{\partial \dot{q}_i}\right]$ and $J_d = \left[\frac{\partial \dot{x}}{\partial \dot{q}_d}\right]$. By substituting in (4.6) and collecting terms,

$$\begin{aligned} \dot{x} &= (J_i\dot{q}_i + J_dC\dot{q}_i) \\ &= \underbrace{(J_i + J_dC)}_{J}\dot{q}_i \end{aligned} \tag{4.8}$$

The flat belts used for locking the four-bar segment are routed as illustrated in Fig. 4.4(c), where belt l_1 is connected to point pA and then routed along the proximal triangle elements through point T^R_{j-1}, continuing to the base where it is connected to belt l_3. Belt l_2 is attached at point pCD and routed around a virtual pulley co-located at pAB and finally routed down along right side of each triangle down to the base, connecting at the bottom to belt l_4. On the left side, l_3 and l_4 are routed along the left side of the system in the same way, connecting to l_1 and l_2, respectively. When clamped, however, the two sides of each belt must be considered independent, and their forces analyzed separately. The velocity $\dot{l}$ of these four belts can be expressed as

$$\dot{l} = [\dot{l}_1 \ \dot{l}_2 \ \dot{l}_3 \ \dot{l}_4]^T = J_t\dot{q}_i, \tag{4.9}$$

where

$$J_t = \left[\frac{\partial \dot{l}}{\partial \dot{q}_i}\right] \tag{4.10}$$

We can thus equate the torques on our independent degrees of freedom q_i from the belts to the equal and opposite torque from the end-effector to the same joints. The required end-effector force $f = [f_x \ f_y \ \tau_z]^T$ can be then calculated according to the tension in the belts $f_t = [f_1 \ f_2 \ f_3 \ f_4]^T$ using the principle of virtual work to

obtain

$$\tau_{ind} = J^T f = J_t^T f_t$$
$$J^T f - J_t f_t = 0 \tag{4.11}$$

Since the J_t is a 4×2 matrix, it is clear that the four forces from the brakes act redundantly on the system. Because, however, they can only act in tension, a valid solution for obtaining static equilibrium must ignore cases when tension in the belts is negative. To solve this problem we formulate it as a constrained minimization problem, minimizing the sum of the square of the belt tensions at a given external tip force, while in a specific configuration as:

$$min \quad - f_{t(i)}^T f_{t(i)} \tag{4.12}$$

subject to

$$g(f_t) : J^T f - J_t f_t = 0 \tag{4.13}$$

$$h(f_t) : f_t \geq 0 \tag{4.14}$$

We calculate the $f_{min}(q)$ at different configurations of the four-bar as a function of q. The resulting minimum force solution can be then used to determine the locking force requirements for the four-bar on the top.

We also model the force interactions of the i-th triangular segment at an arbitrary location as shown in Fig. 4.4(b). The distal hinge of this triangle is connected to the base of the distal four-bar segment. The belts on the triangle are connected to the corresponding vertices of the successive triangle and shown in Fig. 4.4(b) as l_5, l_6. As the triangles are connected to the successive element on its top vertices and the motion of four-bar element will not affect the triangles, we simplify the kinematics to serial linkages.

For example, to solve for equilibrium in the k-th triangle, we create a virtual link, L_a connected to the bottom of this triangle, rotated around the origin. The remainder of this system can be then simplified to a virtual link, L_b rotated along the first link. The length and angular velocities (L_a, L_b, q_a) of the system can then be calculated according to the configuration of the device.

The Cartesian velocity of the end-effector ($\dot{x} = \dot{\vec{p}}_B \cdot \begin{bmatrix} \hat{x} & \hat{y} \end{bmatrix}^T$) can be expressed as

$$\dot{x} = J\dot{q}_i \tag{4.15}$$

where $J = [\frac{\partial \dot{x}}{\partial \dot{q}_i}]$. The velocities $\dot{l}_t$ of the layers mounted on the triangles can be expressed as

$$\dot{l}_t = \begin{bmatrix} \dot{l_5}, \dot{l_6} \end{bmatrix}^T = J_i q_i \tag{4.16}$$

$$J_t = \begin{bmatrix} \frac{\partial \dot{l}_t}{\partial \dot{q}_i} \end{bmatrix} \tag{4.17}$$

The triangle belt velocities can be then related to the independent end-effector velocities. The minimal layer forces, $f_t = [f_5, f_6]^T$ under external load, f can be calculated using a similar approach described in Eq. (4.11) to (4.14) and formulated as

$$min \quad -(f_5^2 + f_6^2) \tag{4.18}$$

subject to

$$g(f_t) : J^T f - J_t f_t = 0 \tag{4.19}$$

$$h(f_t) : f_t \geq 0 \tag{4.20}$$

We obtain the minimal layer force for the triangles. By modifying the orientation of the triangle and the corresponding belts, we then are able to solve each triangles at an arbitrary location.

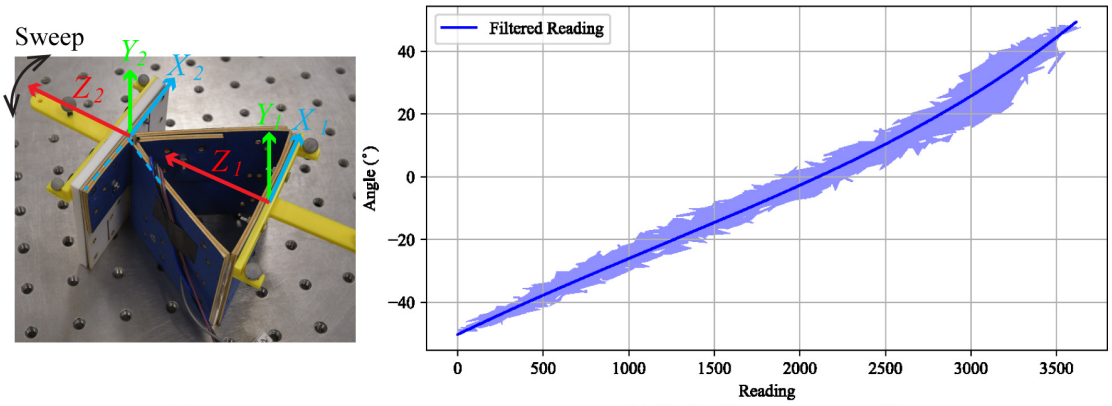

(a) (b) Hall effect sensor reading

Figure 4.6. Sensor calibration and sensing result. In (a), tracking markers permit the relative rotation between two rigid bodies to be measured using a OptiTrack motion capture system. During the experiments, the second rigid body is swept along its $\hat{y}_2$ axis. (b) The fitted curve.

4.4 Results and Analysis

4.4.1 Angle Sensing using Embedded Sensors

With hall effect sensors integrated in each joint, the performance these sensors may be evaluated by measuring the change in magnetic field under cyclic joint motion at various speeds, using the test setup shown in Fig. 4.6(a). Three OptiTrack markers are attached on each segment to define the $\hat{x}$-$\hat{z}$ plane normal to the rotation axis $+\hat{y}$ and permit the relative angle of each joint be measured, in order to calibrate the sensors. The angle between two segments, θ_c, can be expressed as $\theta_c = \cos^{-1}(\hat{z}_1 \cdot \hat{z}_2)$.

Once the OptiTrack data and hall effect sensor data are collected and synchronized, we perform a exponential curve fitting to obtain mathematical model of the sensor to estimate the joint angle using hall effect sensor. The root-mean-square deviation (RMSE) calculation to evaluate the hall effect sensor estimation against OptiTrack orientation demonstrates a 4.07° error and the result can be seen in Fig. 4.6(b).

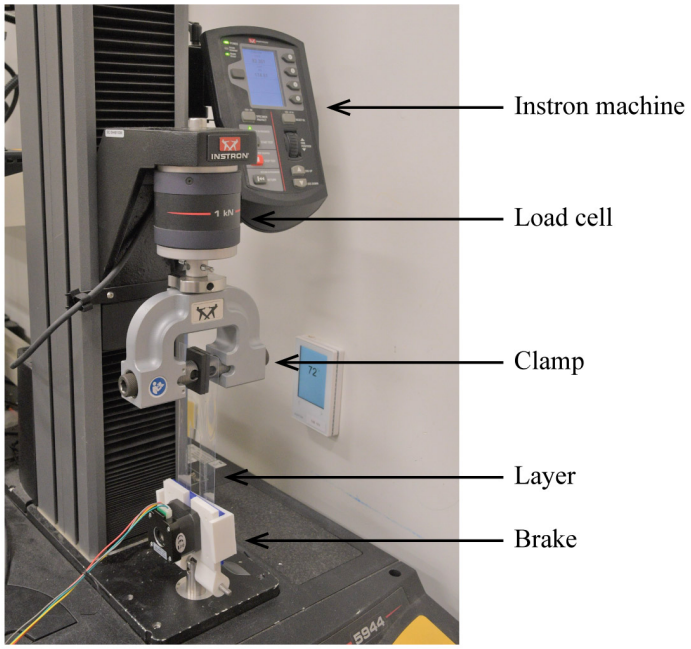

Figure 4.7. Measuring tensile forces with the Instron

4.4.2 Brake Performance

To measure the force generated by the brake, we use a tensile machine [12] with 1 kN load cell at 1 kHz sampling rate as shown in Fig. 4.7. The machine's fixture is clamped to the end of the layer. To facilitate the test, a one-sided clamping mechanism was fabricated with a end cap that can be easily attached to the Instron machine by plugging a metal locating pin. All other design parameters, dimensions, and materials remain consistent with the belts integrated into the base station. Once attached to the Instron, the brake's stepper motor activates, clamping the belts against their housing and the Instron subsequently begins a measurement cycle. The friction force per mm^2 between the brake pad and belt was measured in this way to be $0.017 N/m$ and using the stepper motor at 12 V, 1.7A can generate 0.029 N/mm^2 resistive force per square millimeter.

[12] Instron 5944 machine

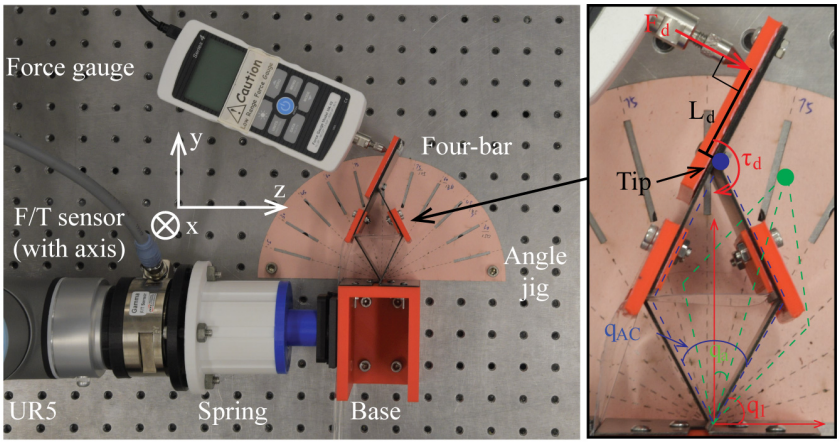

Figure 4.8. Four-bar element locking test set-up. In (a), we show the overview of the experiments and label each piece of equipment. The spring is mounted within the white case between the F/T sensor and the base. The alignment jig (in pink) is installed under the four-bar segment. We highlight how forces are applied to the distal link in (b) and label how we define the joint angles, inner angle and orientation, consistent with q_1, q_{AC} and q_a in Fig. 4.4.

4.4.3 Four-bar Element Kinematic Model Verification

We perform a series of tests measuring the external load required to deform the linkage while changing the configuration and locking forces to verify the static force model presented in Sec. 4.3.4. We use a UR5 robot arm with a spring and a load cell attached at its end effector to adjust the locking pressure, as shown in Fig. 4.8(a). According to Hooke's law, compressing the spring installed inside the white case between the brake pad and the base station increases the locking force. We record the z-axis force of the load cell and control the robot's displacement simultaneously using a python script. The robot arm stops once the force threshold is reached in order to maintain constant clamping pressure.

In this set of tests, the length of each link in this four-bar is 30 mm. After adjusting the four-bar mechanism's joint angles and orientation, we lock the four-bar

using the test setup by compressing the locking pad to constrain the motion of the belts. For the purposes of validating the kinematics and to ensure that the stiffness of the flexure joints do not add noticeable stiffness to the system, we have selected a thinner flexible material [13] for the hinge layer of the laminated origami structure. To measure the external loads applied to the tip, we use a force gauge [14] to push distal link of the four-bar normal to the surface until the layer slips at each configuration, where the distance to the tip of the four-bar, L_d is 30 mm. During the test, we record the maximum force required to initiate slip in the belts and then from that value calculate the equivalent holding torque. In each combination of joint angle and orientation, we repeat the test ten times to obtain the average external torque to deform the mechanism, $\bar{T_d}^f$ as $\bar{T_d}^f = \bar{F_d}^f L_d$.

We have tested the device under a series of symmetric configurations about the four joint angles, q_1=[30°, 45°, 60°, 75°]^T and four values for the inner joint angle q_{AC} = [30°, 60°, 90°, 120°]^T, as shown in Fig.4.9.

We use a laser-cut alignment jig to align the links according to each configuration. As the tip torque is manually measured and applied, using smaller clamping forces improves the accuracy of our results by reducing the deformation that would be present in the system under higher loads. We thus apply 2N of force along the force/torque sensor's z-axis to clamp the belts in this experiment.

We then changed the orientation q_a of the segment to create asymmetric scenarios and validate our kinematics across a larger workspace. In this set of experiments, the orientation, q_a was set to [-30°,-15°,0°,15°,30°]^T of the inner angle we measured before. When the inner angle is 120° and the orientation is set to -30° or 30°, the lower link of the four-bar mechanism interferes with the base. We thus skip this two

[13] Grafix Dura-Lar 2 mil

[14] Mark-10 M4-10 Force Gauge

sets of experiments. A total of 18 (4 × 5-2) of sub-tests were thus performed in Fig.4.9.

The average measured friction force, f_r, measured using the test setup is 1.56N. We then use the following Jacobian matrix, J_t in its numerical form obtained from the Pynamics code generated using the method described in Sec. 4.3.4 to relate the belt forces, $[f_1, f_2, f_3, f_4]^T$ to the independent torque, $[T_1, T_2]^T$ of the four-bar.

$$\underbrace{\begin{bmatrix} c_1 & c_2 & c_3 & c_4 \\ c_5 & c_6 & c_7 & c_8 \end{bmatrix}}_{J_t} \begin{bmatrix} f_1 \\ f_2 \\ f_3 \\ f_4 \end{bmatrix} = \begin{bmatrix} T_1 \\ T_2 \end{bmatrix} \tag{4.21}$$

During the test, the external torque is applied to link $p\vec{D}B$ and the left side link, the right side of the four-bar and the belts are thus in a slack state, meaning no belt force is applied. We thus simplify equation (4.21) to

$$\begin{bmatrix} c_2 & c_3 \\ c_6 & c_7 \end{bmatrix} \begin{bmatrix} f_2 \\ f_3 \end{bmatrix} = \begin{bmatrix} T_1 \\ T_2 \end{bmatrix} \tag{4.22}$$

The tip torque τ_{tip} can be calculated as $\tau_{tip} = T_1 + T_2$. We use the following optimization routine to calculate the maximum external torque the four-bar linkage can hold:

$$\begin{aligned} min: \quad & -(T_1 + T_2)^2 \\ & -(c_2 f_2 + c_3 f_3 + c_5 f_2 + c_6 f_3)^2 \end{aligned} \tag{4.23}$$

subject to

$$h(f_2, f_3): \begin{bmatrix} 0 \\ 0 \end{bmatrix} \leq \begin{bmatrix} f_2 \\ f_3 \end{bmatrix} \leq \begin{bmatrix} f_r \\ f_r \end{bmatrix} \tag{4.24}$$

We then obtain the maximum holding torque the four-bar is able to provide and compare with the $\bar{T_d}$ values experimentally measured, as shown in Fig. 4.9.

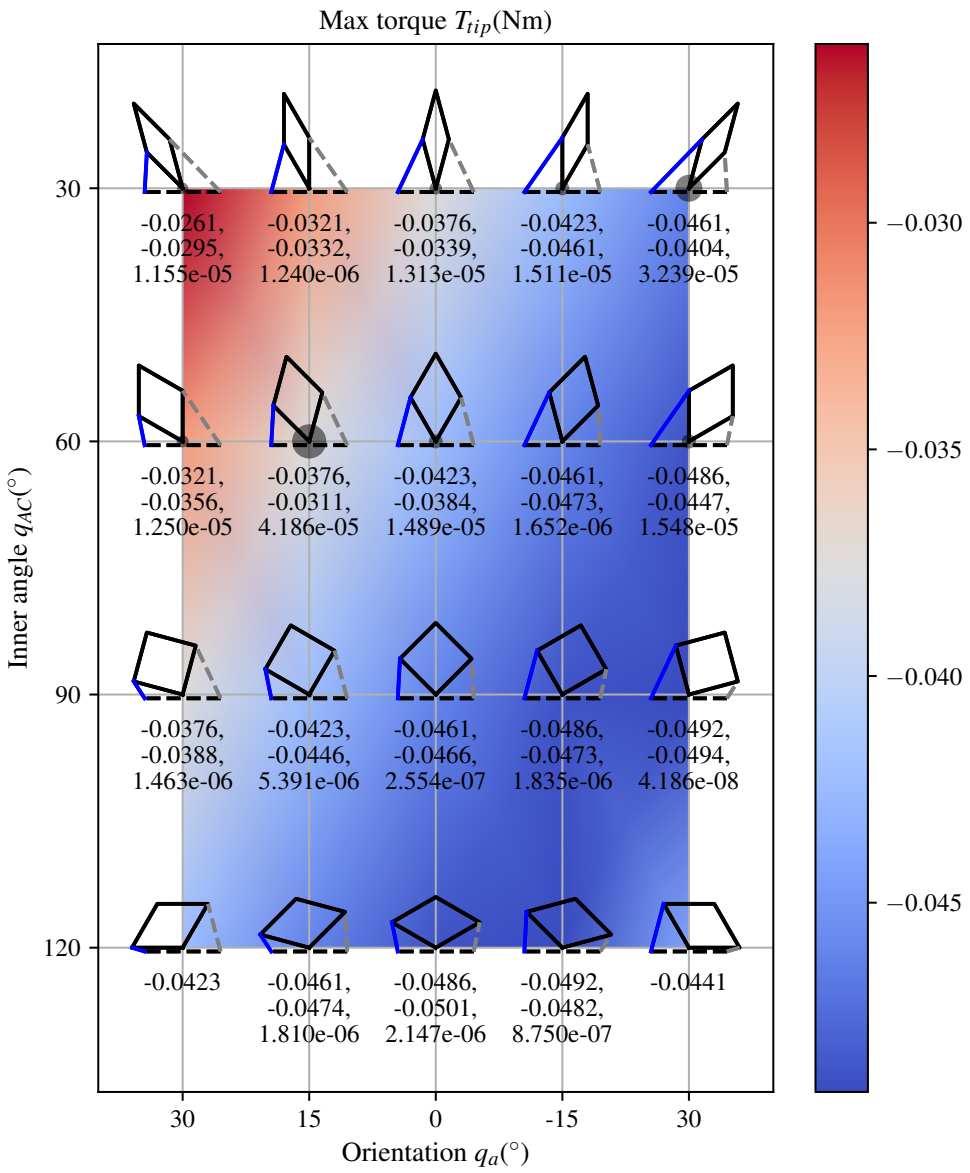

Figure 4.9. Four-bar kinematic model validation. In this figure, we show the maximum simulated holding torque of the four-bar using the continuous contour plot. Experimental values, located at each grid element under the black dots show the simulated torque, measured average torque from experiments, and RMSE between these two values respectively. The size of the black dot indicates the RMSE. We plot the current configuration of the four-bar with base and belt at each combination of orientation and inner joint angle. As the experiments for (30°, 120°) and (-30°, 120°) are not performed, we show the configuration and simulated value only.

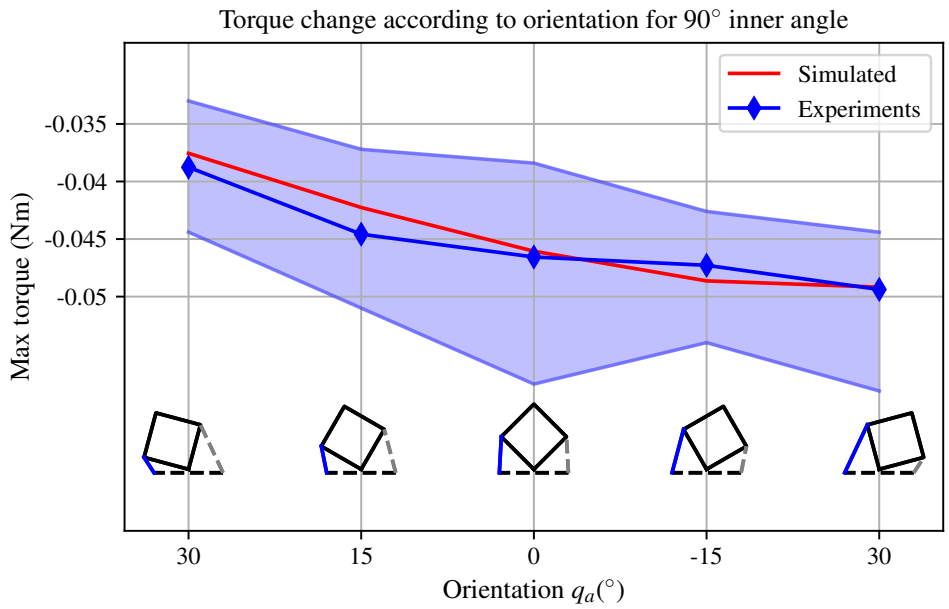

Figure 4.10. 90° inner angle four-bar torque vs. orientation. In this figure, we highlight how the four-bar holding torque changes according to the orientation of the linkage in Fig. 4.9 at 90° inner angle. The blue solid line indicates the experimental values and the blue region beneath it shows the range of experimental values measured from the tests, while the red solid line shows the model estimate.

Although these mechanisms are implemented in the full prototype, some configurations including the belt routing and base location are different. We thus developed two separate simulations to mirror the experimental setups. These may be found in the code repository, where a detailed description of the approach can be found.

4.4.4 Triangle Element Kinematic Model Verification

Using a similar approach, we validated the kinematics of the triangle element, where the length of the sides is 85mm. We use the same test setup previously introduced in this section, but replace the base to fit the new triangular element, as seen in Fig. 4.11. We use the force gauge to push the tip of the upper triangle element, T_2 across joint angle, q_b = [-30°,-15°,0°,15°,30°] and average the reading to obtain the

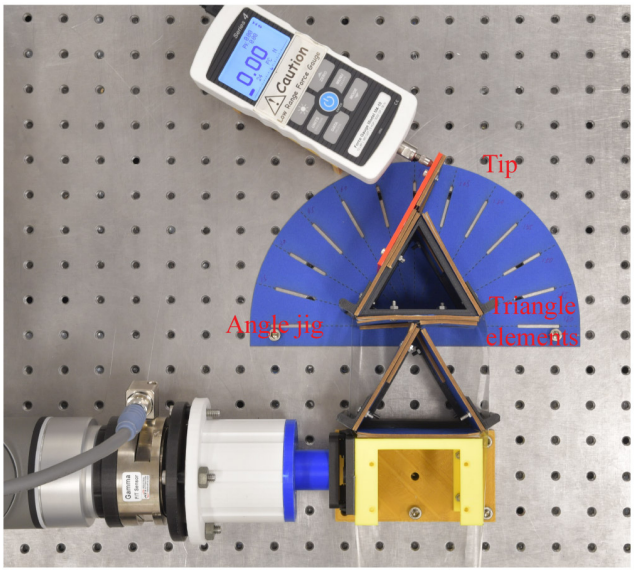

Figure 4.11. Triangle element kinematics test setup: In this figure, we present the test set-up for validating triangle element kinematics and show the result. We replace the four-bar linkage with the triangle segments, base and the angle measurement. The test is performed in a similar manner as described for validating the four-bar.

torque required to deform the triangle as $\bar{T}_d^t$ seen in Fig. 4.12.

In Fig. 4.12, the blue line indicates the condition where the left belt is locked and an external torque is applied clockwise, illustrated along the top of Fig. 4.11. The blue transparent area indicates experimental error between runs, while the blue solid line indicates the mean of experimental data; the dashed blue line represents model results. As pushing along the right side yields a mirrored result, we mirror the model results, presented as a red dashed line.

As mentioned in Fig. 4.4(b), the belt routed between links forms a triangle; this means that the moment arm of each belt is a function of the each joint's configuration. This influences the locking forces available at each joint, requiring us to calculate the braking force required as a function of system configuration. To help dimension of the device, we must analyze the *worst-case* scenario.

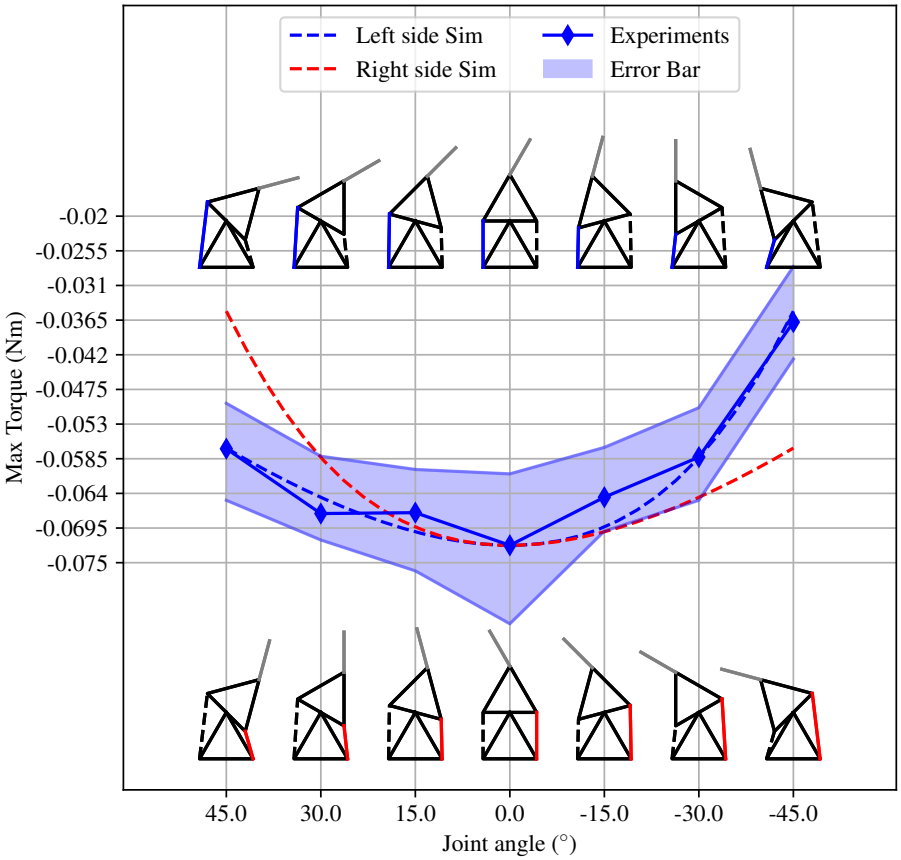

Figure 4.12. Triangle element kinematics torque change vs. configuration: We compare the estimate for the maximum torque the triangle can hold across different configurations against the experimental data, where the solid line is the mean experimental value, the dashed lines indicate the model estimate, and blue region shows the range of experimental values collected at each point.

4.4.5 Dimension Selection and Full System Kinematics

We select the following dimensions for the mechanism, as illustrated in Fig. 4.13 and listed in Table 4.2. We use two NEMA 17 stepper motors (42 mm × 42 mm × 34 mm) inside the base; the width of both the triangle and base are 85 mm. In the current design, we use three equilateral triangles (73 mm height) and one four-bar linkage with a joint length of 40 mm on the top. Using the kinematic models developed in Sec.4.3.4 and the torque requirements from the human study [70], we have determined

the braking forces required for locking the robot are at least 60N when the device is straight. Using Eq.(4.1), with a static friction coefficient of 0.017, we calculate that the minimum required area for the brake pad is 5200 mm^2. Considering the screw hole in the middle of the brake pad (r = 5.25 mm), the length of the brake (L_b) is set as 5200 /(80-5.25 $\times$ 2) =74.8; we thus use a 75 mm long brake pad.

The kinematic analysis also confirms that the four-bar linkage is the weakest joint in this system. We attribute that to the fact that the total effective width of the belts connected to the four-bar segment is half of those connected to the triangular segments, in order to accommodate the routing of four separate belts into the 2-DOF segment.

To test the system-level stiffness, we fully assemble the spine device, mount the device to the test bed horizontally, and attach the brake system as shown in Fig. 4.13(a). During the test, a Python script locks the belts when the device is straight and commands the UR5 to push the end-effector with a metal probe. The robot arm then returns to its original position after it pushes the probe forward a set distance. We then compare the z-axis direction load cell force for four distances, 10 mm, 30 mm, 50 mm and 70 mm to understand the stiffness of the system. We then start to push the robot in locking state using the force gauge to understand the slippage limit using a similar setup in Fig.4.8. We repeat the test for ten times and the average force required to deform the robot is 56.5 N. We attribute this deviation to the design goal (60N) to the assembling and misalignment error of the system. In these test we found that the first joint to slip was the four-bar, confirming the kinematic model's braking force estimates.

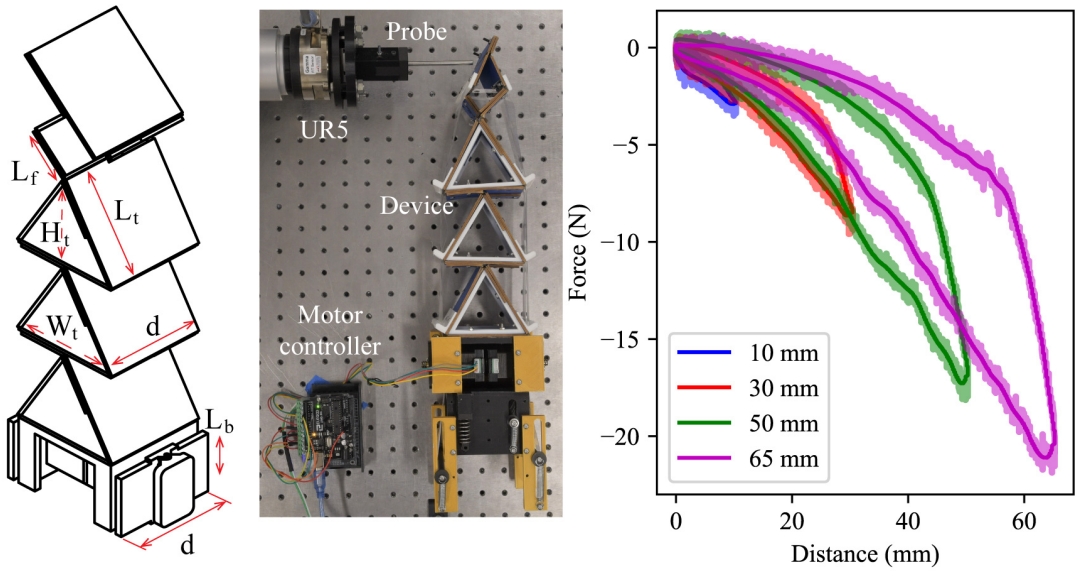

(a) Sketch (b) Test setup (c) Force vs. distance (stiffness)

Figure 4.13. System dimension and loading capability experiments. In (a), we show a sketch of the robot with labeled dimensions. (b) illustrates the test setup. In (c), we show the filtered load cell force versus distance using the solid lines. The light colored lines indicate the unfiltered raw data. We notice the deviation between 40 mm data' slope and we attribute this to the complex kinematics and initial states of the device.

4.4.6 System-level lock and unlock

In this section, we use the same test setup in Fig. 4.13(a) and start pushing the device in the unlocked state using low motor current to measure the locking speed of the robot to prevent damage to the load cell. As the robot is a passive device that can be stiffened on demand, locking speed became the most important – and only – metric for system response. After the tip of the UR5 passes the straight, vertical configuration of the device, the device is locked as the UR5 continues moving.

We use the force from the load cell to differentiate between locked and unlocked states. Before the test starts, the probe does not contact the device for calibration purposes; when the probe begins to contact the spine mechanism, a small -z direction

Parameter	Value	Description
L_f	40 mm	Four-bar length
L_t	85 mm	Triangle length
H_t	73 mm	Triangle height
W_t	85 mm	Triangle width
L_b	75 mm	Brake length
d	80 mm	Depth

Table 4.2: **Spine robot parameter**

force can be seen (starting around t=5 s) − due to system joint stiffness and belt friction − in Fig. 4.14. The load cell force increases after the lock activates (as shown in the red solid line). We compare the load cell reading against the unlocked system (in blue) and estimate that the brake's locking time is around 0.1s, which is a sufficient response time for supporting the trunk, according to preliminary human subject studies.

4.5 Conclusion and future work

We have presented a origami-inspired mechanism with embedded sensing capabilities as well as extensibility for connecting external sensors. We mechanically clamp the sliding layers to design a laminar jamming inspired brake. We estimate the joint angle and end pose using the integrated sensor and reveal its potential in wearable robotics.

We believe that origami inspired "exo-shell" structures can bridge the gap between rigid exoskeletons and soft exo-suits in a way that balances the compromises of both. Introducing origami-inspired techniques into wearable robotics permits us to provide lightweight, low-cost and rapidly manufacturable solutions for each user. Our selected manufacturing technique facilitates rapid iteration of designs while produc-

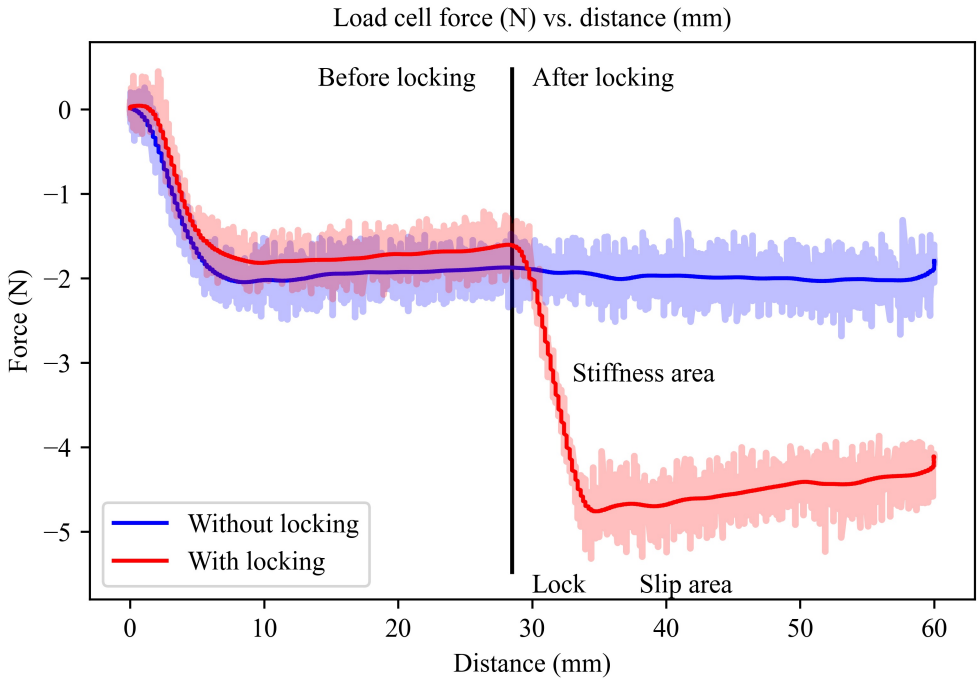

Figure 4.14. System level locking test. We compare the load cell force with and without locking (0.5A current) using red and blue solid lines correspondingly, where the transparent error bar indicates the raw data. We activate the brake at around 28 mm where we draw a black vertical line to indicate the locking.

ing highly-capable wearable prototypes. Currently, this device is designed on to be mounted on the human back to provide external support. By modifying the arrangement and dimension of structural elements, brakes, and supporting components, this development strategy can be easily adapted for wearable applications about other parts of the human body.

Future work includes optimizing the overall dimensions based on a biomechanics study planned with our collaborators on healthy elderly human subjects. Our aim will be to evaluate the hypothesis that timed stiffening of the system can improve stability and reduce torques about the trunk during obstacle avoidance.

Currently, this device is mounted at the spine of the subject. However, we find

that the kinematics of larger arrays of this specific tessellated pattern exhibits highly constrained motion, making it less compatible with the types of motion experienced around the human torso. We aim to address this by investigating more complex, stiffenable, 2D origami patterns such as the waterbomb and herringbone patterns.

Another improvement will be to modularize the braking system to eliminate the base-mounted spring tensioner and reduce the system-level design complexity, which is addressed in Chapter 5.

Chapter 5

A COMPACT, LIGHTWEIGHT, FAST-RESPONDING AND HIGH TORQUE MECHANICAL LOCKABLE MODULE FOR MODULAR WEARABLE ROBOT

5.1 Introduction

In this chapter, I introduce a "lockable module" for controlling rotary degrees of freedom (DoFs) for wearable robotics. As an improvement to Chapter. 4, we are aiming for a compact, lightweight and rotary module that can be individually locked and unlocked. Based on cam-based self-locking mechanisms, we introduce a single-sided brake, where we implement design improvements to realize rapid switching between locked and unlocked states. We then integrate the brake into the module and a series of design considerations to keep the system lightweight with low-energy consumption. Our robot module is capable of resisting up to 11.98Nm torque when locked while only adding 0.7Nm in frictional forces in its unlocked state, and is able to respond under payload of more than 10 Nm in less than 0.15s in order to both lock and unlock. These performance metrics are enhanced by multiple design elements and features, including joint limits to regulate output force, a pulley design to reduce friction, and a linear tensioner to flatten the belt. Our selected braking solution is contrasted against common locking solutions in robotics; we conclude with thoughts on how the module can be adapted to our existing wearable robot system and other potential applications in robotics.

5.2 Statement of Designs and Experimental Methods

This chapter provides the following examples and technical contributions for robotics study:

1): A showcase of an effective brake and brake mechanism design: This chapter presents a thorough mechanical brake design workflow. Drawing inspiration from a simple self-locking mechanism, I identify the minimum design considerations for it to serve within a larger mechanical/robotic system, then implement these features, accompanied by extensive experiments. Through these adaptations, the brake module is able to balance several critical but conflicting design requirements - high torque, fast response time while still remaining compact, lightweight, and low power. The design complexities, retained within the locking robot, do not introduce additional system-level costs when implemented in other robotics applications, thus maintaining affordability for integration.(Page: 78);

2): A comprehensive experimental template for evaluating robot performance: This chapter involves conducting a series of experiments, including tensile testing for the mechanism and robot using an Instron tensile machine to measure force and torque; measuring range of motion using an external angle encoder, as well as gauging response speed using the Instron machine and encoder. By adjusting equipment selection for different experiments, one can use this template to evaluate common performance metrics in robotic studies. . . . . (Page: 94);

3): Conceptual design of "Modular Wearable Robot": In Sec. 5.6.2, following a similar approach in Chapter. 4, the concept of "Modular Wearable Robot"

was introduced. By leveraging a modular design concept, this robot reduced the cost of integration, customization, and human experiments for non-experts. This approach also provide examples of designing effective robot module for a particular functionality and can be applied to other types of actuator/ end-effector module. (Page: 97).

5.3 Design requirements and motivation

In Chapter 4, an origami-inspired wearable robot was presented, based on the requirements for an untethered, low-load-carriage, fast-response, high-force density device that can be worn throughout the day [59]. This robot, featuring serially-connected triangular rotary modules with a global lock at the bottom, was able to lock all degrees of freedom (DOFs) at once. Although controlling all segments with a single brake decreases the segment-level design complexity, accommodating the locking systems engaging in order to provide a continuous normal force, increasing complexity at the system level, limiting the addition of new segments or new types of locking modules.

In response to these challenges, I updated our design goals as follows: 1) Compact and lightweight; 2) High force/torque output and low resistance when unlocked; 3) Fast response in both locking and unlocking; 4) Infinite locking position within the range of motion; 5) Low power consumption. Our objective, therefore, is to develop a single brake module that satisfies these updated requirements while minimizing the system-level design and integration complexity.

As mentioned in Chapter 2, the use of mechanical devices can also result in a failure to unlock in loaded conditions, due to the friction or geometry between interfacing parts [86]. This issue can lead to 1) significant energy consumption during state

change or 2) a requirement for an additional actuator for unlocking, thereby increasing system weight and energy consumption. To address this concern, we implemented joint limits in our design, to restrict the maximum distance or angle between the locking components and the base and control whether or how much our device operates in the "self-locking" regime.

Thus, in this chapter, we present a lockable module that controls the rotational degree of freedom (DoF). We adopt a cam profile in conjunction with a frictional locking strategies in a spring-loaded, "near" self-locking mechanism. To avoid some of the drawbacks we mentioned in Chapter. 2, our approaches include implementing physical joint limits to avoid entering singular conditions and material or structural failure. We have equipped the module with a motor to permit active reconfiguration of the brake and to increase the response speed in both locking and unlocking directions.

Thus, we list our contributions of this paper as follows:

1): We present a fully-integrated lightweight (<265 g) and high-torque (>10 Nm) lockable module that requires low-voltage power;

2): We show an example of how "near" self-locking mechanisms can be coupled with other design considerations to reduce power consumption;

3): We implement active-reconfiguration on a passive device, achieving a fast response (<150 ms) using low-energy actuation (<0.15 J).

The rest of the chapter is organized as follows: In Sec. 5.4.1, we introduce the design inspiration for the single brake, then integrate the brake into the module in Sec. 5.4.2. We detail the belt routing system and locking sequence in the rest of Sec. 5.4. In Sec. 5.5, we first measure the single brake-level performance metric, followed by a series of module-level experiments focusing on holding torque, locking and unlocking response, as well as the ability to unlock under payload. We compare

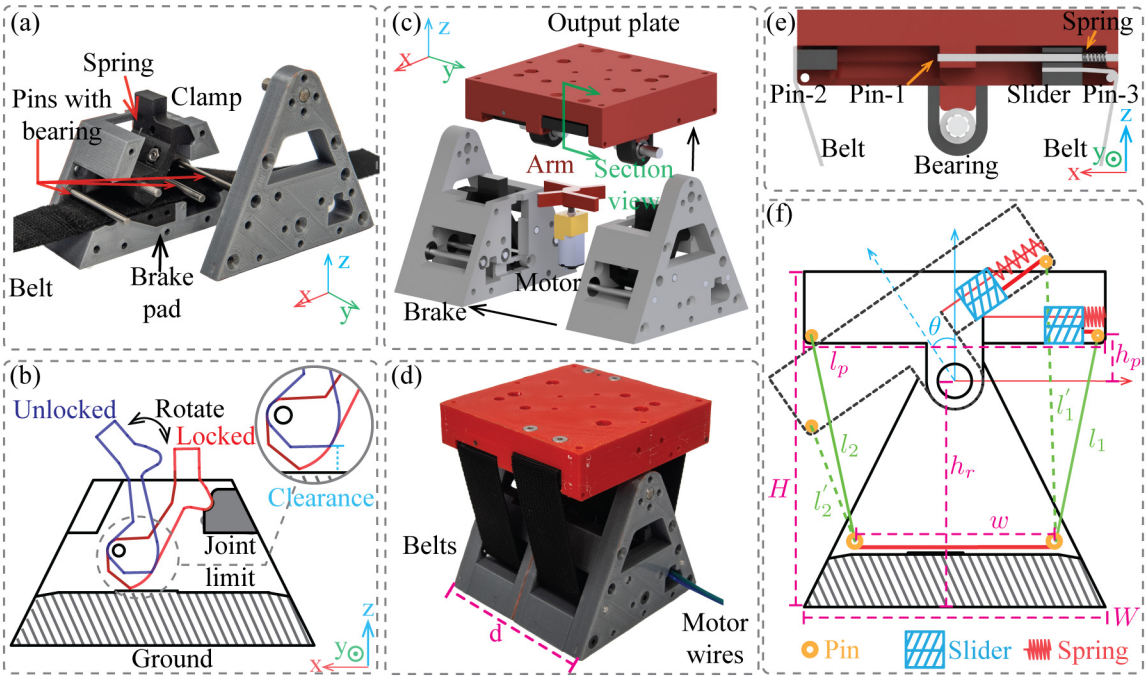

Figure 5.1. Lockable module design: Sub-figure (a) illustrates the brake design and (b) is a simplified 2D sketch. We highlighted the effect of joint limit and the locking and unlocking state, using red and blue, repetitively. We have also indicated the change of clearance in z-direction between the clamp and the brake pad. We present the exploded view of the lockable module in (c), where the motor is installed in the middle of two brakes and the local coordinate system is labeled on the upper right corner. (b) is the assembled device. In (e), we first show a cross section view of the output plate in xz-plane, indicated by the green arrows in (b). The spring in the linear slider is located between the belt and the plate and not visible from the outside. Pin-1 is used for the linear sliding while pin 2 and 3 serve as virtual pulleys. Finally, we compare the location of the slider according to the joint angle and label the dimension of the module in (f).

the features and merits against our design goal in Sec. 5.6.1, where we also list the features of the locking devices mentioned in the Introduction. This paper concludes in Sec. 5.7 with potential improvements.

5.4 Materials and Methods

5.4.1 Single brake design and cam-profile

The cam-profile brake design, as presented in Fig. 5.1(a), includes three main components: a spring-loaded clamp, a brake pad fixed to the base, and a belt linked to the output. When the belt is pulled along the $+x$ direction, a higher resistive force occurs due to the reduced clearance between the clamp and brake pad, illustrated in (d). To increase friction, the brake pad area is covered by sandpaper (150 CW). A rotary spring creates initial tension, keeping the system in a locked state.

As shown in Fig. 5.1(b), when the clamp rotates counter-clockwise, the brake unlocks since the clearance between the pad and clamp is larger than the thickness of the belt. The tension in the spring increases with the counter-clockwise rotation of the clamp; either a constant force or joint limit is required to maintain the unlocked position. This problem is addressed by the lockable module and is discussed further in Sec. 5.4.2.

As mentioned in the introduction, in a configuration where the system in a self-locking state, if the belt continues to be pulled, it can cause excessive compression between the clamp, belt, and base. This may lead to a structural failure and increase the force required to unlock the brake. To avoid this, we added a joint limit on the proximal (-y direction) end of the clamp to constrain its maximum angle in the xz-plane, as highlighted in Fig. 5.1(b). By fixing the maximum angle for the clamp and adjusting the height of the brake pad, we can control the clearance between the clamp, pad, and belt. This strategy allows us to manage the locking regime (whether self-locked or near self-locked), maximum resistive force, and the required unlocking force.

We measured these force metrics for the brakes in Sec. 5.5.1, and chose an exper-

imental approach to guide our design decisions. Although optimizing the cam-profile geometry [23] and surface treatment are alternative methods for adjusting the output force, the main goal of this paper is to incorporate this self-locking inspired mechanism into a fully functional locking device, taking into account system-level design considerations. Therefore, we don't dive into details about the locking geometry, focusing instead on analyzing the effect of height of the brake pad.

5.4.2 Rotational lockable segment design

To control a full rotational degree of freedom (DoF) with the lockable module, we integrated two brakes into one lockable segment. This design can be seen in Fig. 5.1(c). Since the single brake controls linear sliding only in one direction, to control a full DoF, we arranged two brake submodules to face each other, as highlighted in the exploded view in Fig. 5.1(b). We then connected two sets of belts to the output plate such that each brake locks one direction of motion; both directions of rotation are thus controllable. These belts rotate around a shaft located on the 3D printed triangular housing. To reduce friction, we installed needle bearings between the plate and the rotary shaft, as seen in Fig. 5.1(e).

Active reconfiguration of the brake was implemented by installing a small gearmotor [1] along the segment's z-axis, as shown in Fig. 5.1(c). The motor arm, equipped with four "fingers", sets the angle of the clamp in the xz-plane through its rotation. The motor is controlled by a micro-controller [2] via a H-bridge unit [3]. We detail how the movements of the motor arm correspond to the locking state and the sequence of locking in Sec. 5.4.4.

[1] Pololu 298:1 Micro Metal Gearmotor HPCB 6V

[2] Arduino UNO

[3] L298N H-bridge unit

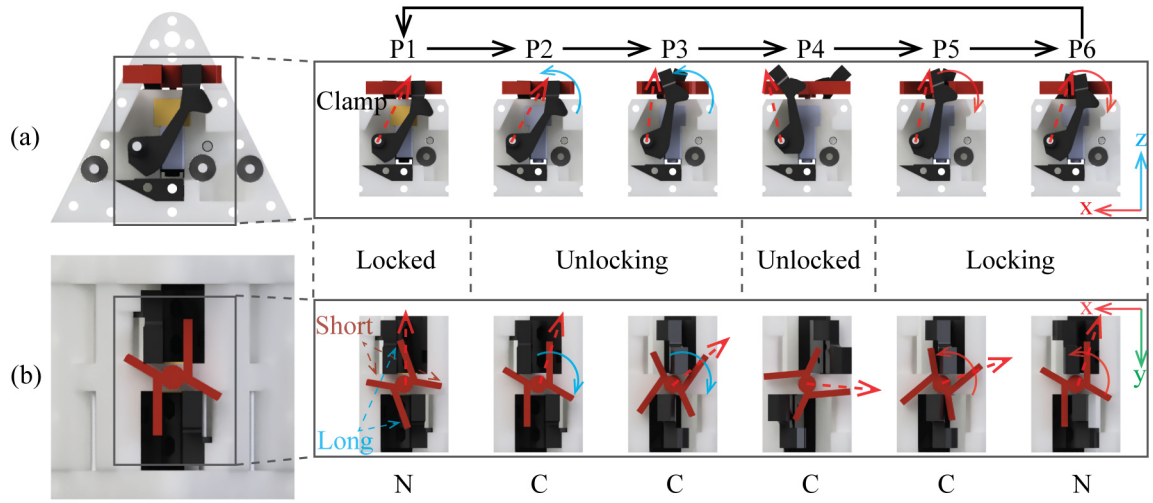

Figure 5.2. Locking sequence and brake configurations. The configuration of the clamp and motor arm are highlighted on the right side of column (a) and (b) according to phases P1 to P6 respectively. In this figure, the springs are not shown to emphasize the arm and clamp configurations. At the bottom, the letter "N" represents no contact between the arm and the clamp, while "C" indicates contact. To enhance clarity, the body is rendered in white and the motor arm in red, and a red dashed arrow is used to indicate the orientation of the clamp and motor arm.

5.4.3 Belt routing and tensioner design

As the brake utilizes a belt to transmit locking forces, a vital design of this robot is its routing system, including the belt, guiding pulleys, and spring tensioner, which work to keep the belt flat and in constant tension. The output's ability to rotate is controlled by the belts, but the total distance around the plate and the brake, L, is dependent on the system configuration, as seen in Fig. 5.1(f). L can be calculated as:

$$L = \underbrace{\sqrt{d_1^2 + h_1^2}}_{l_1} + \underbrace{\sqrt{d_2^2 + h_2^2}}_{l_2} + w \tag{5.1}$$

where l_p is the length of the top plate, w is the width of the brake slots, h is the height from the slot to top plate, and

$$\begin{cases} d_1 = \frac{l_p}{2} cos\theta - \frac{w}{2} \\ d_2 = \frac{l_p}{2} cos\theta - \frac{w}{2} \\ h_1 = h_r + h_p cos\theta + \frac{l_p}{2} sin\theta \\ h_2 = h_r - h_p cos\theta - \frac{l_p}{2} sin\theta \end{cases} \tag{5.2}$$

With a predefined, fixed length, the belt becomes loose at some configurations, creating slack. To keep the belt flat and in tension, we installed a spring-loaded linear tensioner under the plate, as illustrated in Fig. 5.1(e) in a section view and (f) as a simplified sketch. The tensioner is installed on the proximal end of the plate for each brake. Inside the tensioner, a linear slider moves along a 2 mm dowel pin, where a spring is installed between the slider and the edge of the plate. The belt is then attached to the slider on one end, routed through the module then fixed to the other side of the plate.

Based on the current dimensions of the module, the physical range of motion of the module is $\pm 65^\circ$. We calculate the required length using equation. (5.1) for the routing belt across its range, seen in Fig. 5.7(c) as the green dashed line. The maximum and minimum required length for the belt are 159.8 mm and 147.4 mm, respectively, and the minimal sliding distance is 12.4 mm.

A range of 25 mm is thus sufficient to accommodate the tensioner as well as the compressed spring. We have also included another 2 mm pin with bearings to reduce rubbing. When assembling the robot, a 148 mm belt was selected. At a joint angle of 0°, the tensioner is in its most compressed position. As the joint rotates, the required length decreases, and the tensioner compensates for the excess distance by removing slack. The dimensions of the lockable module are shown in Table 5.1.

5.4.4 *Locking sequence*

To illustrate how the locking states of the wearable module change based on the angle of the motor arm, the position of the clamp, and the contact between these two components, we start with the locked configuration as the initial state of the module. In this configuration, the clamp is at its smallest angle; a small clearance between the top of the clamp and the long finger on the arm can be seen in state P1 in Fig. 5.2.

The module remains locked because the spring maintains tension between the clamp and the belt until the arm rotates in the clockwise direction by a small amount, as shown in P2. At this point, contact occurs, and the short finger begins to push against the inner surface of the clamp. This causes the clamp to move counterclockwise and unlock the module, as shown in P3. After the clearance becomes larger than the thickness of the belt, any resistive forces remaining within the module are due to friction between the dowel pins and belt. To keep the module unlocked in this configuration, a small torque is required to oppose the clamp spring, as mentioned in Sec. 5.4.1. To provide such resistance, we utilize the non-backdriveability of the

Name	Symbol	Value/Range
Height	H	90 mm
Width	W	80 mm
Depth	d	80 mm
Rotate height	h_r	65 mm
Plate length	l_p	80 mm
Plate height	h_p	15 mm
Joint angle	θ	$-65° \sim 65°$
Pulley distance	w	51 mm
Total belt length	L	147.4 - 159.8 mm
Weight	m	263 g

Table 5.1: **Lockable module design parameter**

gearmotor. The spring, motor, gear ratio, and other design parameters have been selected such that the torque exerted by the spring on the motor arm is less than the torque required to overcome friction within the gearmotor.

The brake remains unlocked until the motor starts rotating counterclockwise. When the motor starts to rotate, the short finger disengages with the clamp first (P4 to P5). The long finger of the motor arm and the springs then start to push the clamp clockwise together, as shown in P6. With actuation, the brake module responds faster than with springs alone. After this active locking, the clamp is at its smallest angle, which allows the clamp to rotate to its lowest position due to the spring tension. At this final locking state, the motor is turned off, and the arm is no longer in contact with the clamp. The brake is then moved by the springs only and is ready for the next locking-unlocking cycle (P1).

5.5 Results and Analysis

5.5.1 Single-side brake tensile testing

To understand the locking conditions and optimize the design of the lockable module, we first conducted tensile testing on a single, one-sided brake. Although the lockable module is based on rotation and comprises two brake subsystems, analysis of a single-sided brake can provide valuable insights.

The brake was fixed to a tensile testing machine [4] with the belt attached to the load cell using a fixture along the x-axis, as seen in Fig. 5.3(a). The force and displacement data were collected by a PC during each of the five experiments. The belt was pulled at a velocity of 1 mm/s for 15 mm. Following each tensile testing cycle, we measured the required unlocking force on top of the clamp using a force

[4] Instron 5944 machine, 1 kN load cell at 1 kHz sampling rate

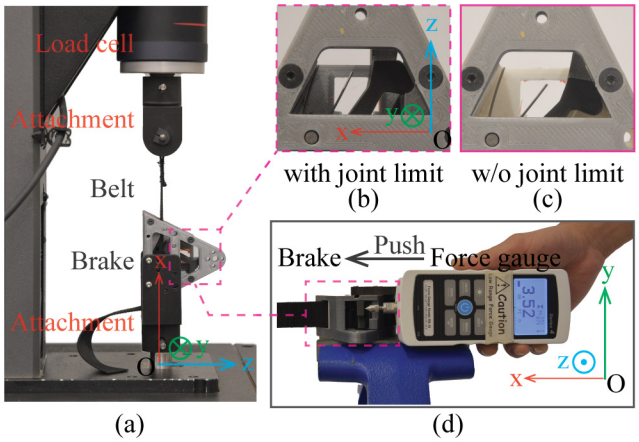

Figure 5.3. Brake tensile testing: (a) demonstrates the test set-up for measuring the brake tensile force using the Instron machine along with custom attachments. The belt is linked to the load cell, while the brake is affixed to the base of the tensile machine. (b) illustrates the joint limit on the clamp (black) and the base (gray), ensuring a fixed clamp rotation that prevents self-locking. In contrast, without the joint limit on the base (c), the brake transitions to a self-locking state under excessive load. Following each trial, the brake is secured to a blue vise, in (d), and a force gauge is employed to exert pressure on the clamp until it disengages. The peak compression during this process is thus recorded.

gauge [5] . The force gauge was used to push the top of the clamp until it rotated, as shown in Fig. 5.3(d). The peak compression recorded is considered the required unlocking force.

The height of the brake pad impacts the clearance and force metrics. We tested four brake pads of varying heights (from 0 to 1.5 mm with an increment of 0.5 mm). For each sub-experiment, a quick force ramp-up was observed, with a taller brake pad leading to higher tensile force, as shown in Fig. 5.4. The solid lines represent the average force, and the transparent area shows the error bar. We calculated the average tensile force, F_l, from the average force between 10 mm and 15 mm, as the force begins to reach its maximum. The output resistive force and the required unlocking force

[5] Mark-10, M4-10

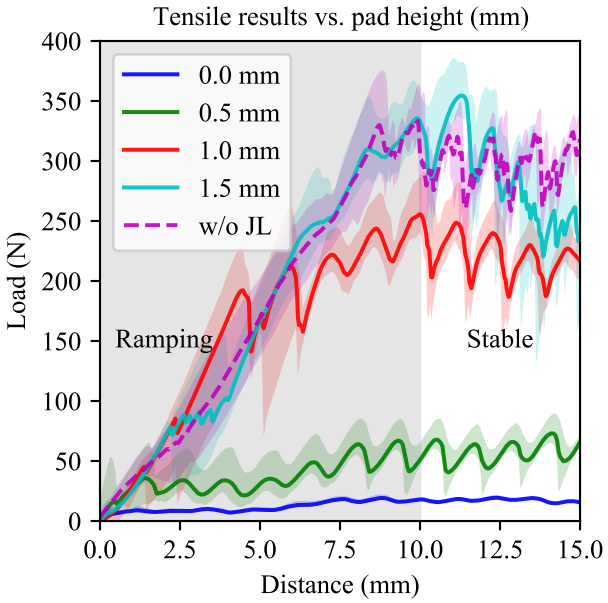

Figure 5.4. Brake tensile results: The solid lines represent the tensile results for four brake pads ranging from 0mm to 1.5mm with joint limits. A comparison of the 1mm brake pad results without the joint limit is shown with a purple dashed line. The transparent area surrounding the lines indicate the error bar from the experiments. The average F_l is calculated inside the stable region and the ramping region is indicated by a gray mask.

are documented in Table 5.2.

As the height of the brake pad increases, the clearance between the clamp and the brake pad decreases, transitioning from extremely low forces to a nearly self-locked system when pulled. The clearance for the 0 mm and 0.5 mm brake pads is 2 mm and 0.95 mm, respectively, with the belt thickness at 1 mm, results in an increase of braking force (from blue to green). A brake without a joint limit to restrict the clamp angle was tested, allowing it to enter the self-locking regime. This test's force result is represented by the dashed line in Fig. 5.4. Using a 1 mm brake pad produced a relatively constant locking force response, F_l. Upon removing the joint limit on the base, the brake began entering the self-locking regime, indicated in Fig. 5.3(c) by the

Height (mm)	C (mm)	F_l (N)	F_u (N)	Regime
0	2	17.37	2.232	Non-contact
0.5	0.95	54.47	4.056	Contact
1	0.55	211.73	3.316	Near S-L
1.5	0.2	265.67	3.38	Near S-L
1 (w/o joint limit)	0	289.97	26.984	Self-locked

Table 5.2: **Brake pad height vs. force metrics:** We compared the force metrics on the right against the height of the brake pad. C stands for the clearance between the brake pad and clamp, F_l represents the output locking force while F_u is the required force to unlock the brake. The last column indicates if the brake is contacted, self-locked or near self-locked (S-L).

purple dashed line.

Despite a higher output force, the required unlocking force, F_u, increased to around 27N, as a high amount of energy must be used to unlock a self-locked device. This is less desired in a lightweight and low-energy-consumption application, as providing large amounts of force at a high speed requires a larger motor that does not fit into our robot. Similar to the brake without a joint limit, a 1.5 mm brake pad approached the self-locking regime and generated more variable force output, as indicated by the cyan line. We thus select a 1 mm high brake pad.

5.5.2 Effect of belt routing system

As discussed in Sec. 5.4.3, the belt routing systems are designed to maintain tension and ensure the belt remains flat across various configurations. A crucial element of this subsystem is the linear tensioner in each brake. To better understand the tensioner's role, we compared the performance of a lockable module with the tensioner activated and deactivated. This evaluation included factors such as the range of slack, tensile results, and response speed. Given the module's symmetry, we measured this performance on one side only.

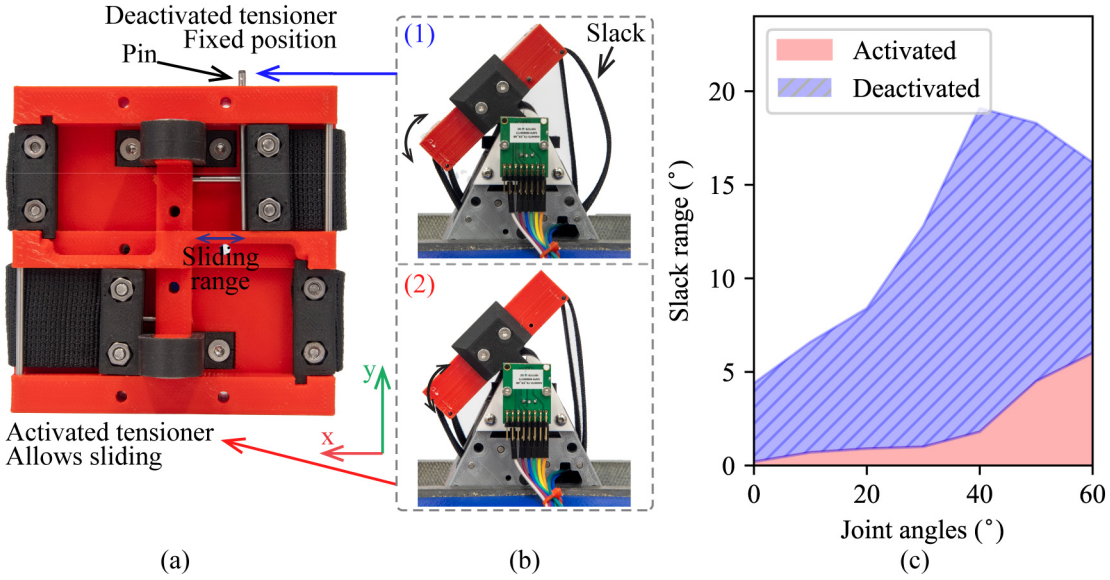

Figure 5.5. Slack evaluation: In (a), we insert a dowel pin to disable the linear tensioner. In these experiments, we disable two tensioner together and we only insert one pin to illustrate the difference between two tensioner states. We indicate the orientation of the output plate using the local coordinate in the lower right corner of (a). We highlight the slack at around 50° joint angle of two modules in (b), where we observed most slack in both module. With an activated tensioner that allows sliding, (2) significantly reduces the slack observed in (1). In (c), we compare the maximum angle of slack for the module with the tensioner (red) and without the tensioner (blue with hatch).

To temporarily deactivate the tensioner, we set it at its most compressed location, as depicted in Fig. 5.5(a), where a 2 mm dowel pin was inserted to prevent sliding and fix the linear slider. We then evaluated the slack of both modules by placing the plate in the locked state at various joint angles and rotating the plate within the slack region. Given the high resistive force of the module (>100 N), manual movement of the plate doesn't cause belt slippage, thus the permitted rotation angle measured by the angle sensor represents the slack range.

The tensioner effectively reduces slack but cannot completely eliminate it, as shown in Fig. 5.5(b). The backlash in the joint with the tensioner module is approximately 5°. Considering that the physical range of motion is ± 65°, the effective

range of motion becomes ± 60°. By contrast, the minimal slack at 0° joint angle for the module without the tensioner is the same as the slack tensioned module generated at 65°. This means that even when the module without the tensioner is locked around the flat configuration, it can still rotate about 5° due to the slack. This slack reduces the effective range of motion of the module. With the tensioner enabled, the belt maintains a tight configuration, which may lead to added friction in the unlocked state, we measure and discuss the effect of friction in the following section.

5.5.3 Lockable module tensile testing

The tensile testing for the lockable module is done using a similar method for the single brake as mentioned in Sec. 5.5.1 but is measured at multiple angles. A lockable segment was mounted to the lower fixture of the tensile testing machine and the z-axis of the module was then aligned with the center of the load cell, as illustrated in Fig. 5.6(a) and (c). A belt (length = 200 mm) fixed at the edge of the top plate is then connected to the load cell using a custom attachment.

To measure the joint angle of the lockable module, we installed a hall effect angle encoder [6] on the module. A disk magnet is installed to the module using a custom adapter with a clearance of 1 mm, as shown in Fig. 5.6(b). The angle data is then synced with the force and displacement reading from the tensile machine using the Arduino micro-controller.

During the experiment, we first move the plate to an initial angle, θ_i° according to the encoder reading and lock the module. We then use the tensile machine to pull the belt until the plate has been moved 10° and calculate the equivalent locking torque, T_l at the rotary joint according to the location of the load cell and plate angle, as:

$$\vec{T_l} = \vec{F_t} \times \vec{r_t} \tag{5.3}$$

[6] AS5047P-TS_EK_AB

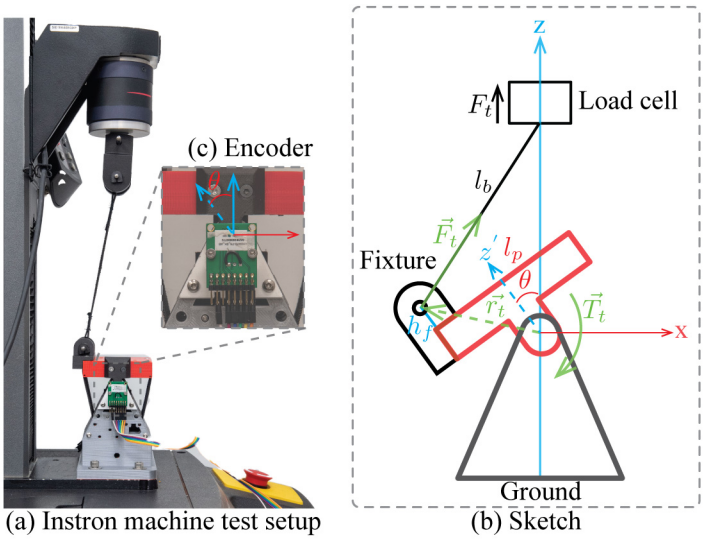

Figure 5.6. Lockable module tensile testing: (a) show the overview of the test setup, where the module is attached to the base of Instron machine using a custom 3D-printed attachment. The output plate is then connected to the load cell using a belt and custom fixture. These dimensions can be seen in simplified sketch in (b) while (c) highlights the module with the angle sensor to read the plate angle, θ.

We repeat each experiment three times to obtain the average locking torque at $(\theta_i - 10)^\circ$ and highlight a typical force response as an example in Fig. 5.7(b). We calculate the average equivalent locking torque according to the tensile machine and module configuration in Fig. 5.6(a) using the solid red line, across 0° to 50° with an increment of 10°, with the transparent area as the error bar, seen in Fig. 5.7(a). We did not measure the holding torque at 60°, as our experiments protocol requires us to set the initial angle, θ_i as 70°, which exceeds the physical range of motion.

The average resistive torque of the module is 11.98 Nm, with a minimum torque of 10.36 Nm at the flat configuration of 0°. We have also included the measured tensile force amplitude, F_t shown by the solid blue line in Fig. 5.7(a).

For the module without the tensioner, the measurement of the locking force less accurate, as the slack from the belt allows movement even when the brake is activated.

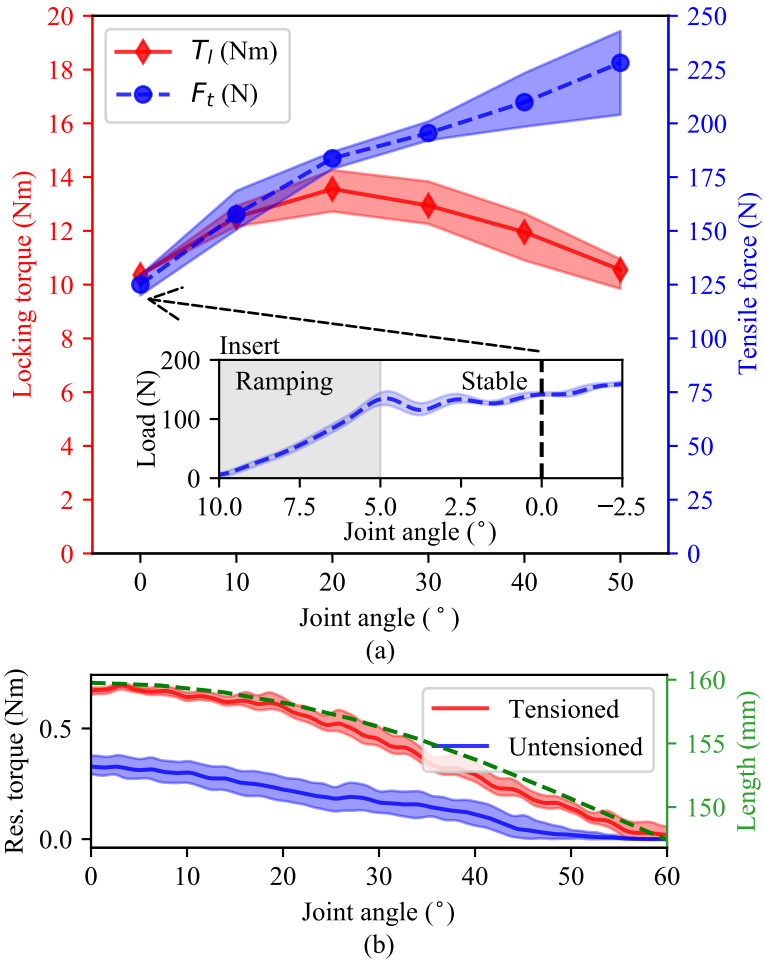

Figure 5.7. Lockable module tensile testing results: In (a), we show the maximum locking torque of the module across all configurations and provide an example of tensile testing results with force change versus joint angle in (b), located inside (a). In (c), we compare the unlocked state force for module with and without the tensioner using red and blue lines, respectively, with transparent area as the error bar. The green line and axis on the right stand for the required length of the belt across the joint angles.

When locked, the belt is first clamped around the brake pad and the slack at the current configuration permits rotation between the output plate and the base, leading to inconsistency in the slipping location and the locking angles. We thus skip the the locking force/torque for the module with tensioner disabled.

The frictional torque in the unlocked state is measured using a similar method, where we unlock the brake and compare the frictional force, both with and without the tensioner, as shown in Fig. 5.6(c). We observed a maximum resistive torque in the unlocked state at 0°. In this configuration, the routing requires the longest belt length, which creates the highest compression in the tensioner, and thus the highest pre-tension, which we believe plays a role.

The linear slider increases resistive torque in the system, primarily due to the friction between the belt and the dowel pins. This is in contrast to the lower resistive torques observed when the tensioner was disabled across all configurations. The required belt length, which is based on the current dimensions of the brake, are indicated on the right axis, and in green, in Fig. 5.6(c). We observed consistency between the required length and the resistive torque, confirming that the increased resistive torque is due to spring compression, belt tension, and pin friction. However, we chose to add the tensioner because a low frictional torque is acceptable when compared to a reduced range of motion and poor performance, as mentioned in Sec. 5.4.3.

5.5.4 Lockable module locking speed experiments

We utilized the same test setup as in Sec. 5.5.3 to measure the locking speeds of the lockable module at different angles. In each sub-experiment, we first set the module to its initial angle, θ_i, using the angle encoder. We then used the tensile machine to pull the plate at a constant linear velocity of 1 mm/s. Once the joint encoder detected a 5° angle increase, we locked the module by sending a locking command to the Arduino, recording the present force response and angle. We repeated the experiments three times and highlighted the average response at a 0° joint angle in Fig. 5.8(b).

In a typical transient response, the force first decreases to a local minimum before steadily increasing until we stop the tensile machine. We calculated the locking speed by determining the time between the locking signal (red dashed line) and the local minimum. We utilized the same test setup as in Sec. 5.5.3 to measure the locking speeds of the lockable module at different angles. In each sub-experiment, we first set the module to its initial angle, θ_i, using the angle encoder. We then used the tensile machine to pull the plate at a constant linear velocity of 1 mm/s. Once the joint encoder detected a 5° angle increase, we locked the module by sending a locking command to the Arduino, recording the present force response and angle. We configured the tensile machine to automatically stop the experiments upon detecting a 50 N pulling force. We repeated the experiments three times and highlighted the average response at a 0° joint angle in Fig. 5.8(b).

In a typical transient response, the force first decreases to a local minimum before steadily increasing until we stop the tensile machine. We calculated the locking speed by determining the time between the locking signal (red dashed line) and the local minimum. Using the same method, we compared the locking speed of the module at 0°, 10°, 20°, 30°, 40°, 50° and 60°. These results are shown in Fig. 5.8(a) as the solid red line with an error bar. The average locking time across all joint angles is 140 ms, with the slowest locking response being 146 ms at a 0° joint angle.

5.5.5 Unlocking speed experiments

The unlocking speed experiments were conducted using a similar method. We first locked the module at θ_i and then commanded the servo to continuously pull the module plate at a rate of 1 mm/s. The Arduino controller, synchronized with the tensile machine using the analog output function of the tensile testing machine, was able to read real-time force data. Once the module detected an external force

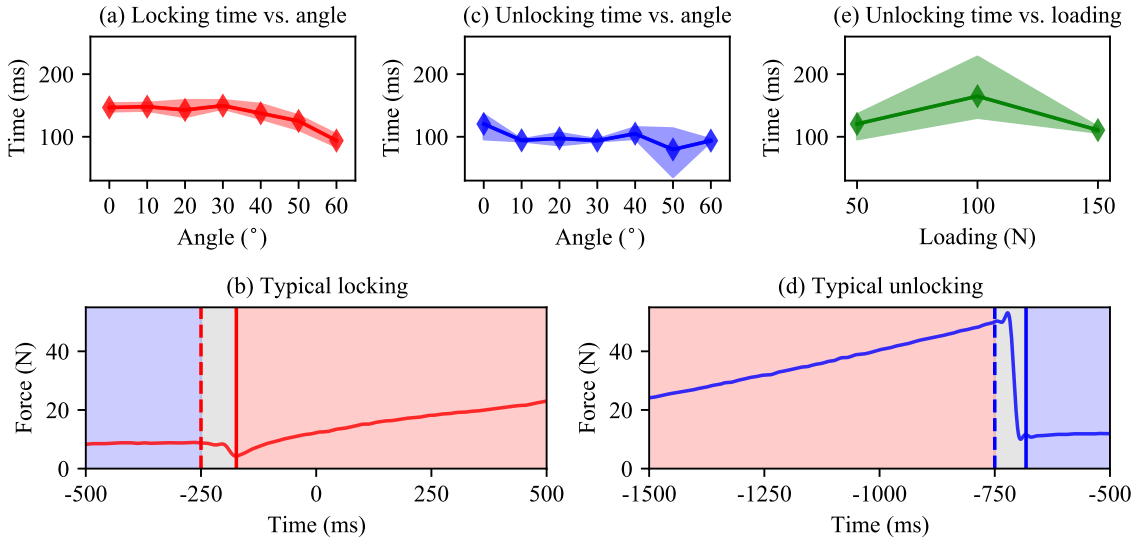

Figure 5.8. Response speed results: (a) Illustrates the change in locking response time versus joint angles. The diamond markers represent the data points, and the transparent bar indicates the error bar. (b) Highlights a typical locking response over time. We initiate the locking signal at 0 ms, as indicated by the dashed line, and we determine the locked state at the timestamp represented by the solid vertical line. The locking response time is calculated by subtracting these two timestamps. Similarly, (c) represents the unlocking response time against joint angle, while (d) displays a typical unlocking response. In (b) and (d), we denote the unlocked, locking, and locked states using transparent blue, gray, and red areas, respectively. Sub-figure (e) shows the unlocking response time against the external load applied to the module.

threshold of 50 N, it sent an unlock signal to the motor and released the brake.

We then recorded the tensile force to determine the unlocking time. We measured the average unlocking time across angles from 0° to 60°, with a 10° increment, and displayed the result in Fig. 5.8(c) using the blue line. A typical force and velocity response is highlighted in Fig. 5.8(d), where we show the load cell force against the timestamp. When the tensile machine pulled the module in the locked state, the force first ramped up to the threshold. After the module was unlocked, the force reading decreased until it dropped to the same level as the frictional force.

We determined the unlocking speed of the lockable module by calculating the time it took for the force to decrease to the frictional level. The average unlocking time is 97 ms, which aligns with the time it takes for the motor arm to spin the clamp to the unlocked position (a total spinning time of 100 ms in the micro-controller programming).

5.5.6 Unlocking under payload

To understand the module's ability to unlock under load, we used the same method as in the previous section, but with a focus on the external load rather than the joint angle. In this set of experiments, We adjusted the plate angle to 0° and then locked the module.We used the Instron machine to pull the output plate and monitor the resistive force. The force and distance data from the tensile machine were synced with the lockable module using an Arduino micro-controller. When the pulling force exceeded a threshold, we unlocked the module and used the angle encoder to measure the plate's angle. We varied this external load on the module and compared the unlocking performance under various payloads, as seen in Fig. 5.8(e), with an average unlocking time of 132 ms.

Since the belt routing system flattens the locking belt in the brakes and the locking force is constant across all configurations, as proven by the tensile testing and locking speed experiments, in these sets of experiments, we only measured the effect of changing payload at joint angle of 0°. We adjusted the external payload from 50 N to 150 N with an increment of 50 N.

The module was able to produce a stable unlocking response across the external load. This is because: 1) the belt routing systems keep the belt in flattened states, thus the external load is not applied to the clamp, and 2) the joint limit restricts the maximum joint angle and stabilizes the unlocking response so that the force imposed

on the motor is constant.

5.6 Comparison and discussion

5.6.1 Comparing with other locking strategies

We summarize the performance metrics of the lockable module and compare it with other locking solutions in robotics based on their features in Table 5.3. Our design goals and the features of the robot are listed at the bottom.

As mentioned in Table 5.1, the 3D dimensions of the module are $80 \times 80 \times 90$ mm and the weight is 263 g. Given that the maximum holding torque of the module is above 10 Nm and it responds within 150 ms, we believe it satisfies our requirements for a compact and low-weight solution.

While the locking strategies introduced here involve some design complexity and require special considerations to fully deploy and adapt to our research requirements, this locking device balances several critical and conflicting performance metrics. Despite its compact design, the module can be scaled up to accommodate various application requirements.

Although we did not measure the power consumption for this brake to switch between states, it can be concluded from the motor's data sheet as it's the only component that consumes energy. In our current design, we use a 6V micro-gearmotor [7] and its max power is 1.1 W. The time required for the brake to lock and unlock is around 140 ms, thus we estimate the energy to switch states does not exceed 0.15 J.

[7] Pololu 298:1 Micro Metal Gearmotor HPCB 6V

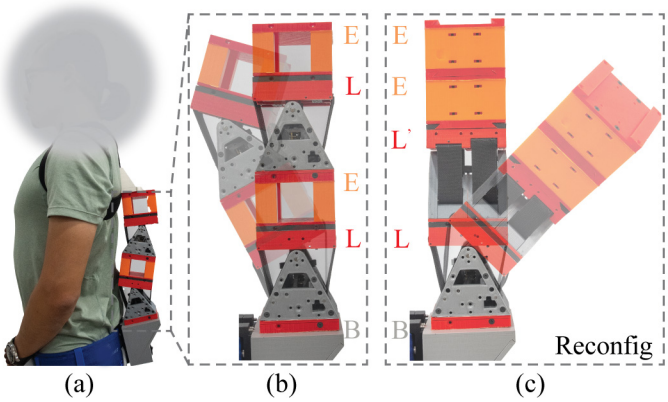

Figure 5.9. Module application: In (a), we show wearing demo with two modules, extension spacers and wearing interfaces. (b) highlights a configuration (E-L-E-L-B) to control sagittal plane bending and compares the straight and deformed configuration, where B stands for the base, L means lockable module and E is the extension spacer. We then change the configuration to E-E-L'-L-B in (c).

5.6.2 Application of modular wearable robot concept

To illustrate our concept of this passive lockable "Modular Wearable Robot", we equipped the lockable module with female and male modular connectors on the top and bottom of the module, respectively, following a modular robot design principle [27, 12]. The male interface can be connected in two ways, while the female connector only allows connection in one direction. Using a similar design to our previous robot [59], we connected three modules with wearable interfaces to realize a lockable spine robot, as shown in Fig. 5.9. To accommodate users of different heights, we included extension spacers with modular connectors and adjustable wearing interfaces, as seen in Fig. 5.9.

To fit the robot to a wearer, we first confirm the wearing interface locations then select the number and orientation of external load thus the lockable module and finally fill the blank using extension spacers. Currently, we plan to wear this robot along the human trunk given the size of the robot, and we highlight stiffening the trunk

in the sagittal plane in Fig. 5.9 (a) using two lockable modules and two extension spacers (E-L-E-L-B), as illustrated in Fig. 5.9 (b). The modularity of our design allows us to rapidly adjust the orientation, location, and number of external locking forces applied to the user. This flexibility facilitates human experiment studies, as the number, location and orientation of the external supporting force provided to the used can be easily customized and reconfigured. In (c), we modified the orientation and the location of the module to control the sagittal and frontal plane by rotating a lockable module for 90 °and reorganizing the configuration to E-E-L$^{'}$-L-B, where L$^{'}$ stands for rotation of 90 °. We will consider the performance of wearable systems composed of our lockable modules in future work.

5.7 Conclusion and future work

In this Chapter, we introduced a novel lockable module that controls rotational degree of freedom (DoF). The module is designed around a spring-loaded, "near" self-locking mechanism, with modifications to accommodate our requirements for low power consumption and fast response. We assembled the module with a brake and motor for active reconfiguration between engaged and disengaged configurations and optimized the belt-routing system to reduce slack and improve response speed. We calculated the resistive torque in both the locked and unlocked states, measured the response speed, and demonstrated the module's ability to unlock under load.

We have also demonstrated how near-self-locking mechanisms can be combined with other design considerations to reduce power consumption. Furthermore, we compared this brake design with other common locking strategies in robotics, outlining both the merits and disadvantages. One of the major challenges faced in this design is its complexity. To meet other design requirements such as fast response, low power consumption, high-force density, while still remaining compact

and lightweight, we made compromises on a series of design parameters and used an experiment-oriented method to select these parameters. However, we encapsulate this complexity within repeating modules; this modularity permits us to assemble larger systems more quickly without the mechanical complexity observed in prior work.

Future work includes optimizing the brake design by analyzing the geometry of the clamp and locking components to improve the braking force, and by exploring a wider range of motor/spring selections to increase speed and potentially force. The locking force of the module is related to the clearance between the clamp and the belt. By implementing active motor control and encoder sensing or using servo motors, we may be able to tune the output torque on-demand and enhance the module's performance by switching between locking regime. We also plan to improve the clamp manufacturing process and add a surface treatment to increase friction. Reducing the size of each module will also help us produce more capable wearable systems that can be worn in more places around the human body.

On the system-level, this module now permits comprehensive human testing to investigate the effect of force amplitude, orientation and location on human walking performance. We also plan to integrate sensors [123] between each module and implement control as well as automated decision making to the next generation of this robot.

Solution	**Locking positions**	**Size Weight**	**Stay unlocked**	**Direct driving**	**Num of directions**	**Speed**	**Respond under-load**	**Adjustable force/torque**	**Design complexity**
Latch [17]	finite	+	+	+	1	+	-	-	-
Ratchet [32]	finite	-	+	+	1	+	-	-	-
Cam-based [23]	infinite	+	+	+	1	-	-	-	-
Jamming [22, 1]	infinite	+	+	+	2	-	+	+	+
Capstan [40]	infinite	+	-	+	1	+	+	-	+
Dielectric [5]	infinite	+	-	+	2	+	+	+	+
Bistable [15]	infinite	-	+	+	2	+	+	-	++
Four-bar [113]	finite	-	+	-	2	-	+	-	-
Wedging [122]	infinite	+	+	-	1	-	+	++	++
This paper	infinite	-	+	-	2	+	+	-	++

Table 5.3: **Comparison of common locking strategies**. "-" means small or without such feature. "+" means large or has this feature while "+" stand for significant higher then other solutions.

Chapter 6

CONCLUSION AND FUTURE WORKS

6.1 Summary

A series of examples demonstrating the combination of soft robotics and mechanism design have been provided in this dissertation, showcasing how this general design principle can be applied to robotics research to enhance performance, reduce cost, or make robots more accessible.

More specifically, in Chapter 3, taking inspiration from the hinge design of origami-inspired robots, a compliant fin with "directional" stiffness was integrated into a flapping-wing rigid swimming robot. Leveraging geometry-based programmable deformation, this robot reduced the necessity for additional control and sensing, while still efficiently performing swimming maneuvers in complex granular media environments. Experimental methodologies, such as granular media force/torque collection, parameter fitting, and robot swimming efficiency measurement, were demonstrated.

The second method – implementing mechanisms into the structural elements of a soft robot – was then presented. Starting with lightweight and rapidly-customizable design requirements, an "exo-shell" wearable device with a laminate, folded structure was manufactured, analyzed, and evaluated in Chapter 4. To select the robot's dimensions, kinematic models were derived, both for element and system level, using a Python script. The test setup and experimental templates for evaluating slippage limit, kinematic models, system-level stiffness, and response speed using a UR5 robot arm were then introduced. This case study delivered a low-cost, rapidly customizable wearable robot design methodology.

Following the evaluation of the origami-inspired wearable robot and performance feedback, I began designing a high-torque and fast-responding, compact, lightweight wearable robot module. This was done with the objective to reduce the power consumption and cost of integration or customization for human studies. The mechanism design and integration for an effective brake design were showcased, and a comprehensive experimental template using an Instron tensile machine was provided. This approach allowed for a higher payload compared to hand-held experiments using a Mark-10 force gauge or a 50 N force level with a UR5 robot arm. Although this robot uses fewer soft materials than the other two, it serves as the locking/variable-stiffness components in larger soft robot systems. Finally I introduce the concept of "Modular Wearable Robot" using a similar serial-robot arrangement previous chapter.

In summary, two general approaches were presented with the aim of making robots more accessible, affordable, and efficient. By adjusting the ratio and locations of soft components, I categorized the first method as using soft robots as the end-effector in a rigid robot system and the second as implementing mechanism design into soft robot structures. It is worth noting that by further modifying the ratio and locations of soft components, one may derive similar yet distinct methodologies. The following section outlines my planned future work, which will focus on applying this design principle to other potential robotics applications.

6.2 The future directions

6.2.1 Compliant actuator design

Similar to the design of the brake module, which takes its locking concept from a global locking strategy embodied within the robot body but eventually transferred to a robot module performing stiffening tasks, I propose the development of modular

compliant actuators as an area of future work. Limiting design complexity to within the rotational braking module can significantly reduce the cost of future integration and enhance task performance by selectively adding new modules to a system. Future work includes, but is not limited to, variable stiffness modules, modular grippers, and sensing components.

6.2.2 Repeatable Soft Robots

One of the significant challenges in soft robotics, and consequently, one of my future work topics, is the introduction of standardized material characterization and repeatable soft robots. As soft robots are constructed from soft and flexible raw materials like polyester sheets, silicone, hydrogels, and more, the properties of these materials play a vital role in determining design parameters and overall performance. In order to overcome these challenges, it is crucial to collaborate with computer scientists and material experts to develop rapid, reliable, standardized, and repeatable characterization and modeling techniques for soft robotics. By identifying the minimal variables that need to be known and by creating adaptive methodologies, we can achieve a more consistent understanding of material behavior, ultimately leading to the design and development of more robust and dependable soft robotic systems. Establishing a strong foundation in material characterization will also facilitate collaboration and communication among researchers, fostering innovation and growth in the field of soft robotics for computation design and artificial intelligence.

6.2.3 Modular wearable robot

As mentioned in Chapter 5, my plan is to develop a lockable module with adjustable torque output, a sensor module capable of estimating the robot's state, and a base station with decision-making abilities for the modular wearable robot concept.

Collaborating with biomechanics researchers will facilitate investigating the optimal location, orientation, number, timing, and amplitude of the external stiffening torque applied to the user, and the potential effect on human walking performance. Ideally, such a system should be rapidly attachable and customizable using the modular connector, fully untethered using an internal battery, and responsive to the walking gait using the sensor and decision-making module.

6.2.4 Multi-gait/terrain locomotion

My future research plan includes studying multi-terrain adaptive locomotion, with a long-term goal of replicating the evolution of animal limbs in water, land, and air through a multi-gait/terrain locomotor robot. By identifying the minimal components for this multi-gait robot, I plan to design the corresponding reconfigurable limb device and work closely with zoologists to decipher the secrets of evolution. My past research on locomotion in granular media and reconfigurable devices provides insights into this topic and points to a promising direction in understanding animal locomotion using a robotics approach.

REFERENCES

[1] Aktaş, B., Y. S. Narang, N. Vasios, K. Bertoldi and R. D. Howe, "A Modeling Framework for Jamming Structures", Advanced Functional Materials (2021).

[2] Albert, I., J. G. Sample, A. J. Morss, S. Rajagopalan, A.-L. Barabási and P. Schiffer, "Granular drag on a discrete object: Shape effects on jamming", Phys. Rev. E **64**, 061303 (2001).

[3] Albert, R., M. A. Pfeifer, A. L. Barabási and P. Schiffer, "Slow drag in a granular medium", Physical Review Letters **82**, 1, 205–208 (1999).

[4] Aukes, D. M., B. Goldberg, M. R. Cutkosky and R. J. Wood, "An analytic framework for developing inherently-manufacturable pop-up laminate devices", Smart Materials and Structures **23**, 9 (2014).

[5] Aukes, D. M., B. Heyneman, J. Ulmen, H. S. Stuart, M. R. Cutkosky, S. Kim, P. Garcia, P. Garcia and A. Edsinger, "Design and testing of a selectively compliant underactuated hand", International Journal of Advanced Robotic Systems (2014).

[6] Aukes, D. M. and R. J. Wood, "PopupCAD: a tool for automated design, fabrication, and analysis of laminate devices", in "Micro- and Nanotechnology Sensors, Systems, and Applications VII", (Spie, 2015).

[7] Awad, L. N., J. Bae, K. O'Donnell, S. M. M. De Rossi, K. Hendron, L. H. Sloot, P. Kudzia, S. Allen, K. G. Holt, T. D. Ellis and C. J. Walsh, "A soft robotic exosuit improves walking in patients after stroke", Science Translational Medicine **9**, 400 (2017).

[8] Belke, C. H. and J. Paik, "Mori: A Modular Origami Robot", IEEE-ASME Transactions on Mechatronics **22**, 5 (2017).

[9] Boffey, D., I. Harat, Y. Gepner, C. L. Frosti, S. Funk and J. R. Hoffman, "The Physiology and Biomechanics of Load Carriage Performance", Military Medicine **184**, 1-2 (2019).

[10] Caldwell, J. N., L. Engelen, C. van der Henst, M. J. Patterson and N. A. S. Taylor, "The Interaction of Body Armor, Low-Intensity Exercise, and Hot-Humid Conditions on Physiological Strain and Cognitive Function", Military Medicine **176**, 5 (2011).

[11] Chen, A., R. Yin, L. Cao, C. Yuan, H. Ding and W. Zhang, "Soft robotics: Definition and research issues", in "International Conference on Mechatronics and Machine Vision in Practice (M2VIP)", (2017).

[12] Chen, I.-M. and M. Yim, "Modular Robots", in "Springer Handbook of Robotics", edited by B. Siciliano and O. Khatib, Springer Handbooks (Springer International Publishing, Cham, 2016).

[13] Cherelle, P., V. Grosu, A. Matthys, B. Vanderborght and D. Lefeber, "Design and Validation of the Ankle Mimicking Prosthetic (AMP-) Foot 2.0", IEEE Transactions on Neural Systems and Rehabilitation Engineering (2014).

[14] Choi, W. H., S. Kim, D. Lee and D. Shin, "Soft, Multi-DoF, Variable Stiffness Mechanism Using Layer Jamming for Wearable Robots", IEEE Robotics and Automation Letters (2019).

[15] Chou, J. B., K. Yu and M. C. Wu, "Electrothermally Actuated Lens Scanner and Latching Brake for Free-Space Board-to-Board Optical Interconnects", J. Microelectromech. Syst. (2012).

[16] Chu, A., H. Kazerooni and A. Zoss, "On the Biomimetic Design of the Berkeley Lower Extremity Exoskeleton (BLEEX)", in "IEEE/RSJ International Conference on Intelligent Robots and Systems (IROS)", (2005).

[17] Collins, S. H. and A. D. Kuo, "Recycling Energy to Restore Impaired Ankle Function during Human Walking", PLoS ONE (2010).

[18] Collo, A., V. Bonnet and G. Venture, "A quasi-passive lower limb exoskeleton for partial body weight support", International Conference on Biomedical Robotics and Biomechatronics (2016).

[19] Dickinson, M. H., "How Animals Move: An Integrative View", Science **288**, 5463, 100–106 (2000).

[20] Ding, Y., I. Galiana, A. T. Asbeck, S. M. M. De Rossi, J. Bae, T. R. T. Santos, V. L. de Araujo, S. Lee, K. G. Holt and C. Walsh, "Biomechanical and Physiological Evaluation of Multi-Joint Assistance With Soft Exosuits", IEEE Transactions on Neural Systems and Rehabilitation Engineering **25**, 2 (2017).

[21] Ding, Y., N. Gravish and D. I. Goldman, "Drag induced lift in granular media", Physical Review Letters **106**, 2, 1–4 (2011).

[22] Do, B. H., I. Choi and S. Follmer, "An All-Soft Variable Impedance Actuator Enabled by Embedded Layer Jamming", IEEE/ASME Transactions on Mechatronics (2022).

[23] Fang, D., J. Shang, Z. Luo, P. Lv and G. Wu, "Development of a novel self-locking mechanism for continuous propulsion inchworm in-pipe robot", Advances in Mechanical Engineering (2018).

[24] Felton, S. M., M. T. Tolley, E. D. Demaine, D. Rus and R. J. Wood, "A method for building self-folding machines", Science (2014).

[25] Filipov, E. T., T. Tachi and G. H. Paulino, "Origami tubes assembled into stiff, yet reconfigurable structures and metamaterials", Pnas (2015).

[26] Firouzeh, A. and J. Paik, "Robogami: A fully integrated low-profile robotic origami", Asme Jmr (2015).

[27] Gilpin, K. and D. Rus, "Modular Robot Systems", IEEE Robotics & Automation Magazine (2010).

[28] Goldman, D. I., "Colloquium: Biophysical principles of undulatory self-propulsion in granular media", Reviews of Modern Physics **86**, 3, 943–958 (2014).

[29] Grabowski, A., C. T. Farley and R. Kram, "Independent metabolic costs of supporting body weight and accelerating body mass during walking", Journal of Applied Physiology **98**, 2 (2005).

[30] Gray, B. Y. J. and G. J. Hancockf, "The Propulsion of Sea-Urchin Spermatozoa", Journal of Experimental Biology **32**, 4, 802–814 (1955).

[31] Gregorczyk, K. N., L. Hasselquist, J. M. Schiffman, C. K. Bensel, J. P. Obusek and D. J. Gutekunst, "Effects of a lower-body exoskeleton device on metabolic cost and gait biomechanics during load carriage", Ergonomics **53**, 10 (2010).

[32] Guo, X.-Y., W.-B. Li, Q.-H. Gao, H. Yan, Y.-Q. Fei and W.-M. Zhang, "Self-locking mechanism for variable stiffness rigid–soft gripper", Smart Materials and Structures (2020).

[33] Han, K., D. Peric, D. Owen and J. Yu, "A combined finite/discrete element simulation of shot peening processes – Part II: 3D interaction laws", Engineering Computations **17**, 6, 680–702 (2000).

[34] Hansen, N., Y. Akimoto and P. Baudis, "CMA-ES/pycma on Github", Zenodo, DOI:10.5281/zenodo.2559634, URL `https://doi.org/10.5281/zenodo.2559634`, published: Zenodo, DOI:10.5281/zenodo.2559634 (2019).

[35] Hawkes, E. W., B. An, N. Benbernou, H. Tanaka, S. Kim, E. D. Demaine, D. Rus and R. J. Wood, "Programmable matter by folding", Pnas (2010).

[36] Heo, U., S. J. Kim and J. Kim, "Backdrivable and Fully-Portable Pneumatic Back Support Exoskeleton for Lifting Assistance", IEEE Robotics and Automation Letters **5**, 2 (2020).

[37] Hosoi, A. and D. I. Goldman, "Beneath Our Feet: Strategies for Locomotion in Granular Media", Annual Review of Fluid Mechanics **47**, 1, 431–453 (2015).

[38] Hsu, J., E. Yoshida, K. Harada and A. Kheddar, "Self-Locking Underactuated Mechanism for Robotic Gripper", in "IEEE International Conference on Advanced Intelligent Mechatronics (AIM)", (2017).

[39] Huang, S., Y. Tang, H. Bagheri, D. Li, A. Ardente, D. Aukes, H. Marvi and J. J. Tao, "Effects of Friction Anisotropy on Upward Burrowing Behavior of Soft Robots in Granular Materials", Advanced Intelligent Systems **2**, 6, 1900183 (2020).

[40] In, H., S. Kang and K.-J. Cho, "Capstan brake: Passive brake for tendon-driven mechanism", in "IEEE/RSJ International Conference on Intelligent Robots and Systems (IROS)", (2012).

[41] Jang, J. H., A. Sales Coutinho Junior, Y. J. Park and H. Rodrigue, "A Positive and Negative Pressure Soft Linear Brake for Wearable Applications", IEEE Transactions on Industrial Electronics (2022).

[42] Jiang, M., Z. Zhou and N. Gravish, "Flexoskeleton Printing Enables Versatile Fabrication of Hybrid Soft and Rigid Robots", Soft Robotics (2020).

[43] Jiang, Y., D. Chen, C. Liu and J. Li, "Chain-Like Granular Jamming: A Novel Stiffness-Programmable Mechanism for Soft Robotics", Soft Robotics (2019).

[44] Jiang, Y., D. Chen, C. Liu and J. Li, "Chain-like granular jamming: A novel stiffness-programmable mechanism for soft robotics", Soft Robotics **6**, 1 (2019).

[45] K., S., I. S. and T. H., "Applying a flexible microactuator to robotic mechanisms", IEEE Control Syst. (1992).

[46] Kazerooni, H., J.-L. Racine, L. Huang and R. Steger, "On the Control of the Berkeley Lower Extremity Exoskeleton (BLEEX)", in "IEEE International Conference on Robotics and Automation (ICRA)", (2005).

[47] Kermavnar, T., K. J. O'Sullivan, A. de Eyto and L. W. O'Sullivan, "Discomfort/Pain and Tissue Oxygenation at the Lower Limb During Circumferential Compression: Application to Soft Exoskeleton Design", Hum Factors **62**, 3 (2020).

[48] Kim, J. and S. B. Choi, "Design and Modeling of a Clutch Actuator System With Self-Energizing Mechanism", IEEE/ASME Transactions on Mechatronics (2011).

[49] Kim, Y., S. Cheng, S. Kim and K. Iagnemma, "A Novel Layer Jamming Mechanism With Tunable Stiffness Capability for Minimally Invasive Surgery", IEEE Transactions on Robotics **29**, 4 (2013).

[50] Lauder, G. V., E. J. Anderson, J. Tangorra and P. G. A. Madden, "Fish biorobotics: kinematics and hydrodynamics of self-propulsion", Journal of Experimental Biology **210**, 16, 2767–2780 (2007).

[51] Lauga, E., "Floppy swimming: Viscous locomotion of actuated elastica", Physical Review E **75**, 4, 041916 (2007).

[52] Lauga, E. and T. R. Powers, "The hydrodynamics of swimming microorganisms", Reports on Progress in Physics **72**, 9, 096601 (2009).

[53] Lee, C. S., S. GodageIsuru, GonthinaPhanideep and D. WalkerIan, "Soft robots and kangaroo tails: Modulating compliance in continuum structures through mechanical layer jamming", Soft robotics (2016).

[54] Lee, D., S. Kim, H.-J. Park, S. Kim and D. Shin, "A Spine Assistive Robot With a Routed Twisted String Actuator and a Flat-Back Alleviation Mechanism for Lumbar-Degenerative Flat Back", IEEE/ASME Trans. Mechatron. (2022).

[55] Lee, G. L., D. H. Ahn, B. R. de Supinski, J. Gyllenhaal and P. Miller, "Pynamic: the Python Dynamic Benchmark", in "IEEE International Symposium on Workload Characterization", p. 6 (2007).

[56] Lee, S., J. Kim, L. Baker, A. Long, N. Karavas, N. Menard, I. Galiana and C. J. Walsh, "Autonomous multi-joint soft exosuit with augmentation-power-based control parameter tuning reduces energy cost of loaded walking", Journal of NeuroEngineering and Rehabilitation **15**, 1 (2018).

[57] Li, C., T. Zhang and D. I. Goldman, "A Terradynamics of Legged Locomotion on Granular Media", Science **339**, 6126, 1408–1412 (2013).

[58] Li, D., S. Huang, Y. Tang, H. Marvi, J. Tao and D. Aukes, "Compliant Fins for Locomotion in Granular Media", IEEE Robotics and Automation Letters (2021).

[59] Li, D., E. Q. Yumbla, A. Olivas, T. Sugar, H. B. Amor, H. Lee, W. Zhang and D. M. Aukes, "Origami-inspired wearable robots for trunk support", IEEE/ASME Transactions on Mechatronics (2022).

[60] Li, Y., Y. Chen, Y. Yang and Y. Wei, "Passive Particle Jamming and Its Stiffening of Soft Robotic Grippers", IEEE Transactions on Robotics (2017).

[61] Lin, Y., G. Yang, Y. Liang, C. Zhang, W. Wang, W. Wang, D. Qian, H. Yang and J. Zou, "Controllable stiffness origami "skeletons" for lightweight and multifunctional artificial muscles", Advanced Functional Materials (2020).

[62] Liu, T., H. Xia, D.-Y. Lee, A. Firouzeh, Y.-L. Park and K.-J. Cho, "A Positive Pressure Jamming Based Variable Stiffness Structure and its Application on Wearable Robots", IEEE Robotics and Automation Letters (2021).

[63] Loschak, P. M., S. F. Burke, E. Zumbro, A. R. Forelli and R. D. Howe, "A Robotic System for Actively Stiffening Flexible Manipulators", IEEE/RSJ International Conference on Intelligent Robots and Systems (IROS) **2015** (2015).

[64] Lucas, K. N., N. Johnson, W. T. Beaulieu, E. Cathcart, G. Tirrell, S. P. Colin, B. J. Gemmell, J. O. Dabiri and J. H. Costello, "Bending rules for animal propulsion", Nature Communications **5**, May 2013, 1–7 (2014).

[65] Maladen, R. D., Y. Ding, C. Li and D. I. Goldman, "Undulatory Swimming in Sand: Subsurface Locomotion of the Sandfish Lizard", Science **325**, 5938, 314–318 (2009).

[66] Maladen, R. D., Y. Ding, P. B. Umbanhowar, A. Kamor and D. I. Goldman, "Mechanical models of sandfish locomotion reveal principles of high performance subsurface sand-swimming", Journal of the Royal Society Interface **8**, 62, 1332–1345 (2011).

[67] Maladen, R. D., P. B. Umbanhowar, Y. Ding, A. Masse and D. I. Goldman, "Granular lift forces predict vertical motion of a sand-swimming robot", in "IEEE International Conference on Robotics and Automation (ICRA)", pp. 1398–1403 (2011).

[68] Marvi, H., C. Gong, N. Gravish, H. Astley, D. L. Hu and D. I. Goldman, "Sidewinding with minimal slip: Snake and robot ascent ofsandy slopes", Science **346**, 6206 (2014).

[69] Masood Nevisipour, T. S. and H. Lee, "Trunk Control In Young Healthy Adults Requires Large Adaptations During And After Obstacle Avoidance With A Cognitive Task", in "The 45th Annual Meeting of the American Society of Biomechanics", (2021).

[70] Masood Nevisipour, T. S. and H. Lee, "In preparation –Multi-tasking deteriorates trunk movement control during and after obstacle avoidance", Human Movement Science (2022).

[71] Mazouchova, N., P. B. Umbanhowar and D. I. Goldman, "Flipper-driven terrestrial locomotion of a sea turtle-inspired robot", BIOINSPIRATION & BIOMIMETICS **8**, 2, publisher: IOP PUBLISHING LTD (2013).

[72] Mazumdar, A., S. J. Spencer, C. Hobart, J. Dabling, T. Blada, K. Dullea, M. Kuehl and S. P. Buerger, "Synthetic Fiber Capstan Drives for Highly Efficient, Torque Controlled, Robotic Applications", IEEE Robotics and Automation Letters (2017).

[73] Mengüç, Y., Y.-L. Park, H. Pei, D. Vogt, P. M. Aubin, E. Winchell, L. Fluke, L. Stirling, R. J. Wood and C. J. Walsh, "Wearable soft sensing suit for human gait measurement", International Journal of Advanced Robotic Systems **33**, 14 (2014).

[74] Michael, M., F. Vogel and B. Peters, "DEM–FEM coupling simulations of the interactions between a tire tread and granular terrain", Computer Methods in Applied Mechanics and Engineering **289**, 227–248 (2015).

[75] Mintchev, S., J. Shintake and D. Floreano, "Bioinspired dual-stiffness origami.", Science Robotics (2018).

[76] Mueller, D., J. W. Gerdes and S. K. Gupta, "Incorporation of Passive Wing Folding in Flapping Wing Miniature Air Vehicles", in "IDETC-CIE2009", pp. 797–805 (2009), event-place: Volume 7: 33rd Mechanisms and Robotics Conference, Parts A and B.

[77] Narang, Y. S., J. J. Vlassak and R. D. Howe, "Mechanically versatile soft machines through laminar jamming", Advanced Functional Materials (2018).

[78] Nian, P., B. Song, J. Xuan, W. Zhou and D. Xue, "Study on flexible flapping wings with three dimensional asymmetric passive deformation in a flapping cycle", Aerospace Science and Technology **104**, 105944 (2020).

[79] Onal, C. D., R. J. Wood and D. Rus, "Towards printable robotics: Origami-inspired planar fabrication of three-dimensional mechanisms", in "IEEE International Conference on Robotics and Automation (ICRA)", pp. 4608–4613 (IEEE, 2011).

[80] Onal, C. D., R. J. Wood and D. Rus, "An Origami-Inspired Approach to Worm Robots", IEEE/ASME Transactions on Mechatronics **18**, 2, 430–438 (2013).

[81] Ortiz, D., N. Gravish and M. T. Tolley, "Soft Robot Actuation Strategies for Locomotion in Granular Substrates", IEEE Robotics and Automation Letters **4**, 3, 2630–2636 (2019).

[82] Park, J.-H., P. R. Stegall, D. P. Roye and S. K. Agrawal, "Robotic Spine Exoskeleton (RoSE): Characterizing the 3-D Stiffness of the Human Torso in the Treatment of Spine Deformity", IEEE Trans. Neural Syst. Rehabil. Eng. (2018).

[83] Peng, Z., Y. Ding, K. Pietrzyk, G. J. Elfring and O. S. Pak, "Propulsion via flexible flapping in granular media", Physical Review E **96**, 1, 012907 (2017).

[84] Peng, Z., G. J. Elfring and O. S. Pak, "Maximizing propulsive thrust of a driven filament at low Reynolds number via variable flexibility", Soft Matter **13**, 12, 2339–2347 (2017).

[85] Perry, J. C., J. Rosen and S. Burns, "Upper-Limb Powered Exoskeleton Design", IEEE/ASME Transactions on Mechatronics **12**, 4 (2007).

[86] Plooij, M., G. Mathijssen, P. Cherelle, D. Lefeber and B. Vanderborght, "Lock Your Robot: A Review of Locking Devices in Robotics", IEEE Robotics & Automation Magazine (2015).

[87] Plooij, M., T. Van Der Hoeven, G. Dunning and M. Wisse, "Statically Balanced Brakes", Precision Engineering (2016).

[88] Pratt, J., B. Krupp, C. Morse and S. Collins, "The RoboKnee: an exoskeleton for enhancing strength and endurance during walking", in "IEEE International Conference on Robotics and Automation (ICRA)", vol. 3 (2004).

[89] Purcell, E. M., "Life at low Reynolds number", American Journal of Physics **45**, 1, 3–11 (1977).

[90] Pérez Vidal, A. F., J. Y. Rumbo Morales, G. Ortiz Torres, F. d. J. Sorcia Vázquez, A. Cruz Rojas, J. A. Brizuela Mendoza and J. C. Rodríguez Cerda, "Soft Exoskeletons: Development, Requirements, and Challenges of the Last Decade", Actuators **10**, 7 (2021).

[91] Quinlivan, B. T., S. Lee, P. Malcolm, D. M. Rossi, M. Grimmer, C. Siviy, N. Karavas, D. Wagner, A. Asbeck, I. Galiana and C. J. Walsh, "Assistance magnitude versus metabolic cost reductions for a tethered multiarticular soft exosuit", Science Robotics (2017).

[92] Quinlivan, B. T., S. Lee, P. Malcolm, D. M. Rossi, M. Grimmer, C. Siviy, N. Karavas, D. Wagner, A. Asbeck, I. Galiana and C. J. Walsh, "Assistance magnitude versus metabolic cost reductions for a tethered multiarticular soft exosuit", Science Robotics **2**, 2 (2017).

[93] Rapaport, D. C., *The Art of Molecular Dynamics Simulation* (Cambridge University Press, 2004).

[94] Rupal, B. S., S. Rafique, A. Singla, E. Singla, M. Isaksson and G. S. Virk, "Lower-limb exoskeletons: Research trends and regulatory guidelines in medical and non-medical applications", International Journal of Advanced Robotic Systems **14**, 6 (2017).

[95] Russell, R. A., "CRABOT: A Biomimetic Burrowing Robot Designed for Underground Chemical Source Location", Advanced Robotics **25**, 1, 119–134 (2011).

[96] Salmoiraghi, A. and D. Akin, "Review of Wearable Robotic Assistive Devices for Integration with Pressure Suit Arms", in "42nd International Conference on Environmental Systems", (American Institute of Aeronautics and Astronautics, San Diego, California, 2012).

[97] Shah, D., E. J. Yang, M. C. Yuen, E. C. Huang and R. Kramer-Bottiglio, "Jamming skins that control system rigidity from the surface", Advanced Functional Materials (2020).

[98] Sharifzadeh, M., Y. Jiang and D. M. Aukes, "Reconfigurable Curved Beams for Selectable Swimming Gaits in an Underwater Robot", IEEE Robotics and Automation Letters **6**, 2 (2021).

[99] Sharifzadeh, M., R. Khodambashi and D. M. Aukes, "An Integrated Design and Simulation Environment for Rapid Prototyping of Laminate Robotic Mechanisms", in "IDETC-CIE2018", (2018).

[100] Shoele, K. and Q. Zhu, "Performance of a wing with nonuniform flexibility in hovering flight", Physics of Fluids **25**, 4, 041901 (2013).

[101] SuitX, "PhoeniX Suit, www.suitx.com", (2022).

[102] Sun, Y., X. Wu, B. Lu, M. Wang, J. Ding, H. Pu, W. Jia, Y. Peng and J. Luo, "Electrostatic Layer Jamming Variable Stiffness Enhanced by Giant Electrorheological Fluid", IEEE/ASME Transactions on Mechatronics (2023).

[103] Suzumori, K., S. Iikura and H. Tanaka, "Development of flexible microactuator and its applications to robotic mechanisms", in "Proceedings. 1991 IEEE International Conference on Robotics and Automation", pp. 1622–1627 vol.2 (1991).

[104] Tao, J. J., S. Huang and Y. Tang, "Bioinspired Self-Burrowing-Out Robot in Dry Sand", Journal of Geotechnical and Geoenvironmental Engineering **145**, 12, 02819002 (2019).

[105] Tao, J. J., S. Huang and Y. Tang, "SBOR: a minimalistic soft self-burrowing-out robot inspired by razor clams", Bioinspiration & Biomimetics **15**, 5, 055003, URL `https://doi.org/10.1088/1748-3190/ab8754`, publisher: IOP Publishing (2020).

[106] Taylor, N. A., G. E. Peoples and S. R. Petersen, "Load carriage, human performance, and employment standards", Applied Physiology, Nutrition, and Metabolism **41**, 6 (Suppl. 2) (2016).

[107] Thomas, G. C., C. C. Gimenez, E. D. Chin, A. P. Carmedelle and A. M. Hoover, "Controllable, High Force Amplification Using Elastic Cable Capstans", in "Volume 4: 36th Mechanisms and Robotics Conference, Parts A and B", (2012).

[108] Tolley, M. T., S. M. Felton, S. Miyashita, D. Aukes, D. Rus and R. J. Wood, "Self-folding origami: shape memory composites activated by uniform heating", Smart Materials and Structures **23**, 9, 094006 (2014).

[109] Trueman, E., "The Mechanism of Burrowing of the Mole Crab, Emerita", Journal of Experimental Biology **53**, 3, 701–710 (1970).

[110] Tu, F., D. Delbergue, H. Miao, T. Klotz, M. Brochu, P. Bocher and M. Levesque, "A sequential DEM-FEM coupling method for shot peening simulation", Surface and Coatings Technology **319**, 200–212 (2017).

[111] Tummala, Y., M. Frecker, A. Wissa and J. E. Hubbard, Jr., "Design and Optimization of a Bend-and-Sweep Compliant Mechanism", in "Volume 6A: 37th Mechanisms and Robotics Conference", (2013).

[112] van Herpen, F. H. M., R. B. van Dijsseldonk, H. Rijken, N. L. W. Keijsers, J. W. K. Louwerens and I. J. W. van Nes, "Case Report: Description of two fractures during the use of a powered exoskeleton", Spinal Cord Ser Cases **5**, 1 (2019).

[113] van Oort, G., R. Carloni, D. J. Borgerink and S. Stramigioli, "An Energy Efficient Knee Locking Mechanism for a Dynamically Walking Robot", in "IEEE International Conference on Robotics and Automation (ICRA)", (2011).

[114] Walsh, C. J., Ken Endo and H. M. Herr, "A quasi-passive leg exoskeleton for load-carrying augmentation", International Journal of Humanoid Robotics (2007).

[115] Wang, T., J. Zhang, Y. Li, J. Hong and M. Y. Wang, "Electrostatic Layer Jamming Variable Stiffness for Soft Robotics", IEEE-ASME Transactions on Mechatronics (2019).

[116] Wang, X. and S. Alben, "Dynamics and locomotion of flexible foils in a frictional environment", Proceedings of the Royal Society A: Mathematical, Physical and Engineering Sciences **474**, 2209 (2018).

[117] Whitesides, G. M., "Soft Robotics", Angewandte Chemie International Edition **57**, 16, URL https://onlinelibrary.wiley.com/doi/10.1002/anie.201800907 (2018).

[118] Wieghardt, K., "Experiments in Granular Flow.", Annu Rev Fluid Mech **v**, 89–114 (1975).

[119] Wood, R., "The First Takeoff of a Biologically Inspired At-Scale Robotic Insect", IEEE Transactions on Robotics **24**, 2, 341–347 (2008).

[120] Yang, X., T.-H. Huang, H. Hu, S. Yu, S. Zhang, X. Zhou, A. Carriero, G. Yue and H. Su, "Spine-Inspired Continuum Soft Exoskeleton for Stoop Lifting Assistance", IEEE Robotics and Automation Letters (2019).

[121] Yang, Y., Y. Zhang, Z. Kan, J. Zeng and M. Y. Wang, "Hybrid Jamming for Bioinspired Soft Robotic Fingers", Soft Robotics (2020).

[122] Yu, L., L. Ma, J. Song and X. Liu, "Magnetorheological and Wedge Mechanism-Based Brake-by-Wire System With Self-Energizing and Self-Powered Capability by Brake Energy Harvesting", IEEE/ASME Transactions on Mechatronics (2016).

[123] Yumbla, E. Q., D. Li, T. M. Nibi, D. M. Aukes and W. Zhang, "A Kinematically Constrained Kalman Filter for Sensor Fusion in a Wearable Origami Robot", ASME Letters in Dynamic Systems and Control (2023).

[124] Zhai, Z., Y. Wang and H. Jiang, "Origami-inspired, on-demand deployable and collapsible mechanical metamaterials with tunable stiffness", Pnas (2018).

[125] Zhang, T. and D. I. Goldman, "The effectiveness of resistive force theory in granular locomotion", Physics of Fluids **26**, 10, 0–17 (2014).

[126] Zoss, A., H. Kazerooni and A. Chu, "Biomechanical design of the Berkeley lower extremity exoskeleton (BLEEX)", IEEE/ASME Transactions on Mechatronics **11**, 2 (2006).

APPENDIX A

KEYWORDS AND METHODS INDEX

KEYWORDS AND METHODS INDEX